Title
Non-Equilibrium in the Mars Entry Shock Layer Characterized via Laser Absorption Spectroscopy

Author
Jelloian, Christopher

Publication Date
2022

Peer reviewed|Thesis/dissertation

UNIVERSITY OF CALIFORNIA

Los Angeles

Non-Equilibrium in the Mars Entry Shock Layer Characterized via Laser Absorption Spectroscopy

A dissertation submitted in partial satisfaction of the
requirements for the degree Doctor of Philosophy
in Aerospace Engineering

by

Christopher Jelloian

2022

ABSTRACT OF THE DISSERTATION

Non-Equilibrium in the Mars Entry Shock Layer Characterized via Laser Absorption Spectroscopy

by

Christopher Jelloian
Doctor of Philosophy in Aerospace Engineering
University of California, Los Angeles, 2022
Professor Raymond M. Spearrin, Chair

Predicting and managing heat transfer during planetary entry is a critical engineering challenge for current and future space exploration missions. This work aims to improve the understanding of thermodynamic non-equilibrium during Mars entry via experimental studies to capture chemical kinetics and the rates of energy transfer between translation, rotation, and vibration for the dominant molecular species (CO_2 and CO). The key elements of this research can be split into two distinct phases: (1) develop and demonstrate non-equilibrium high speed sensing of CO and CO_2 on a high enthalpy shock tube at UCLA. (2) Deploy the sensor at NASA Ames on a representative Mars entry flow. A mid-infrared laser absorption strategy for simultaneous measurement of translational, rotational, and vibrational temperatures of carbon monoxide (CO) at high speeds was developed for application to high temperature non-equilibrium environments relevant to Mars atmospheric entry. The sensing strategy is shown to resolve each targeted transition with temporal and spectral resolution sufficient for quantitative multi-temperature measurements over a wide range of temperatures and pressures (2100 - 5500 K, 0.03 - 1.02 atm), including behind incident shock waves

traveling up to 3.3 km/s. A similar strategy is employed on CO_2 transitions from the $\nu_3(00^00)$ and $\nu_3(01^10)$ states. Vibrational relaxation times were resolved at temperatures relevant to Mars backshell heating (2,000 - 3,000 K) in various CO_2 - Ar mixtures and found to be in good agreement with the Simpson rate model. The final effort of this project deployed a multi-species sensor on the Electric Arc Shock Tube facility at NASA Ames to study a recreated shock layer similar to that experienced on the Mars2020 mission. Temperature and number densities of CO_2 and CO were extracted from the data and compared to various chemistry models and a simultaneous emission measurement. At shock velocities below 3.1 km/s, the agreement between the measurements and the Johnston mechanism is typically within 5% for temperature and within 10% for number density. At shock velocities above 3.1 km/s, the CO_2 measurement becomes sensitive to a thin boundary layer and corrections of this effect are presented. On test cases with enough energy to dissociate CO_2, a quantum cascade laser scanned the P(2, 20), P(0, 31), and P(3, 14) transitions of the CO fundamental band at 4.98 µm. CO formation rate is measured to be close to the Johnston kinetic mechanism at low velocities, and then trending towards the Cruden kinetic mechanism at high velocities. In summary, this work has advanced laser absorption techniques to include high speed (MHz) multi-temperature measurements of CO_2 and CO on non-equilibrium flows relevant to Mars planetary entry.

The dissertation of Christopher Jelloian is approved.

Ann R. Karagozian

Richard E. Wirz

Xiaolin Zhong

Raymond M. Spearrin, Committee Chair

University of California, Los Angeles

2022

DEDICATION

To God, the Father of light,

thank You for shining in our hearts, minds,

and throughout all creation.

May we walk with You, our Father, forever.

TABLE OF CONTENTS

LIST OF FIGURES

Page

LIST OF SYMBOLS

A	pre-exponential factor
A_{21}	Einstein A coefficient of spontaneous emission [s^{-1}]
B_{21}	Einstein B coefficient of stimulated emission [$cm^3/(erg \cdot s^2)$]
B_{12}	Einstein B coefficient of absorption [$cm^3/(erg \cdot s^2)$]
B_λ	spectral blackbody emission intensity [$W/(cm^2 \cdot \mu m \cdot sr)$]
c	speed of light [cm/s]
c_2	second radiation constant [cm/K]
c_p	heat capacity at constant pressure [$J/(kg \cdot K)$]
D_{rot}	rotational degrees of freedom
E_a	activation energy [erg]
E_i	energy of level i [cm^{-1}]
$E_{\mathrm{rot},i}$	rotational energy of level i [cm^{-1}]
$E_{\mathrm{vib},i}$	vibrational energy of level i [cm^{-1}]
E_tr	translational energy [erg]
E_rot	rotational energy [erg]
E_vib	vibrational energy [erg]
e_vib	vibrational energy per volume [erg/cm^3]
g_i	degeneracy of level i
$g_\mathrm{rot,i}$	rotational degeneracy level i
$g_\mathrm{vib,i}$	vibrational degeneracy of level i
h	Planck's constant [$(cm^2 \cdot g)/s$]
h_0	stagnation enthalpy [J/kg]
h_f^0	enthalpy of formation [J/kg]
h_{vib}	enthalpy contribution from vibrational energy [J/kg]
I_t	transmitted light intensity [W/m^2]

I_0	incident light intensity [W/m^2]
I_λ	spectral intensity [W/(cm$^2 \cdot \mu$m $\cdot$ sr)]
I_λ^o	incident spectral intensity [W/(cm$^2 \cdot \mu$m $\cdot$ sr)]
J''	lower state rotational quantum number
k	Boltzmann constant [erg/K]
k	thermal conductivity (appears in Ch4) [W/(m $\cdot$ K)]
L	pathlength [cm]
M	molecular weight [g/mol]
n	collisional broadening coefficient of temperature dependence
n_A	number density of absorbing molecule A [molec/cm^3]
N	number of molecules [molec]
N_i	population of level i
P	pressure [atm]
Q	partition function
Q_{tr}	partition function of translation
Q_{rot}	partition function of rotation
Q_{vib}	partition function of vibration
R	area ratio of the transitions
R	gas constant (appears in Ch4) [J/(kg $\cdot$ K)]
S_j	linestrength of transition j [cm^{-1}/(molec $\cdot$ cm^{-2})]
S_k	second coefficient of the Sutherland law for thermal conductivity [K]
S_μ	second coefficient of the Sutherland law for viscosity [K]
T	temperature [K]
T_{tr}	translational temperature [K]
T_{rot}	rotational temperature [K]
T_{vib}	vibrational temperature [K]
T_{el}	electronic temperature [K]

T_{e}	temperature outside of boundary layer [K]
t	time [μs]
$t_{particle}$	particle time [μs]
t_{lab}	lab time [μs]
u	flow velocity in the x direction [m/s]
u_2	flow velocity behind the incident shock (shock fixed frame of reference) [m/s]
U_{is}	incident shock wave velocity [m/s]
v	flow velocity in the y direction [m/s]
v''	lower state vibrational quantum number
X	mole fraction
α	absorbance
α_λ	volumetric absorption coefficient [cm^{-1}]
γ_{A-B}	collisional broadening coefficient [cm^{-1}/atm]
$\Delta\nu_C$	collisional (Lorentzian) FWHM [cm^{-1}]
$\Delta\nu_D$	Doppler (Gaussian) FWHM [cm^{-1}]
δx_i	uncertainty in variable x_i
δ_{99}	boundary layer thickness [mm]
Θ_{vib}	characteristic temperature of vibration [K]
μ	reduced mass [g]
μ	dynamic viscosity (appears in Ch4) [$\mathrm{N} \cdot \mathrm{s}/\mathrm{m}^2$]
ν_0	transition linecenter in wavenumber [cm^{-1}]
ν	wavenumber [cm^{-1}]
ρ	density [kg/m^3]
τ_{VT}	vibrational relaxation time [μs]
ϕ	lineshape function [cm]
$\mathcal{A}_i$	absorbance area of transition i [cm^{-1}]

ACKNOWLEDGMENTS

I would like to thank all of the individuals who have helped me in my education. First, I would like to thank my adviser, Prof. Mitchell Spearrin, for giving me the opportunity to work in the Laser Spectroscopy and Gas Dynamics Laboratory at UCLA. It has been a blessing to be a part of your lab and to watch it grow. I look forward to what the future holds for your research group. Prof. Karagozian, Prof. Wirz, and Prof. Zhong, thank you for your mentorship and for teaching outstanding classes that I have enjoyed very much including: Compressible Flows, Rocket Propulsion Systems, Hypersonics, and Plasma and Ionized Gases.

I would like to thank my mentors at NASA Ames Research Center for their support. Dr. Megan MacDonald, it has been a privilege to get to work with and learn from you. Thank you for your guidance and patience in navigating the technical challenges of this work and for supporting me at UCLA in addition to the visits at NASA Ames. Dr. Brett Cruden, thank you for your expertise and mentorship throughout this work. I have learned so much from you about planetary entry and the state-of-the-art experiments and modeling taking place at Ames. Dr. Augustin Tibere-Inglesse, it has been a privilege to work with you. I am very thankful for your efforts on my behalf and for your kindness and support during my visits to Ames. In my book, there are no better NASA collaborators than the three of you. My sincerest thank you! Additionally, thank you to Dr. Aaron Brandis, Dr. Dinesh Prabhu, and Jeff Hill from the NASA Ames Aerothermodynamics branch for your interest and support. Ramon Martinez, and the rest of the EAST facility staff at the NASA Ames Thermophysics Facilities branch, thank you for your outstanding support and expertise throughout this project.

I would like to thank the NASA Space Technology Mission Directorate for funding this work through Grant No. 80NSSC18K1158 and Grant No. 80NSSC21K0066. The NASA Space

Technology Research Fellowship (NSTRF/NSTGRO) Program is phenomenal. I hope the program grows and more opportunities become available for students as time goes on.

I would like to thank my undergraduate faculty mentor, Dr. John Deisz at California Lutheran University. Thank you for guiding me in my studies as a physics major and for inspiring me to pursue graduate studies.

I would like to thank all of my colleagues with the SpearrinLab group that I have worked: Nicolas Minesi, Fabio Bendana, Chuyu Wei, Daniel Pineda, Daniel Lee, Kevin Schwarm, Anil Nair, Nick Kuenning, Isabelle Sanders, Alex Keller, David Morrow, Barathan Jeevaretanam, and Miles Richmond. I have learned so much from you all, and you have made each day fun and exciting.

Lastly, I would like to thank my family for their constant love and support. To my sister and brother, you inspire me to be a better person every day. To my mom and dad, thank you for all you have done for me. To my Uncle Paul, thank you for being an outstanding role model in my life, and for teaching me how to MacGyver solutions.

VITA

Christopher Jelloian

B.S. in Physics (2012 - 2016)

California Lutheran University, Thousand Oaks, CA

M.S. in Aerospace Engineering (2016 - 2018)

University of California, Los Angeles (UCLA), Los Angeles, CA

Ph.D. Candidate in Aerospace Engineering (2018 - 2022)

University of California, Los Angeles (UCLA), Los Angeles, CA

Peer Reviewed Archival Publications

[1] **Jelloian, C. C.**, Bendana F. A., Wei C., Spearrin, R. M., MacDonald, M. E. (2021). Nonequilibrium Vibrational, Rotational, and Translational Thermometry via Megahertz Laser Absorption of CO. AIAA Journal of Thermophysics and Heat Transfer. https://doi.org/10.2514/1.T6376

[2] Nair, A. P., Minesi, N. Q., **Jelloian, C. C.**, Kuenning N., Spearrin, R. M. (2022). Extended tuning of distributed-feedback lasers in a bias-tee circuit via waveform optimization for MHz-rate absorption spectroscopy. Measurement Science and Technology 33 105104. https://doi.org/10.1088/1361-6501/ac7b13

[3] Minesi, N. Q., Richmond, M. O., **Jelloian, C. C.**, Kuenning N., Nair, A. P., Spearrin, R. M. (2022). Multi-line Boltzmann regression for near-electronvolt temperature and CO sensing via MHz-rate infrared laser absorption spectroscopy. Applied Physics B. https://doi.org/10.1007/s00340-022-07931-7

[4] **Jelloian, C. C.**, Minesi, N. Q., Spearrin, R. M. (2022). High-speed mid-infrared laser absorption spectroscopy of CO2 for shock-induced thermal non-equilibrium studies of planetary entry. Applied Physics B.
https://doi.org/10.1007/s00340-022-07934-4

Chapter 1

Introduction

1.1 Planetary Entry Flows

Planetary entry aerothermodynamics have been a key area of interest since the 1950s and the race to the moon. The design of mass-efficient thermal protection systems (TPS) for planetary entry probes and Earth return vehicles require accurate modeling of the shock layer temperatures, pressure, composition, and radiation. These flow properties are dictated by the thermochemical characteristics of the planetary atmosphere and the entry velocity of the vehicle. Earth shock layers are composed of an N_2 - O_2 plasma that forms around the vehicle, while the Mars shock layer is characterized by a CO_2 - CO - N_2 plasma. CO forms due to thermal dissociation of CO_2, and becomes significant as the Mars atmosphere is approximately CO_2 (95%) with small amounts of N_2 (3%) and Ar (2%), along with other trace gases (O_2, CO, and H_2O) [21]. The Mars shock layer is the focus of this work, as the robotic exploration of Mars has become an increasingly popular scientific endeavor due to advances in many fields, namely, large reusable rockets (lower cost, larger payload capacity) and proven Entry Decent and Landing (EDL) technologies driving a desire to land larger

Table 1.1: List of Mars Entries

Mission Name	Agency	Payload Mass [kg]	Entry Velocity [km/s]	Transit Time [days]	Entry Date	Notes
Mars 2	USSR	2670	6.0	192	Nov. 27 1971	Crashed
Mars 3	USSR	2670	5.7	188	Dec. 2, 1971	20s of operation
Mars 6	USSR	1400	5.6	219	Mar. 12, 1974	Crashed
Viking I	NASA	1261	4.5	335	Jul. 20, 1976	
Viking II	NASA	1261	4.5	361	Sep. 3, 1976	
Pathfinder	NASA	1257	7.5	213	Jul. 4, 1997	
MPL	NASA	639	6.9	335	Dec. 3, 1999	Failed
DS-2	NASA	8	6.9	335	Dec. 3, 1999	Lost
Beagle	ESA	73	5.6	207	Dec. 25, 2003	Lost
MER-A	NASA	1808	5.6	209	Jan. 3, 2004	
MER-B	NASA	1808	5.6	203	Jan. 24, 2004	
Phoenix	NASA	770	5.5	296	May 25, 2008	
MSL	NASA	1982	5.8	255	Aug. 6, 2012	
Schiaparelli	ESA/RSA	1272	5.8	220	Oct. 19, 2016	Crashed
InSight	NASA	789	5.5	206	Nov. 26, 2018	
Mars2020	NASA	2260	5.6	204	Feb. 18, 2021	

and more massive vehicles on the surface. A catalogue of Mars entry missions are presented in Table 1.1 to give an idea of the payload mass and typical entry velocities.

State of the art computational fluid dynamics (CFD) codes are utilized by mission planners to determine the material type and thickness of a thermal protection system (TPS) for use on a potential mission. It is important to design the TPS to be effective over a range of entry conditions (varying angle of attack, entry velocity, atmospheric conditions, etc.) to increase the general robustness of the heatshield in case an unforeseen event occurs during the mission. Additionally, the TPS is a significant part of the entry vehicle weight and required for surface access, though it is often discarded during the landing sequence or shortly after touchdown. Even though recent missions have flown entry, descent, and landing (EDL) instrumentation for measurements along the decent through the atmosphere [54, 99], the TPS is a minimal contributor to the science goals of most missions, therefore the forebody and backshell should be efficiently designed (mass-minimized) to maximize scientific payload

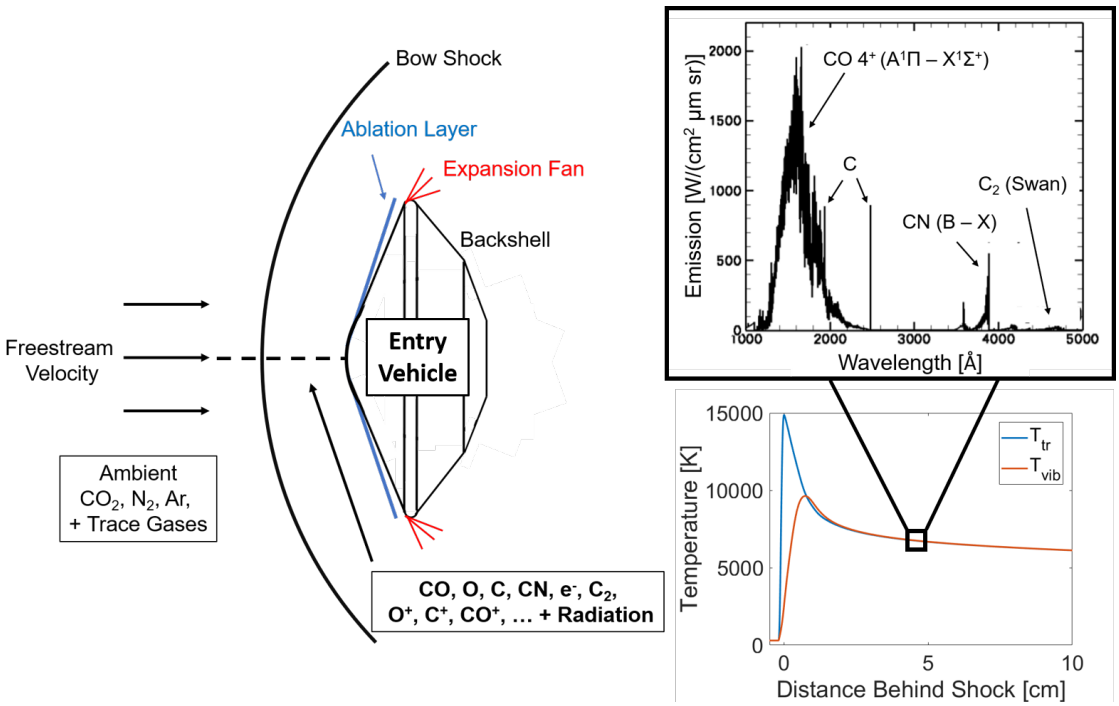

Figure 1.1: Entry flow diagram shown with simulated equilibrium radiation (taken from [102]) and simulated non-equilibrium temperature profile from Data Parallel Line Relaxation Code (DPLR) [104]

delivered to the surface. Mission planners make use of modern CFD methods that enable heat load and shear stress encountered by the vehicle through EDL to be characterized over the entire vehicle (forebody + backshell) and across a wide range of trajectories.

1.2 Modeling and Simulation Techniques

The field of aerothermodynamics relies on two key approaches: 1) simulation of the environment and 2) experimental investigations of the flow and material response in partially similar flow fields. These approaches must be taken together to ensure the simulation accuracy and maximize the data's predictive power to infer flow behavior at conditions that were not directly experimentally investigated.

CFD is coupled with chemical kinetic models to generate predictions of the time evolution

of the state variables (temperature, pressure, entropy, chemical composition, etc.) of the reacting flow system. These parameters are necessary to predict the thermal and radiation environment in the shock layer. From the molecular theory of gases [94], temperature is understood to describe a Boltzmann population distribution over available energy states in the gas as shown in Eq. 1.1. N_i, g_i, and E_i are the population, degeneracy, and energy of level i respectively. c_2 is the second radiation constant.

$$\frac{N_i}{N} = \frac{g_i \exp\left(\frac{-c_2 E_i}{T}\right)}{Q(T)} \tag{1.1}$$

N is the total population, and $Q(T)$ is the partition function at temperature T (shown in Eq. 1.2).

$$Q(T) = \sum_i g_i \exp\left(\frac{-c_2 E_i}{T}\right) \tag{1.2}$$

The partition function represents all available energy states of the gas at temperature T and can be calculated once the energies and degeneracies of each level are known. The accuracy of the partition function calculation is tied directly to the accuracy of the fundamental spectroscopic parameters (anharmonicity constants and centrifugal distortion terms) of each species. Additionally, chemical reaction rates are often modeled with the modified Arrhenius equation shown in Eq. 1.3 where A is the pre-exponential factor, T_x^n captures the temperature dependence of A, E_a is the activation energy of the reaction and k is the Boltzmann constant.

$$k = A T_x^n \exp\left(\frac{-E_a}{kT}\right) \tag{1.3}$$

These molecular and chemical rate constants are often determined experimentally and can sometimes be calculated a priori from the theory quantum mechanics. These constants may have significant uncertainties when modeling excited electronic states of some molecules, or

extrapolating experimental fits into new temperature regimes where no data is available. Lastly, a single temperature may not be able to accurately describe the population distribution present in the gas. When atmospheric molecules cross the bow shock of an entry vehicle, the translational and rotational energy modes excite very rapidly and equilibrate quickly. The vibrational and electronic energy modes lag behind due to higher characteristic temperature [94, 72, 58]. When this occurs there are two common approaches to model the non-equilibrium: 1) Multi-temperature models (such as [72, 14, 37]) describe the thermal state of the gas, allowing each energy mode (translation, rotation, vibration, electronic) to be described by Boltzmann population distributions at different temperatures. 2) State-to-state models (such as [92, 43]) assume no Boltzmann distributions and each energy level population is modeled with rate equations into and out of the state.

1.2.1 Multi-Temperature Models

Multi-temperature models have historically been used to simulate non-equilibrium. In this computationally inexpensive method, developed by Bethe and Teller in 1940 [5], a temperature is defined over each of the available energy modes of the gas. Atoms possess two modes of storing energy:

- kinetic motion (translation), described by the temperature of translation, T_{tr}.
- electronic excitation, described by the electronic temperature T_{el}.

Molecules possess the aforementioned modes and the additional modes:

- rotation, described by the rotational temperature, T_{rot}.
- vibration, described by the vibrational temperature T_{vib}.

The available modes of rotation and vibration depend on the complexity of the molecular structure and chemical rates can be defined in typical Arrhenius form with a temperature dependence on a specific mode or a combination of modes. This was done extensively by Park et al. in the models of Earth [71] and Mars [72] entry and is still used in the Johnston and Cruden mechanisms of planetary entry [37, 14]. For example, a diatomic molecule such as CO has 2 principle axes of rotation and one bond that can vibrate. If independent Boltzmann distributions (i.e. temperatures) are assumed over each mode, CO can be described in non-equilibrium by 4 temperatures (T_{tr}, T_{rot}, T_{vib}, and T_{el}). A linear polyatomic molecule such as CO_2 is more complicated, but a multi-temperature approach can still be valid as long as all of the modes are properly accounted for. CO_2 possess two axes of rotation and two vibrational bonds that result in 3 separate modes of vibration able to store energy. The vibrational modes are symmetric stretch, bending (which is doubly degenerate), and asymmetric stretch. The CO_2 molecule is therefore described in non-equilibrium by six temperatures (T_{tr}, T_{rot}, $T_{vib,1}$, $T_{vib,2}$, $T_{vib,3}$, and T_{el}).

Vibrational energy exchange in the gas is mediated via collisions between molecules and can be categorized as vibration-vibration (VV) exchange or vibration-translation (VT) exchange. VV exchange occurs when a vibrationally excited molecule collides and transfers some of its vibrational energy to the vibrational energy mode of another molecule. VT exchange occurs when the kinetic energy from a collision (translational energy) transfers to the vibrational energy mode of one of the collision partners. Models often consider the relative timescales of each process and VV exchange frequently occurs on timescales faster than VT exchange [44]. For diatomic species the Bethe-Teller equation is often used to model the vibrational energy change with time (Eq. 1.4).

$$\frac{\mathrm{d}E_{\mathrm{vib}}}{\mathrm{d}t} = \frac{E_{\mathrm{vib}}(T_{\mathrm{tr}}) - E_{\mathrm{vib}}(T_{\mathrm{vib}})}{\tau_{VT}} \tag{1.4}$$

$E_{vib}(T_{tr})$ is the vibrational energy of the molecule if the vibrational mode was at the at

the current T_{tr}, $E_{vib}(T_{vib})$ is the current vibrational energy of the molecule, and τ_{VT} is the vibrational relaxation time. τ_{VT} is often determined experimentally [59, 79], however Millikan and White [59] have a widely used model of τ_{VT} based on the the reduced mass of the collision partners (μ), characteristic temperature of the oscillator, and a length parameter which attempts to capture the collisional interaction potential. The Millikan and White expression is shown in Eq. 1.5, where C_1 is often experimentally determined.

$$p\tau_{VT} = \exp\left[C_1(T^{-1/3} - 0.015\mu^{1/4}) - 18.42\right] \tag{1.5}$$

There is interest in addressing the uncertainties in this expression and often improvements are made via fitting a linear relation as shown in Eq. 1.6 to experimental measurements of relaxation time.

$$log(p\tau_{VT}) = C_1 T^{-1/3} + C_2 \tag{1.6}$$

For mixtures the relaxation time is calculated via Eq. 1.7, where X_b is the mole fraction of diluent b.

$$(\tau_{VTmix})^{-1} = \sum_b \frac{X_b}{\tau_{VT,a-b}} \tag{1.7}$$

The above relations for vibrational energy transfer and relaxation timescales are regularly used in CFD models of planetary entry.

The Park chemical mechanism [72] is an example of a multi-temperature approach to model the Mars entry shock layer. Park uses a two temperature model by assuming that the translational and rotational modes of the gas are in equilibrium ($T_{tr} = T_{rot}$) and the vibrational and electronic modes of the gas are in equilibrium ($T_{vib} = T_{el}$) but not necessarily equal to $T_{tr,rot}$. The Park mechanism accounts for 23 species and 35 reactions modeled in modified Arrhenius form (Eq.1.3). The temperature T_x [K] is either translation-rotation, vibration-

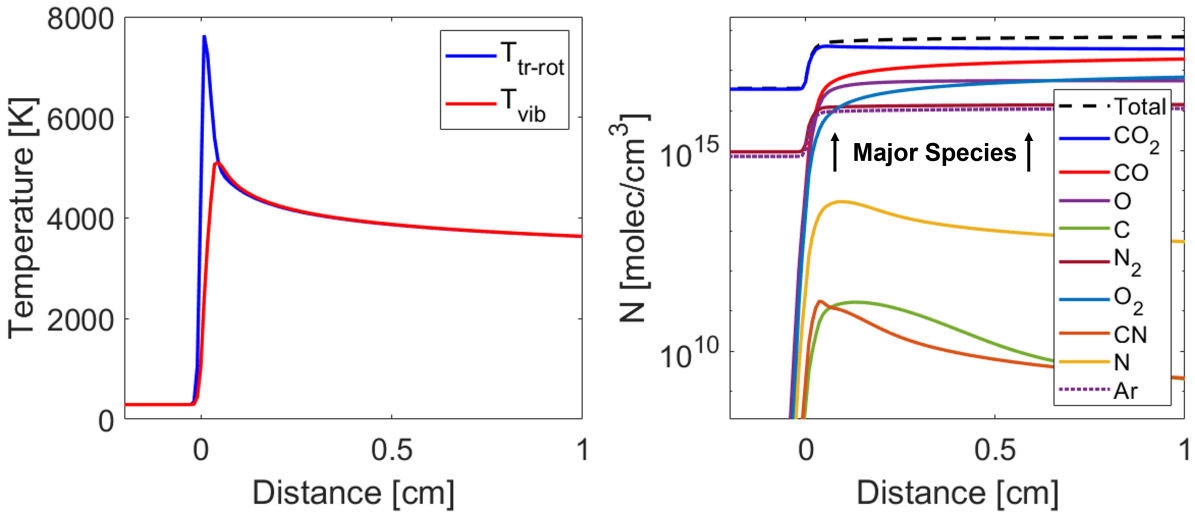

Figure 1.2: Multi-temperature simulation of the stagnation line of a Mars entry using DPLR [104]. (left) Stagnation line temperature profile (assuming $T_{tr} = T_{rot}$) vs distance behind shock front. (right) Species number density vs distance behind shock front.

electronic, or the quadratic mean of the two temperatures ($\sqrt{T_{tr}T_{vib}}$). The pre-exponential factor and pre-exponential temperature dependence (T_x^n) can be interpreted as the collision frequency and probability of the reaction occurring. This chemical reaction mechanism can be input into a CFD code to simulate a chemically reacting flow.

While there are many CFD codes available to model this flow, NASA has mainly utilized the Data Parallel Line Relaxation (DPLR) [104] developed and maintained by NASA Ames and Langley Aerothermodynamic Upwind Relaxation Algorithm (LAURA) [25] developed and maintained by NASA Langley for the study of aerothermal entry environments. Recently, NASA has also developed the US3D [11] code in conjunction with the University of Minnesota as the next-generation DPLR code to utilize unstructured grids around the entry vehicle. All of these codes [104, 25, 11] subtly differ in their transport models and solution methods. Hash et al. [33] compare these CFD codes to each other and to flight data from the Fire II mission, a significant Earth entry experiment. At most, a 7% difference was found in the convective heating result between all three codes, however greater differences were found in the radiative heating estimation as the radiative heating component is more sensitive

to the multi-temperature model employed. In summary, the CFD methods are well known however accuracy of the aerothermal environment simulation largely depends on the chemical mechanism and relaxation models used as input to the CFD.

1.2.2 Radiation Models

To solve the radiation environment of this flow, NASA deploys two codes: Non-EQuilibrium Air (NEQAIR) [101] and High-temperature Aerothermodynamic RAdiation (HARA) [39]. NEQAIR is a line-by-line radiation code that is capable of simulating emission or absorption spectra along a line of sight utilizing the radiative transport equation as shown in Eq. 1.8, and the gas slab approximation. I_λ is the spectral intensity [W/(cm$^2 \cdot \mu$m $\cdot$ sr)], I^0_λ is the incident spectral intensity from the previous gas slab, and B_λ [W/(cm$^2 \cdot \mu$m $\cdot$ sr)] is the spectral blackbody emission intensity. α_λ [cm^{-1}] is the volumetric absorption coefficient within the layer, L [cm] is the gas slab width.

$$I_\lambda = I^0_\lambda \exp\left(-\alpha_\lambda L\right) + B_\lambda(1 - \exp\left(-\alpha_\lambda L\right)) \tag{1.8}$$

The NEQAIR input, typically from a CFD code, includes location along the line of sight, species number densities, and temperatures within each slab. Non-equilibrium spectral predictions are produced using a multi-temperature model (T_{tr}, T_{rot}, T_{vib}, and T_{el}). Lastly, NEQAIR is capable of modeling non-Boltzmann electronic spectra using the quasi steady state (QSS) approximation (discussed in [70]). QSS assumes that the radiation timescales are much faster than flow timescales. The HARA code was developed after the NEQAIR code and aimed to accurately and efficiently couple the CFD flow solvers in use by NASA to a radiative code. HARA produces similar results to NEQAIR along a single line of sight, but the databasing schemes employed for radiation predictions are different and more inclined to handle complex 2D and 3D flow geometries. In summary, these CFD codes [104, 25, 11]

when coupled with a radiation code [101, 39] provide a comprehensive description of the aerothermal environment around the entry vehicle.

Recently, different spectral tools such as SpectraPlot [27] and RADIS [69] have been developed to estimate emission and absorption from the HITRAN [29], HITEMP [75], CDSD [87], and ExoMol [89] databases. These tools are valuable for vibrational spectroscopy, particularly in the sensor design process but are not typically used in the investigation of planetary entry flow radiation, though the non-equilibrium model of CO_2 employed in RADIS [69] was validated against the NEQAIR [101] model. The spectroscopic models employed in these codes [27, 69] are very applicable to planetary entry radiation, however caution must be exercised as there is a question of the validity of some of the database parameters at these extreme temperature conditions. These tools and methods are very valuable in the fitting of spectroscopic data, as similar codes can be easily implemented with updated partition functions, collisional broadening coefficients, lineshape functions etc. to produce quantitative results for a set of experimental data.

1.2.3 State-to-State Models

The state-to-state model is a much more computationally expensive endeavor when compared to the multi-temperature method but eliminates the need for a Boltzmann assumption over the internal energy modes of the gas. In this method each energy level of the gas is treated as its own species as illustrated in Fig. 1.3, where $k_{i,i+1}$ represent the rate of population transfer from level i to i+1. All the excitation and quenching processes within the vibrational modes must be accounted for, however, the rates of energy transfer are poorly known for many states. Refined state-to-state models also consider electronic and rotational excitation/quenching. Thus, a full state-to-state model is rarely pursued, but simplified models can be useful, especially when modeling spectroscopic data. The absorption data collected

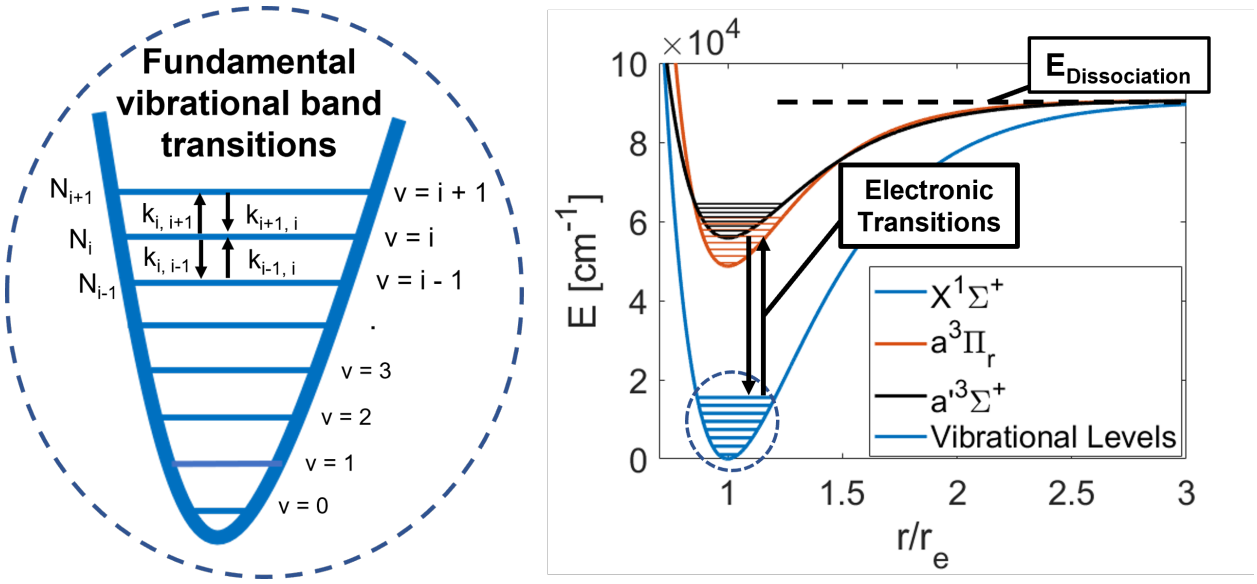

Figure 1.3: State to state representation of CO. (left) Vibrational transitions into and out each level. (right) Electronic potential wells of the three lowest electronic states with vibrational bands displayed for the low lying vibrational levels of each energy well. The dissociation energy for these states is near 90,600 cm^{-1}.

in this work could be used to investigate both multi-temperature and state-to-state models of planetary entry.

The recent work of Vargas et al. [92] has produced a detailed state-to-state model for the vibrational excitation and dissociation of CO_2. The classical approach of Schwartz-Slawsky-Herzfeld (SSH) theory [78] was critiqued for providing inaccurate rates of population transfer in the high lying states. SSH theory scales low lying state-to-state rates to higher levels and is insufficient for modeling the complicated rovibronic structure of CO_2. To lower computational cost, Vargas et al. consider only one electronically excited state: $CO_2(^3B_2)$. This state is of primary importance because, through $CO_2(^3B_2)$, the molecule can dissociate by overcoming two energy barriers, which are small compared to the 7.2 eV required to directly dissociate CO_2 in one step. At low temperature, two weak energy transfer events via collisions is more likely than one strong energy transfer event for direct dissociation from the ground electronic state. The final model developed by Vargas et al. includes 22,569 reactions using a combination of rates published in literature from experimental data and

rates determined from forced harmonic oscillator theory [1]. It considers 201 vibrational levels of CO_2, 2 electronic states of oxygen, and 11 species in total. Kustova and Kosareva et al. [46, 45, 43] have also developed a state-to-state model investigating both vibrational excitation and dissociation in shock heated CO_2 flows. They investigate the characteristic times of vibrational relaxation in CO_2 and their effect on other properties such as bulk viscosity and dissociation rate. The state-to-state models described above are well beyond the scope of this work, however the relaxation pathways that these works highlight are very applicable to the interpretation of the spectroscopic data collected and discussed in Ch. 2 - 4.

In summary the multi-temperature and state-to-state approach are both valuable tools that can be accurate provided the assumptions of the relaxation times and chemical rates are correct. Experimental verification and validation efforts are needed to confirm or refine the thermochemical rates employed in these models for upcoming and future Mars missions.

1.3 Recent Challenges and Experimental Needs

Mars has become a significant target for planetary exploration missions and there is a strong desire to land larger and heavier payloads on the surface at higher entry velocities ($>$ 7 km/s). Increasing speed and mass will lead to an increase of the total heat load on the capsule. The heaviest payloads to land on Mars to date are the Mars Science Laboratory (MSL - Curiosity) and the Mars2020 rover (Perseverance) with masses of 1,982 lbs and 2,260 lbs respectively. Infrastructure necessary to support human exploration on the surface such as a return vehicle, base structure, etc. will require masses an order of magnitude larger to be safely and reliably delivered to the surface. Additionally the entry vehicles themselves will be larger (likely Hypersonic Inflatable Aerodynamic Decelerators - HIAD). Due to the size and weight of these payloads, radiative heating must be better characterized to safely

and efficiently land. While radiative heating scales approximately linearly with the size of the vehicle, radiative heating scales approximately exponentially with entry velocity [102]. The desire to increase the entry velocity of Mars vehicles stems from the desire to minimize the flight time for a possible crewed mission. A faster transit time between Earth and Mars is advantageous to reduce the amount of resources required for the flight (food and water), reduce the radiation dose experienced by the crew, and gain science time on the surface of the planet. The fastest probe to enter the Martian atmosphere was the Pathfinder rover with an entry velocity near 7.5 km/s. Radiative heating is predicted to have contributed roughly 8% to the total heat load experienced by the vehicle (10 W/cm^2 of 125 W/cm^2) [102]. Recent rovers such as the Mars exploration rovers (Spirit and Opportunity), MSL, InSight, and Mars2020 enter the atmosphere at velocities between 5.0 - 6.0 km/s. Convective heating dominates this flight regime and is generally well understood for the current class of payloads heading for the surface [102].

Additionally, aerocapture trajectories are being studied as a way to increase the mass delivered to the planet. A spacecraft on an aerocapture trajectory does not need to propulsively decrease its energy to enter orbit, which implies that less fuel is needed and thus more equipment and supplies can be delivered in one trip. The craft will fly through the upper atmosphere of the planet and use the drag force it experiences to be captured into orbit around the planet. Then, at apogee, a small boost from the rocket is needed to raise the periapsis out of the atmosphere and into a safe orbit. The entry velocities during aerocapture are extremely fast and robust models of the flow chemistry and radiation are needed to support these flight paths.

Lastly, it was discovered from a combination of theoretical and experimental studies [8] that the backshell of Mars entry vehicles experience higher than predicted radiative heating. Even though the backshell experiences less heat than the forebody, this energy needs to be well characterized because the backshell is a different thickness and often a different

material than the forebody heat shield. Brandis mentions that accurate understanding of the CO_2 midwave-IR vibrational bands will influence future safety margin policies for backshell design [8]. The desire to (i) land larger and heavier payloads on the surface, (ii) enter the atmosphere at higher speeds (ex. future crewed missions and aerocapture trajectories), and (iii) accurately predict backshell radiative heating in the Mars entry environment necessitate a better understanding of the non-equilibrium radiative processes that CO_2 and CO undergo in the shock layer. This work focuses on the development and deployment of novel non-equilibrium sensors to quantitatively characterize the Martian entry environment to better constrain models and sub-models currently used by NASA.

1.4 Recent Experimental Studies

It is extremely difficult to reproduce all the aspects of the planetary entry flow at once in a lab environment and hence different facilities have utilized a wide range of experimental techniques. The planetary entry environment has been studied in shock tubes [22, 3], arc-jets, plasma torches, free-flight facilities, and hypersonic wind tunnels. Spectroscopic emission and absorption techniques have historically been utilized to quantify flow properties (temperatures, pressures, composition, etc.) in these environments. This section describes notable recent experimental works by various groups and establishes the scientific foundation and framework for this dissertation.

The NASA Ames Electric Arc Shock Tube (EAST) facility is NASA's flagship shock tube for studying high temperature gas kinetics at planetary entry velocities. This facility is well documented in literature [15] and is briefly described below. A 1.25 MJ capacitor bank supplies energy for the electric arc driver. The facility is capable of generating incident shock velocities up to 46 km/s through the 30-foot driven section. Earth (N_2 - O_2), Mars/Venus (CO_2 - N_2), Titan (N_2 - CH_4), and outer planet entries (H_2 - He) have been studied in this

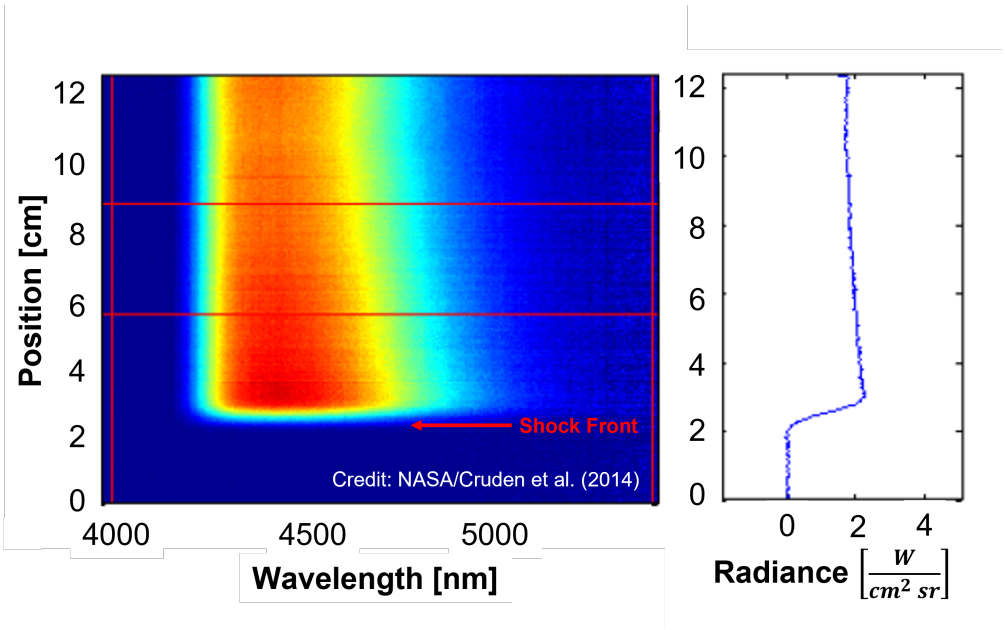

Figure 1.4: (left) Spectral emission and (right) radiance signal of the 4.3 μm band of CO_2 for a 3.03 km/s shock in 0.99 Torr of pure CO_2. The shock front is located just past 2 cm. Figure reproduced from [17].

facility via emission spectroscopy. Multiple chemical kinetic mechanisms have been developed at EAST to model CO_2/CO planetary entry flows including the Park [72], Johnston [37], and Cruden [17, 14] mechanisms. The facility is outfitted with multiple spectrometers that spatially and spectrally resolve wavelengths from the infrared to the vacuum ultraviolet (VUV). Sample CO_2 emission data is taken from Cruden et al. [17] and displayed in Fig. 1.4. The spectra are typically fit via NASA's radiation code NEQAIR [101]. Often temperatures and number densities are extracted from the emission signals and rate models are tuned accordingly. This is inherently difficult at low shock velocities as the emission signal is weak. Additionally, the emission signal must be calibrated after each test via an integrating sphere, blackbody, deuterium lamp, etc. to transform pixel position and intensity counts to wavelength and radiance [W/(cm$^2\cdot$ sr)]. Laser absorption measurements have the potential to complement the emission measurements due to their calibration free nature and high signal to noise ratio (SNR) at low velocities where emission is weak.

A recent study conducted by Cruden et al. (2018) [14] utilized the EAST facility to study

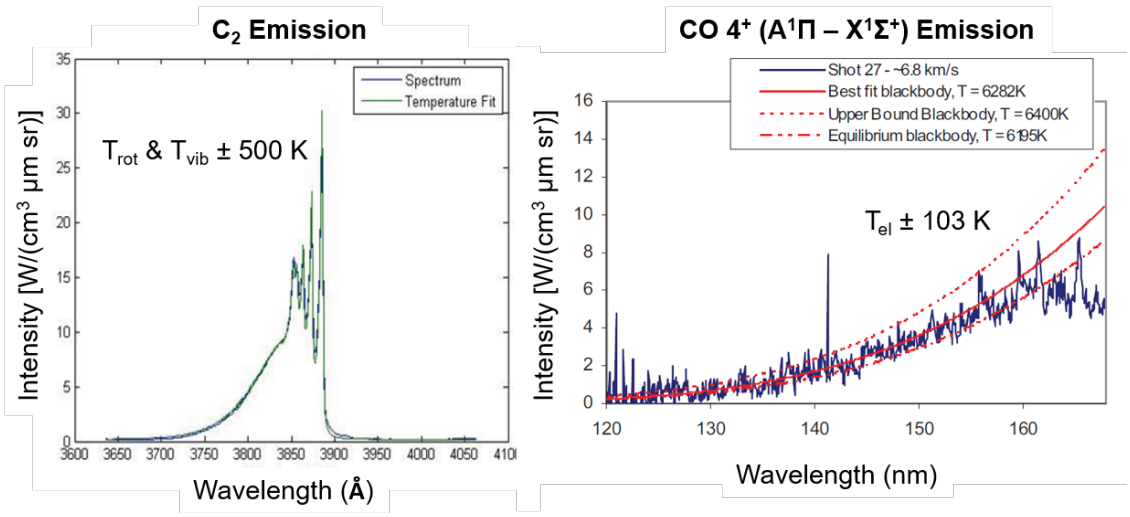

Figure 1.5: C_2 emission (left), and CO 4^+ emission (right) shown with the respective fits. Error estimated. Figures reproduced from Cruden et al. [13]

shock heated carbon monoxide with the goal of temporally resolving temperature relaxation to better model the dissociation rate of CO. Emission signals were utilized to spatially and spectrally resolve CO vacuum ultraviolet and mid-infrared bands. Atomic carbon and C_2 signatures were also observed in the visible wavelengths. Additionally a rovibrational transition of CO was measured during the tests and is described by MacDonald et al. (2018) in a companion paper [55]. Temperatures of rotation and vibration could not be extracted from the optically thick CO 4^+ band. The blackbody limited region of the CO 4^+ band was fit with a Planck function to obtain the electronic temperature of the test as shown in Fig. 1.5 (right). T_{rot} and T_{vib} were extracted from C_2 emission which is optically thin as displayed in Fig. 1.5 (left). Translational temperature was determined from the Doppler halfwidth of the CO R(0, 51) line measured via Tunable Diode Laser Absorption Spectroscopy (TDLAS). This method of measuring the C_2 vibrational temperature and applying it to the vibrational temperature of CO is not ideal but was the strongest band to fit that contained T_{rot} and T_{vib} information. Resulting temperatures for a sample test are shown in Fig. 1.6. It is observed that the laser absorption measurement of T_{tr} has significantly lower noise than the emission measurements of T_{rot} and T_{vib}.

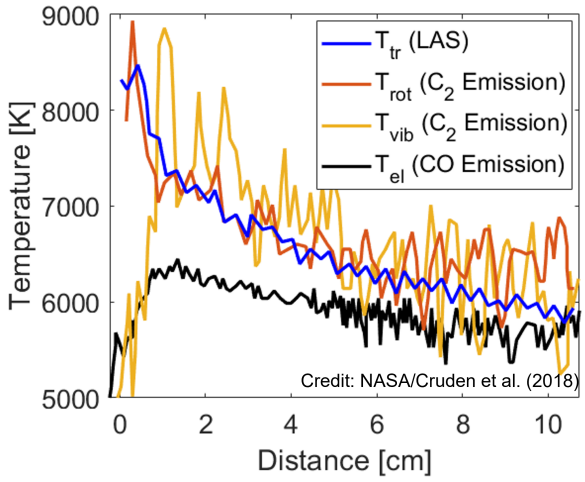

Figure 1.6: Non-equilibrium temperatures inferred for a 4.4 km/s shock in 100% CO. Figure reproduced from [14].

Cruden et al. used multiple kinetic mechanisms to model the flow and predict the subsequent radiation using NEQAIR [101]. They determined that at low shock velocities (< 6.6 km/s) CO dissociation likely proceeds through a metastable electronic state. CO infrared radiation intensity was demonstrated to be very sensitive to the rate of CO dissociation. At high incident shock velocities electron impact dissociation is suggested to play an important role which is not explicitly accounted for in either of the kinetic mechanisms investigated by Cruden. Additionally, Cruden et al. note the CO 4^+ band is poorly predicted at velocities above 7.5 km/s and attempts to fit the band using two different techniques, but a reasonable solution fails. This suggests further experimental efforts are needed to constrain the models of this flow.

Additionally, non-equilibrium CO_2 flows have been studied in plasma torches. In a CO_2 plasma torch experiment, the electronic energy of the gas excites rapidly, and energy cascades from the electronic mode to the vibrational modes of CO_2, first the asymmetric stretch mode and then the symmetric stretch and bending modes, and eventually to the rotational and translational modes. Klarenaar et al. [42] used Fourier-transform infrared spectroscopy (FTIR) to measure non-equilibrium temperatures of CO_2 and CO in a glow discharge. Klare-

naar provides a useful guide to fit non-equilibrium CO_2 and CO spectra from absorption data, and investigates a range of plasma torch conditions. The FTIR technique produces quantitative results, but requires a steady or repeatable flow and cannot be easily employed in fast-evolving single-shot shock tube experiments due to the slow measurement rate.

Emission diagnostics have also been utilized by various groups to measure spectral radiance and infer non-equilibrium temperatures of translation, rotation and vibration on plasma torches. Grimaldi et al. [30] studied a recombining CO_2 plasma with optical emission spectroscopy between 4.1 - 5.6 μm. They observed differences in CO_2 and CO rotational temperature and reported a vibrational temperature of CO_2. Emission diagnostics can also be employed to improve spectral simulations, see McGuire et al. [56] where several electric transition dipole models of the CO 4th positive system were compared to VUV experiments. These measurements are important, as CO emission from this band is very significant for Mars and Venus entries at high velocities on the forward heat shield [37, 14].

Among species generated during Mars entries, atomic oxygen is an important collision partner in the entry flows of Earth and Mars. On Mars it is created through the thermal dissociation of CO_2 described in Eq. 1.9.

$$CO_2 + M \rightarrow CO + O + M \tag{1.9}$$

O is an abundant species in the Mars entry flow and very efficient collision partner with CO_2 and CO. It is thought to drive much of the vibrational relaxation that occurs in the shock layer along with the chemistry [14]. A laser absorption diagnostic for O was developed by Nations et al. (2016) [65] and probed two electronically excited states ($^5S^0$ and $^3S^0$) using a diode feedback laser at wavelengths of 777.2 nm and 844.6 nm. Nations et al. deployed the sensor to determine heavy particle excitation rates of O. Reflected shocks were used to study a 1% O_2 - Ar mixture over the temperature range 5400 - 7500 K. Nations compared

the predicted electronic excitation rate coefficients from Drawin (1973) [19] to the measured rates and found Darwin's model to be 3 orders of magnitude off in opposite directions for each measured state. This highlights the importance of experimental confirmation of theoretical rates especially when using state-to-state models.

At high temperatures, the effect of electron collisions begins to dominate the plasma chemistry. Following the work of Nations et al., but at higher temperature, Li et al. (2021) [50] measured the Stark shift of atomic oxygen for the determination of the electron number density. The Stark shift is caused by an electric field which induces a Lorentzian broadening and a shifting of spectral lines. At the temperatures studied by Li et al., from 10,100 to 11,200 K, the ionization fraction increases and the Stark effect becomes prevalent in broadening features. The work of Nations and Li highlight the applicability of quantitative laser absorption techniques at temperatures of nearly 1 eV.

Non-equilibrium NO has been investigated by Girard et al. (2020) [23] in the T5 reflected shock tunnel at Caltech using laser absorption, with the goal to develop a diagnostic for use in hypersonics facilities to quantify the thermal state of the flow. NO is an important species in the understanding of Earth entry and often in hypersonics facilities such as arcjets, intrusive methods are used to measure the temperature. Typically, a probe is swept across the core flow at the beginning of each test. The data from these probes is often difficult to interpret and does not contain information on the vibrational temperature of the gas. Non-intrusive optical techniques (such as the one put forth by Girard et al. and the sensor described in this work) are a promising solution to not perturb the flow and to gain more information about the composition and thermal state of the flow (such as non-equilibrium temperatures) when compared with the traditional probe-sweep method. Girard et al. conclude with presenting measurements of T_{rot}, T_{vib}, and partial pressure of NO. Additionally, they detected a measurable amount of CO, and H_2O that was not expected in the flow.

In summary, state of the art emission and absorption techniques for studying high tempera-

ture non-equilibrium planetary entry flows have been reviewed and contextualized. Emission diagnostics provide estimations of the radiance, an important quantity for predicting radiative heat loads, however often it is difficult to relate radiance to the underlying kinetic rates. Laser absorption techniques have been shown to provide quantitative temperature and number density measurements especially in combustion flows [85, 81, 84, 83, 82, 77, 48, 49, 96], however these are mostly single temperature measurements. Aside from a small body of work on CO [9] and NO [23], multi-temperature laser absorption methods have rarely been utilized to study these planetary entry flows. The extreme temperature range, fast timescales (μs), and increased spectral modeling complexity have made multi-temperature measurements difficult, though it is likely they can reduce measurement noise and probe underlying chemical rates largely hidden from emission techniques. These techniques have been brought together to study Mars entry flows [52, 51], however rotational and vibrational temperatures were determined via CN violet emission. Non-equilibrium multi-temperature laser absorption methods are the subject of this dissertation and are demonstrated on CO_2 and CO (the two primary radiators of interest in the Mars shock layer). These measurements were enabled initially by work to increase the temporal resolution of these lasers from the 100s of kHz to the MHz range and have since been optimized [64] and deployed on other studies involving rotating detonation engines [62] where flow phenomena occur at μs timescales.

1.5 Our Approach: Laser Absorption Spectroscopy

Our approach to study Mars entry kinetics uses Laser Absorption Spectroscopy (LAS) in the mid-wave infrared to resolve individual spectral transitions to high fidelity. Recent advances in photonics have enabled the development of room temperature, single mode lasers at nearly any wavelength from the visible into the far infrared ($\sim$20 μm) [26]. These advancements in tunable light sources have been widely deployed in combustion environments

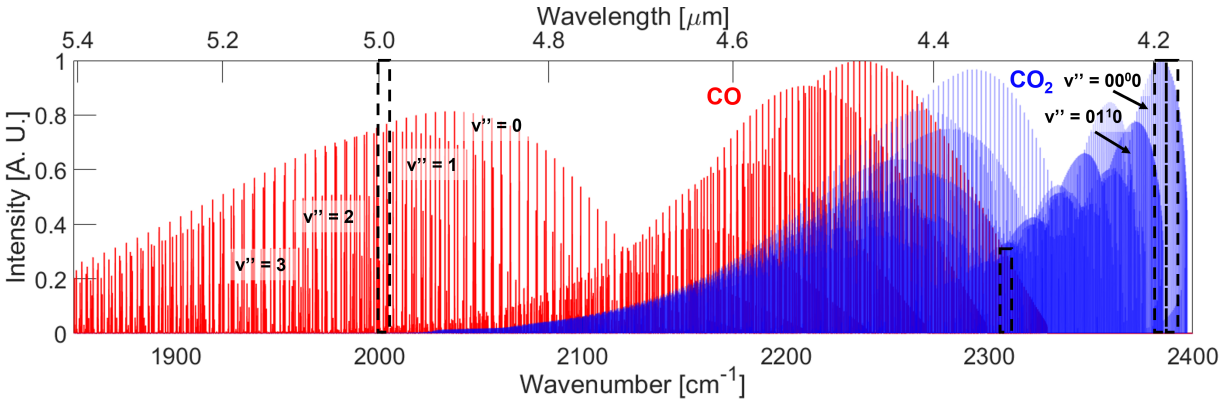

Figure 1.7: Linesurvey of CO_2 and CO mid-IR vibrational bands. The four wavelengths used in this work are highlighted by the boxed regions. Vibrational band structure is highlighted with lower state vibrational level (v") labeling. Three P branch CO lines near 2008 cm^{-1} were used as well as one R branch CO transition near 2314 cm^{-1}. For CO_2 two wavelengths were utilized near 2384 and 2396 cm^{-1} to resolve 8 features.

on a variety of species of interest (H_2O, CO_2, CO, NO, CH_4, NH_3). Additionally, these sensors are lightweight and portable for deployment on drones or easy integration on larger ground test facilities. This work adapts the mid-IR techniques and methods previously demonstrated on combustion flows for use on higher temperature, lower pressure planetary entry flows. Additionally, for the case of planetary entry, non-equilibrium between energy modes of translation, rotation, and vibration can complicate the LAS method. In this work, it is shown that T_{tr}, T_{rot}, and T_{vib} can be determined simultaneously by targeting spectral transitions from different vibrational bands of the significant Mars shock layer species (CO_2 and CO) in the mid-infrared.

A key advancement in this work was the incorporation of a bias tee into the laser control circuit which enabled MHz tuning of the continuous wave distributed feedback lasers (CW-DFB) used in this work. Bias tees are well known devices often used in radio frequency engineering. The bias tee is a diplexer which takes a DC input and an AC input and combines the signals onto the same output line. In the context of CW-DFB laser control, there is a trade-off in laser tuning range (termed 'scan depth') vs modulation frequency as shown in Fig. 1.8 (right). It is often desirable to maximize the scan depth, as this allows more spectral

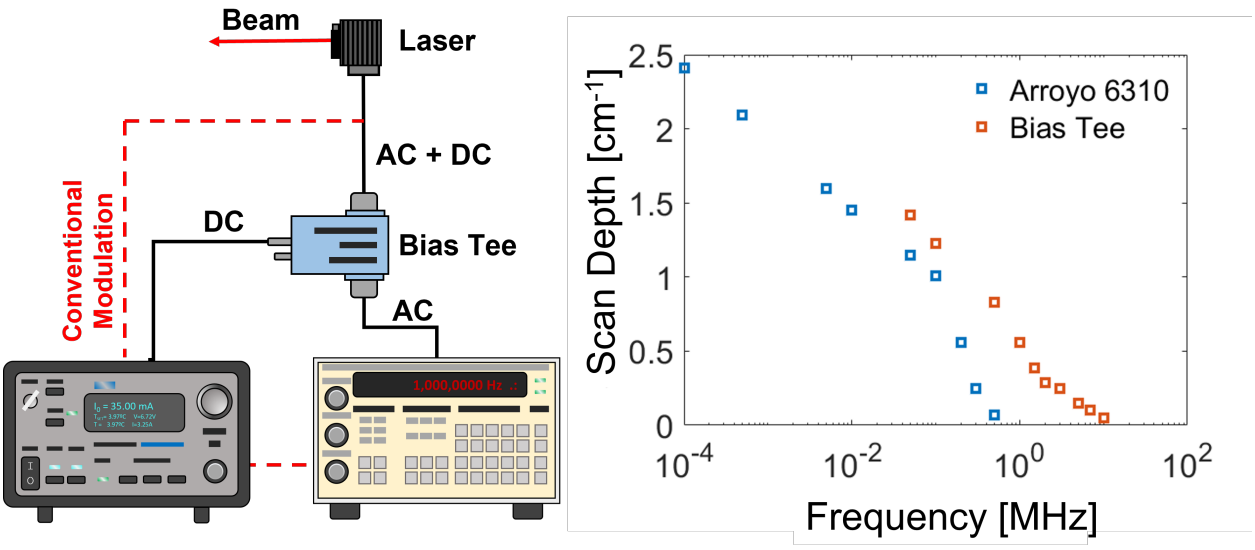

Figure 1.8: Laser control circuit diagram showing the conventional modulation circuit (red dashed lines) and the modulation circuit through a bias tee (black solid lines) (left). Typical scan depth vs scan frequency for a CW-DFB with and without the bias tee.

information to be collected per scan. Historically, scanned direct absorption measurements have been limited from the 10s to 100s of kHz due to the bandwidth limitations of the laser controller (in Fig. 1.8 labeled Arroyo 6310). This limit can be overcome with the control circuit shown in Fig. 1.8 (left) which applies the high frequency AC modulation directly to the laser enabling quantitative spectral lineshape measurements to resolve thermochemical phenomena occurring at μs timescales. This was a key advancement that benefited multiple studies in the following chapters, and additionally separate studies of rotating detonation engines [63, 62] and CO dissociation near 10,000 K [60]. Additionally this control circuit allowed further studies to optimize sensor capability with custom waveforms, and achieved a scan depth on the order of 1 cm^{-1} at a scan frequency of 1 MHz (see Nair et al. [64]).

Previous LAS work conducted by MacDonald et al. [55] measured T_{tr} and number density of CO and CO_2 in the EAST facility at conditions relevant to Mars entry. Previous work to determine temperatures of rotation and vibration in the flow field have relied on calibrated emission measurements of the optically thin C_2 emission near 385 nm [14] and the CN violet band [52, 51]. Our method is an extension of the LAS work of MacDonald et al. [55] to

include temperatures of rotation and vibration, directly observing the primary radiators of interest in the Mars entry environment (CO_2 and CO). This method is calibration free and shown to be sensitive. The sensitivity of the LAS temperature measurement is primarily affected by the lower state energy difference. For sensitive rotational temperature measurements, probing states of significantly different lower state rotational quantum number (J") is desirable as this ensures a large lower state rotational energy difference. Similarly, for sensitive vibrational temperature measurements, probing states of significantly different lower state vibrational quantum number (v") is desirable as this ensures a large lower state vibrational energy difference. Measuring many levels of each will also confirm or contradict Boltzmann rovibrational behavior during a test.

Although LAS theory is well-detailed in literature [31] and has been utilized to probe rovibrational non-equilibrium of NO and CO in other studies [24, 9], key governing equations are described here for context and nomenclature definition. The Beer-Lambert law, given in Eq. 1.10, relates the spectral absorbance α at frequency ν to thermophysical gas properties via incident and transmitted light intensities, I_0 and I_t, respectively.

$$\alpha(\nu) = -\ln\left(\frac{I_t}{I_0}\right)_\nu = S_j(T_{\text{rot}}, T_{\text{vib}}) n_A L \phi_j(\nu, T_{\text{tr}}, P, X_A) \tag{1.10}$$

Here, n_A [molec/cm^3] is the number density of absorbing molecule A, L [cm] is the pathlength, S_j [cm^{-1}/(molec cm^{-2})] is the linestrength of rovibrational transition j at rotational temperature T_{rot} [K] and vibrational temperature T_{vib} [K], and ϕ_j [cm] is the lineshape function.

In this work, scanned-wavelength direct absorption spectroscopy is utilized to resolve ϕ_j, which is modeled using the Voigt lineshape profile. The Voigt lineshape is a convolution of Lorentzian and Gaussian profiles, capturing the effects of collisional and Doppler broadening,

respectively. The value of ϕ_j at the transition linecenter $\nu_{j,0}$ is expressed in Eq. 1.11, where a is the spectral damping parameter and $\Delta\nu_D$ [cm^{-1}] and $\Delta\nu_C$ [cm^{-1}] are the Doppler and collisional linewidth contributions, respectively.

$$\phi_j(\nu_{j,0}) = \frac{2}{\Delta\nu_D}\sqrt{\frac{\ln 2}{\pi}}\exp(a^2)[1-\mathrm{erf}(a)] \tag{1.11}$$

$$a = \frac{\sqrt{\ln 2}\Delta\nu_C}{\Delta\nu_D} \tag{1.12}$$

The Doppler broadening (Eq. 1.13) is used to infer the translational temperature T_{tr} [K], where M [g/mol] is the molecular weight of the absorbing molecule and ν_0 [cm^{-1}] is the linecenter of the transition.

$$\Delta\nu_D = \nu_0(7.1623\times10^{-7})\sqrt{\frac{T_{\mathrm{tr}}}{M}} \tag{1.13}$$

Collisional linewidth scales with broadening coefficient γ_{A-B} [cm^{-1}/atm], and partial pressure of collision partner P_B, as shown in Eq. 1.14.

$$\Delta\nu_C = \sum_B P_B 2\gamma_{A-B} \tag{1.14}$$

The broadening coefficient is a function of the reduced mass of the collision partners, temperature, and collision cross-section (which is also known to be a weak function of temperature). The calculation of broadening coefficient at elevated temperatures $\gamma_{A-B}(T_{tr})$, is typically modeled via a power law fit to experimental data, as shown in Eq. 1.15, where T_0 [K] is a reference temperature and n is the temperature exponent.

$$\gamma_{A-B}(T_{\mathrm{tr}}) = \gamma_{A-B}(T_0)\left(\frac{T_0}{T_{\mathrm{Tr}}}\right)^n \tag{1.15}$$

T_{tr} can be determined accurately if the Doppler to collision width ratio ($\Delta\nu_D/\Delta\nu_C$) is >> 1, making the measurement insensitive to uncertainties in collisional broadening model, provided other broadening mechanisms (Stark, collisional narrowing [93], etc.) are negligible. If the Doppler signal is not the dominant signal in the lineshape, accurate models of the other broadening mechanisms are needed to measure T_{tr}.

To infer mode specific temperatures of rotation and vibration, the linestrength information must be accessed through the measured absorbance areas. Integration of the Beer-Lambert law (Eq. 1.10) over frequency yields Eq. 1.16 and shows the absorbance area of transition j, $\mathcal{A}_j$ [cm^{-1}], is a function of the linestrength, number density, and pathlength.

$$\mathcal{A}_j = S_j(T_{\mathrm{rot}}, T_{\mathrm{vib}}) n_A L \tag{1.16}$$

The ratio of two absorbance areas is solely a function of the linestrengths as shown by Eq. 1.17 and a general expression for the linestrength is given in Eq. 1.18.

$$R = \frac{\mathcal{A}_1}{\mathcal{A}_2} = \frac{S_1(T_{\mathrm{rot}}, T_{\mathrm{vib}})}{S_2(T_{\mathrm{rot}}, T_{\mathrm{vib}})} \tag{1.17}$$

$$S_j = \left(\frac{N_1}{N} B_{12} - \frac{N_2}{N} B_{21} \right) \frac{h\nu}{c} \tag{1.18}$$

B_{12} and B_{21} [$\mathrm{cm}^3/(\mathrm{erg}\cdot\mathrm{s}^2)$] are the Einstein coefficients of absorption and stimulated emission, which are calculated from the Einstein A coefficient, A_{21} [s^{-1}], listed in the HITEMP database [75]. h is Planck's constant, ν is the wavenumber of the transition, c is the speed of light, N_1/N and N_2/N are the population fractions of the lower and upper energy states, respectively. Equation 1.19 can be derived from Eq. 1.18 assuming separable populations of

rotation and vibration and Boltzmann population distributions.

$$S_j = \frac{A_{21} g_2}{8\pi\nu^2 c Q_{\text{rot}}(T_{\text{rot}}) Q_{\text{vib}}(T_{\text{vib}})} \left[\exp\left(\frac{-c_2 E_{\text{rot},1}}{T_{\text{rot}}}\right) \exp\left(\frac{-c_2 E_{\text{vib},1}}{T_{\text{vib}}}\right) - \exp\left(\frac{-c_2 E_{\text{rot},2}}{T_{\text{rot}}}\right) \exp\left(\frac{-c_2 E_{\text{vib},2}}{T_{\text{vib}}}\right) \right] \quad (1.19)$$

g_2 is the upper level degeneracy of the transition, c_2 is the second radiation constant (1.439 cm·K), $E_{\text{rot},1}$ and $E_{\text{vib},1}$ are the rotational and vibrational energies of the lower state [cm^{-1}], $E_{\text{rot},2}$ and $E_{\text{vib},2}$ are the rotational and vibrational energies of the upper state [cm^{-1}], and Q_{rot} and Q_{vib} are the partition functions of rotation and vibration. To evaluate this equation, the rotational and vibrational energies must be determined. Once the energy levels are determined, the partition function can be calculated via a direct sum.

The measurement sensitivity to rotational and vibrational temperatures is primarily determined from the lower state energies and the magnitude of the absorbance signals of the transitions probed. It is advantageous to probe states sufficiently separated in rotational quantum number for a sensitive rotational temperature measurement, and similarly it is advantageous to probe states sufficiently separated in vibrational quantum number for a sensitive vibrational temperature measurement. Lastly, an alternative way to determine the vibrational temperature is from the magnitude of the absorbance area signals via Eq. 1.16 provided the other variables are known or modeled accurately.

In summary, our technique has extended state of the art LAS techniques to MHz rates and examined thermodynamic non-equilibrium in shock heated CO - Ar and CO_2 - Ar gas mixtures. Additionally, LAS was deployed in parallel with optical emission spectroscopy on a reacting simulated Mars atmosphere at the EAST facility as part of this research. This diagnostic is valuable for understanding the Mars entry shock layer, and also has potential applications to flow characterization of aerothermal ground test facilities (especially those that run CO_2 and CO). The absorption technique is built on the fundamental Doppler effect

which encodes translational temperature into the lineshape of the spectral feature and the Einstein theory of radiation which relates the strength (area) of the spectral transitions to the energy level populations. These energy level populations can be interpreted through a Boltzmann assumption to yield non-equilibrium temperatures of rotation and vibration. The following chapters describe the implementation of the multi-temperature sensing technique in shock heated carbon monoxide (Ch. 2) and carbon dioxide gas mixtures (Ch. 3). Chapter 4 describes the deployment of a similar sensor (built out of the previous work with CO and CO_2 described in Ch. 2 - 3) on the EAST facility at NASA Ames. This work developed and demonstrated mid-IR LAS multi-temperature sensing techniques on representative Mars entry shock layers to improve the vibrational relaxation and chemical rate models employed by NASA for simulation of this extreme environment.

Chapter 2

Non-Equilibrium Carbon Monoxide Spectroscopy

2.1 Motivation

To accurately predict radiative heating rates experienced by the TPS of a Mars entry vehicle, the thermal and chemical kinetics across the near-surface bow shock layer in the Martian atmosphere must be well-understood. Previous work conducted by Cruden et al. [14], MacDonald et al. [55], and Johnston et al. [38] have focused on characterizing this environment using data from the Electric Arc Shock Tube at NASA Ames with multiple spectroscopic techniques (emission and absorption) along with modeling this radiation environment using state-of-the-art CFD and radiative codes, such as DPLR [103], HARA/LAURA [40], and NEQAIR [100]. There are multiple kinetic mechanisms available to model the Mars shock layer, and a simple chemical mechanism for the dissociation of CO_2 [66] is presented below.

$$CO_2 + M \rightarrow CO + O + M \tag{2.1}$$

$$O_2 + CO \rightarrow O + CO_2 \tag{2.2}$$

$$2O + M \rightarrow O_2 + M \tag{2.3}$$

CO_2 dissociation is the first reaction to occur behind the shock wave and is the rate limiting reaction in this environment. Reaction 2.1 creates an abundance of atomic oxygen, which is a very efficient collision partner, and drives many of the other reactions mentioned in the typical kinetic mechanisms of Mars entry (Cruden et al. [14] and Johnston et al. [37]). Reaction 2.1 also creates large amounts of CO in the shock layer. At fast entry velocities (> 7 km/s) CO radiation in the vacuum ultraviolet (specifically the 4th positive system) dominates the overall radiation in the shock layer and must be modeled accurately to predict heat transfer rates [7]. Non-equilibrium temperatures can be used to simulate this emission intensity, and understanding how these temperatures evolve is a key parameter in the simulation of this environment.

In this study, an optical diagnostic strategy has been developed and demonstrated to simultaneously quantify multiple temperatures (vibration, rotation, and translation) of carbon monoxide (CO), with particular relevance to non-equilibrium radiation during Mars entry. Mode-specific temperatures (rotational, vibrational, and translational) determine the energy state population distributions and associated wavelength-specific radiation intensity of CO bands. While CO radiation is strongest in the ultraviolet and vacuum ultraviolet during Mars entry, the infrared domain can be probed to determine the temperature and state population distributions that, in part, underlie the spectral intensity of the rovibronic system. Additionally, the mid-wave infrared spectrum of CO should be considered for modeling the

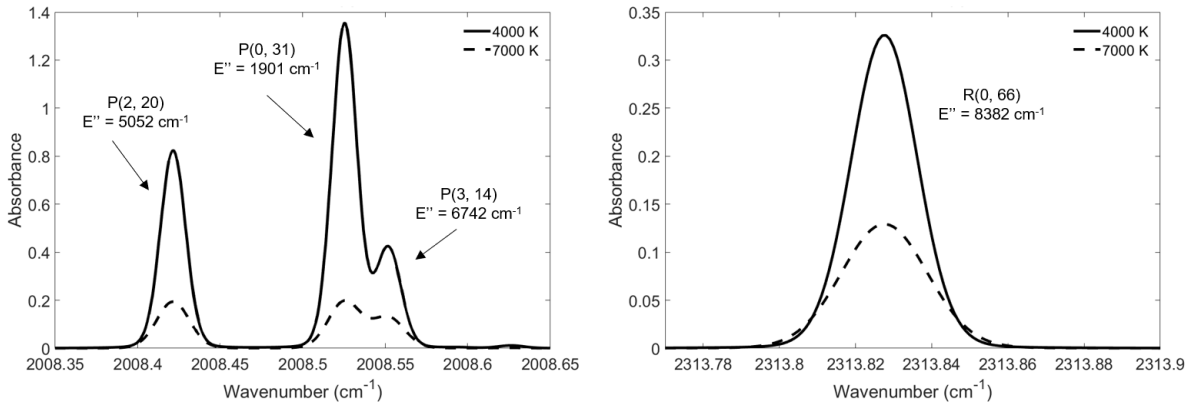

Figure 2.1: Simulated CO spectra using HITEMP database [75]. Absorbance is simulated at $X_{\mathrm{CO}} = 1.0$, $P = 0.05$ atm, $L = 10.32$ cm, and two temperatures ($T = 4000$ K and 7000 K)

back shell radiation. Multi-temperature CO measurements can also be used to reduce the uncertainty in the models of the chemistry and state population kinetics of rovibrational energy of CO during non-equilibrium. In this work, the High Enthalpy Shock Tube (HEST) facility at UCLA is used to shock-heat gas mixtures comprising CO yielding variable high-temperature, non-equilibrium conditions. Here we advance upon prior work probing translational temperature [55] by demonstrating multi-temperature sensing capability. We employ a scanned-wavelength absorption spectroscopy technique that exploits the rapid tunability of emerging semiconductor lasers in the mid-wave infrared to spectrally resolve several rovibrational lines in the CO fundamental vibrational bands. Line intensities and widths are used to infer vibrational, rotational, and translational temperature simultaneously. Fast measurement rates (on the order of MHz) are desired when probing shock layer thermochemical non-equilibrium. Rapid laser scanning via diplexed RF modulation [62] enables sufficient temporal resolution for the measurements in this study. The following sections detail the theory and methods behind the novel measurement technique, as well as time-resolved data demonstrating the sensing method in shock-induced non-equilibrium.

2.2 Methods and Spectroscopic Model

2.2.1 Line Selection

Laser absorption spectroscopy (LAS) was utilized to infer energy mode-specific temperatures from spectrally-resolved light attenuation in the mid-wave infrared. In this study, scanned-wavelength direct absorption spectroscopy is utilized to resolve ϕ_j, which is modeled using the Voigt lineshape profile as described in Sec. 1.5. The Voigt lineshape is a convolution of Lorentzian and Gaussian profiles, which describe collisional and Doppler broadening effects, respectively. For this study, collisional broadening and temperature coefficients for CO-CO and CO-Ar were taken from Sinclair et al. [80], Roscasco et al. [73], and Bendana et al. [4]. Most experiments performed in this study had collisional FWHM nearly one order of magnitude less than the Doppler FWHM making this measurement technique relatively insensitive to the collisional broadening parameters used.

2.2.2 Multi-temperature linestrength

In this work, the R(0,66), P(2,20), P(0,31), and P(3,14) lines of the CO fundamental infrared vibrational bands were measured; here the line identifiers B(v'',J'') indicate the branch (R or P) and lower state vibrational and rotational quantum numbers. The lines were chosen because of spectral isolation enabling resolution of individual integrated areas and linewidths of each transition and due to sufficient absorbance over a wide temperature and pressure range of interest (2000–7000 K, 0.01–0.1 atm). In order to determine vibrational temperature, multiple vibrational levels must be probed. Similarly, in order to determine rotational temperature, multiple rotational levels must be measured. The separation of lower state energies further factored into line selection. The present sensing strategy probes 3 lower state vibrational levels ($v'' = 0$, 2, 3) and 4 lower state rotational levels ($J'' = 14$, 20, 31, 66) of CO.

The HITEMP database [75] was used to simulate the selected lines in equilibrium, shown in Fig. 2.1. The vibrational and rotational quantum numbers along with the lower state energy of each transition are indicated in the figure. A large range of lower state energies is preferred, since this increases the sensitivity of the temperature measurement according to the Boltzmann distribution.

The translational temperature of the gas can be determined from the width of the lines, while the rotational and vibrational temperatures can be inferred from the relative intensities of the lines. Integration of Eq. 1.10 over the frequency domain yields an integrated absorbance area $\mathcal{A}_j$ of a spectral line that is linearly proportional to the linestrength. This is shown in Eq. 1.16 below. The ratio of integrated absorbance areas of various lines is thus independent of pressure, mole fraction, and pathlength; this area ratio thus reduces to a ratio of linestrengths, as shown in Eq 1.17.

To evaluate this equation, the energy levels were computed with the Dunham expansions taken from the NIST database [53]. The rotational and vibrational partition functions were computed via direct summation over the energy levels and were shown to adequately reproduce the equilibrium partition function provided from HITRAN [29] up to 9000 K.

Fig. 2.2 shows the calculated linestrengths as a function of T_{rot} and T_{vib} for the lines measured in this study. It can be clearly seen that the lines in the ground vibrational level (P(0, 31) and R(0, 66)) are stronger at lower T_{vib} than the second and third vibrational level lines (P(2,20) and P(3,14)). Additionally, the higher rotational energy lines are clearly stronger at higher T_{rot}.

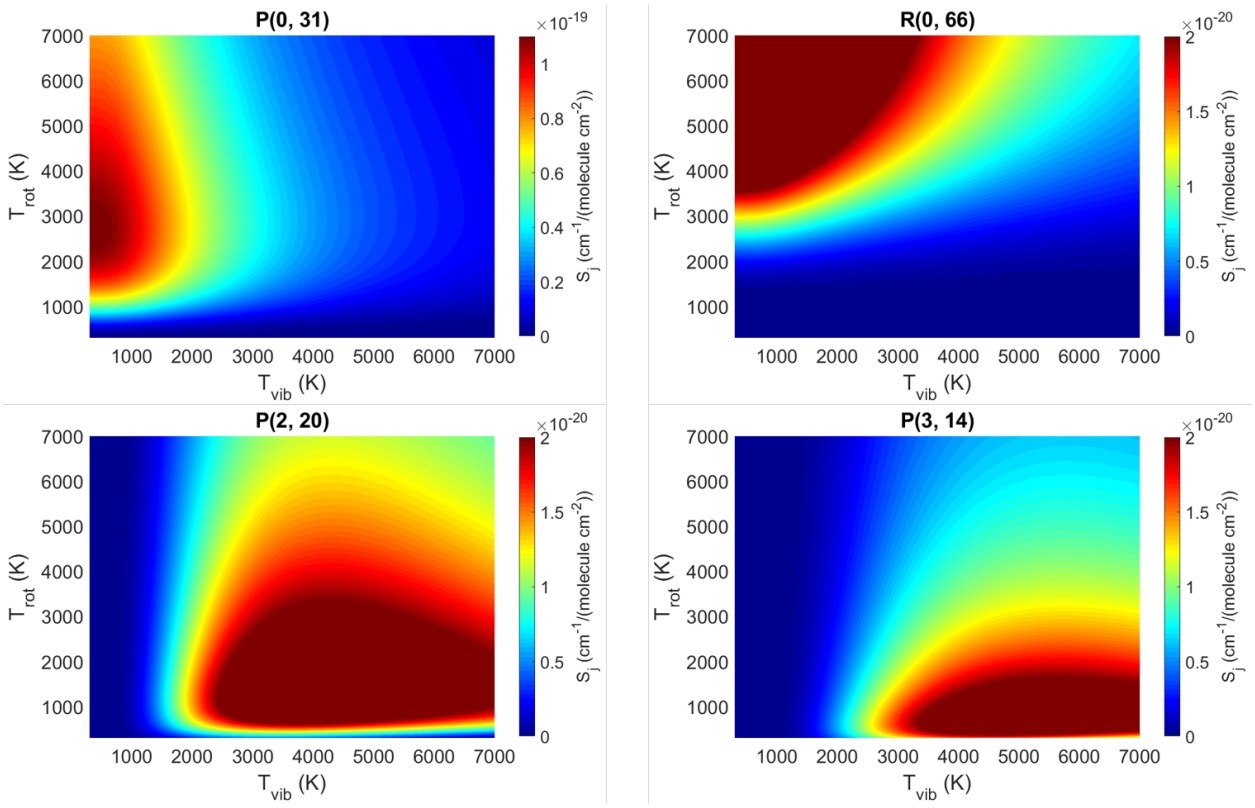

Figure 2.2: Simulated linestrengths as a function of T_{rot} and T_{vib} for the spectral features measured in this study.

2.2.3 Vibrational relaxation model

When a shock wave interacts with a quiescent gas, a rapid energy transfer occurs from the shock wave into the gas mixture [94]. The energy from the shock wave will be absorbed by the gas in various energy modes depending on the constituent molecules in the gas. In a shock heated gas mixture made up of monatomics, such as He, Ar, Ne, etc., the energy is stored in the translational and electronic energy modes of the gas. In a shock heated mixture made up of diatomic or polyatomic molecules, such as N_2, O_2, CO, CO_2, etc., the energy can be stored in translation and electronic modes, but additionally modes of rotation and vibration become available. As the shock passes through the gas, the translational energy mode is the first to excite, and if there are rotational and vibrational energy modes available, energy will be transferred from translation to rotation and vibration as the gas seeks to minimize

its free energy. In cases where vibrational energy transfers are the slowest (often the case for diatomics like CO), the thermal kinetics are defined by vibrational relaxation. Often, these energy modes are considered independent and separable as shown in Eq. 2.4. In this approximation, separate temperatures can be used to describe the energy of each mode. In molecular gas theory, an energy mode's temperature describes a Boltzmann population distribution of gas molecules over the energy levels of that mode. Additional terms in Eq. 2.4 may be included to capture additional modes of vibration and electronic excitation, each at their own temperature. It is important to note that when the gas reaches equilibrium over its internal energy modes it is possible to describe the gas by a single temperature (i.e. at equilibrium, $T_{\text{tr}} = T_{\text{rot}} = T_{\text{vib}}$).

$$E_{\text{gas}} = E_{\text{tr}}(T_{\text{tr}}) + E_{\text{rot}}(T_{\text{rot}}) + E_{\text{vib}}(T_{\text{vib}}) + ... \tag{2.4}$$

The partition function of an ensemble of gas molecules defines the total number of available states that the gas can occupy. If the energy modes are considered separable, the partition function for each mode can be written and the total partition function may be determined via products of each mode's partition function as shown below in Eq. 2.5. Additionally, the partition function and constituent partition functions can be related to useful macroscopic properties of the gas such as energy and entropy. Eq. 2.8 below shows the relation between internal energy and partition function. The energy stored in vibration can be calculated by using Eq. 2.8 with the vibrational partition function (Q_{vib}) and vibrational temperature (T_{vib}). The result for E_{vib} shown in Eq. 2.9 assumes a simple harmonic oscillator for the energy level spacing.

$$Q = Q_{\text{tr}} Q_{\text{rot}} Q_{\text{vib}} Q_{\text{el}} \tag{2.5}$$

$$Q_{\text{rot}} = \sum_{0}^{J_{\max}} \left[g_{\text{rot}} \exp\left(\frac{-hcE_{\text{rot},j}}{kT_{\text{rot}}} \right) \right] \tag{2.6}$$

$$Q_{\text{vib}} = \sum_{0}^{v_{\max}} \left[g_{\text{vib}} \exp\left(\frac{-hcE_{\text{vib},v}}{kT_{\text{vib}}} \right) \right] \tag{2.7}$$

$$E_{\text{gas}} = NkT^2 \left(\frac{\partial \ln Q}{\partial T} \right)_V \tag{2.8}$$

$$E_{\text{vib}} = \frac{Nk\Theta_{vib}}{\exp\left(\frac{\Theta_{\text{vib}}}{T_{\text{vib}}} \right) - 1} \tag{2.9}$$

In a high-temperature gas, information propagates via radiation and collisions between atoms, electrons and molecules. The dominant relaxation process of the translation and vibration energy modes is driven by collisional processes and often referred to as a "VT" transfer. This is described in detail by Schwartz, Slawsky and Herzfeld theory (SSH theory) [78]. It is important to note that there are different timescales of excitation for the modes of translation, rotation, and vibration. A model for the vibrational relaxation time constant (τ_{VT}) has been made by Millikan and White [59] and an analytical expression is available based on the reduced mass of the collision partners as well as temperature and pressure. Empirical fits to data for τ_{VT} are available in [58] and often provide a more accurate model when studying a specific set of collision partners. The Bethe-Teller equation (Eq. 3.3) is used to model the VT process, which asserts that the rate of vibrational energy change is proportional to the energy difference between the equilibrium vibrational energy at the current translational temperature ($E_{\text{vib}}(T_{\text{tr}})$) and its current vibrational energy ($E_{\text{vib}}(T_{\text{vib}})$). The

Millikan relaxation time constants and the Bethe-Teller equation along with the assmuptions described in the previous section constitute the model used to describe the time evolution of translational and vibrational temperature in this study.

$$\frac{\mathrm{d}E_{\mathrm{vib}}}{\mathrm{d}t} = \frac{E_{\mathrm{vib}}(T_{\mathrm{tr}}) - E_{\mathrm{vib}}(T_{\mathrm{vib}})}{\tau_{VT}} \tag{2.10}$$

2.3 Optical and Experimental Setup

Laser absorption spectroscopy (LAS) was utilized to measure the mode-specific temperatures (translation, rotation, vibration) of CO behind incident and reflected shock waves. The High Enthalpy Shock Tube facility at UCLA was used to generate incident shock waves (1–3.3 km/s) for CO-Ar gas mixtures at various initial conditions to test the range and accuracy of the measurement strategy. Five piezoelectric time-of-arrival sensors located in the driven section of the tube were used to measure the incident shock velocity. Measurements were conducted two centimeters from the shock tube end wall through two 0.5 degree wedged

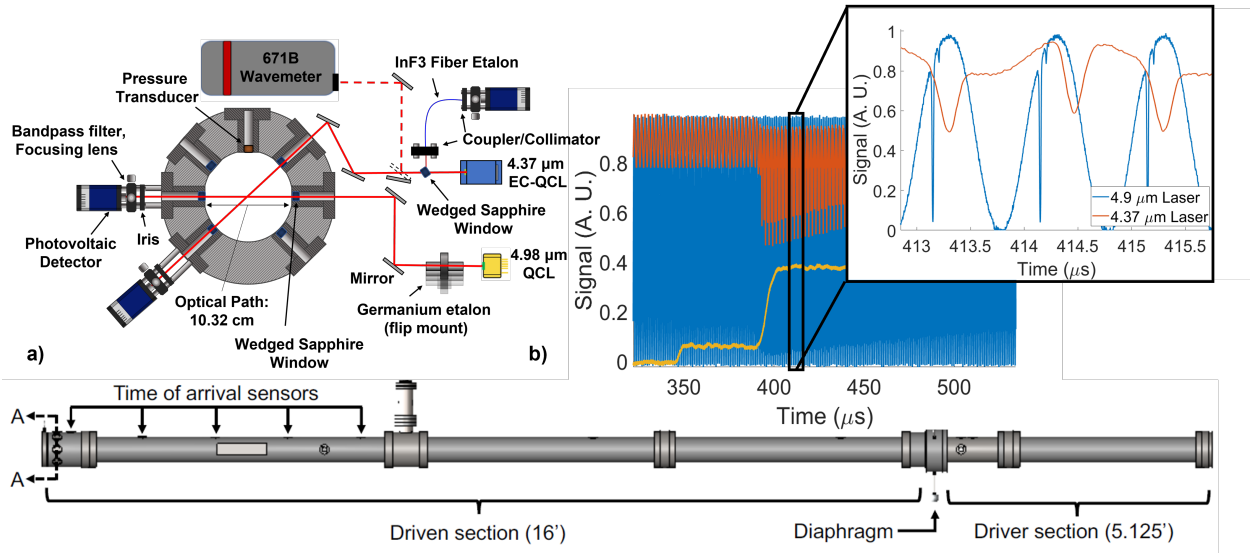

Figure 2.3: a) Optical setup on the shock tube b) Modulating intensity signals from the two lasers during a test

sapphire windows. A normal shock relation solver [10], with prescribed vibrationally frozen or equilibrium assumptions, were used with the shock velocity and enthalpy curve fits [2] of CO and Ar to calculate conditions generated during each test.

The optical setup is shown in Fig. 2.3. The four spectral transitions probed in this study (defined in Section 2.2.2) were measured with two mid-wave infrared tunable semi-conductor lasers. An external cavity, continuous-wave, quantum cascade laser (EC-QCL) (Daylight Solutions), tunable over a range of wavelengths near 4.37 µm, was used to probe the R(0,66) transition. A small fraction of the beam intensity was reflected using a sapphire window and coupled into a 1 meter indium-fluoride (InF_3) optical fiber etalon. The etalon signal was recorded on a 50 MHz PVMI-8 detector. A flip mirror was also utilized to intermittently direct the light into a wavemeter before each test to ensure that the EC-QCL was at the proper wavelength and did not drift between tests. The EC-QCL was modulated with a 500 kHz sine wave using the bias tee built into the laser. This resolved the R(0,66) transition at a rate of 1 MHz when both the up and the down scans are processed. After being pitched through the test section, the 4.37 µm light is directed through multiple neutral density filters and focused on a high bandwidth (∼200 MHz) AC coupled PVI-5-4TE detector. To measure the DC offset of the laser intensity on this detector, a beam chopper was used during the tests. A 4.98 µm distributed feedback quantum cascade laser (DFB-QCL) was used to probe the P(2,20), P(0,31) and P(3,14) transitions. This laser is typically tuned with a current driver with a modulation bandwidth limit of 200 kHz. To bypass this limit, a bias tee circuit was built to diplex the mean current signal generated from the laser driver with a RF modulation signal from a function generator. A similar technique was developed and used by Nair et al. [63] to achieve MHz gas property measurements in a rotating detonation engine. The P branch lines are spectrally proximal enough to be resolved on the same laser current scan at a rate of 1 MHz with the bias tee modulation circuit. The 4.98 µm light passes through a separate optical port on the shock tube in the same transverse axial plane. A calcium-fluoride lens is used to focus the 4.98 µm light through a narrow bandpass spectral

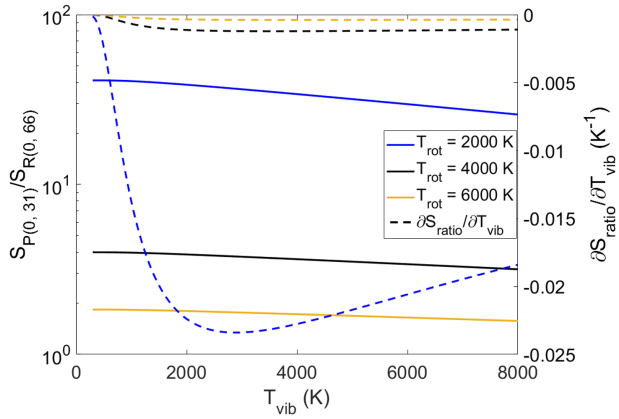

Figure 2.4: Linestrength ratio as a function of T_{vib} plotted for multiple T_{rot}. The T_{vib} effect on linestrength ratio is most prominent at low T_{rot} and higher T_{vib} as shown with the derivative curves.

filter and onto a 195 MHz PVMI-8-4TE detector. The data acquisition system used on these tests was a Tektronix mixed signal oscilloscope with a bandwidth limit of 200 MHz that recorded the pressure trace, and three detector signals (two transmission signals from the test section and a real-time etalon signal for the EC-QCL). Fig. 2.3 (b) shows the modulation detector intensity signals of the 4.37 μm and 4.9 μm laser during a test after the passage of the reflected shock.

2.4 Spectroscopic Data Processing

In this section, we describe the spectroscopic data processing methods used to quantitatively infer vibrational, rotational, and translational temperatures from the transmitted intensity signals that scan over the target CO transitions. The three strongest lines dominate the data fitting procedure, but the weak P(3,14) transition contributes at high temperatures and blends with the stronger P(0,31) transition, complicating the spectral fit (see Fig. 2.1 (a)). We account for this spectral overlap with an iterative convergence procedure, depicted in Fig. 2.5. In this procedure, the absorbance contributed by the CO P(3,14) transition

is modeled utilizing a Voigt lineshape and subtracted from the measured absorbance prior to a three-line spectral fit of the P(0,31), P(2,20), and R(0,66) lines. In the first step (iteration k), estimates for three temperatures are used in combination with the calculated collisional widths $\Delta\nu_C$ using the calculated pressure from the shock solver [10] to simulate the absorbance from the P(3,14) line. The simulated P(3,14) line is then subtracted from the measured absorbance spectra. Next, a three-line Voigt fit is applied to the remaining P(0,31), P(2,20), and R(0,66) spectra to determine T_{tr} (which is based on the Doppler linewidth $\Delta\nu_D$ of each line). In addition to T_{tr}, the absorbance areas and line positions are treated as free parameters during the fit. In the final steps, T_{vib} is inferred from the ratio of fitted absorbance areas of the P(0,31) and P(2,20) lines using two-line thermometry as described by Eq. 1.17 at the estimated rotational temperature. Similarly, T_{rot} is inferred from the ratio of fitted absorbance areas of the P(0,31) and R(0,66) lines. These inferred values of T_{tr}, T_{vib}, and T_{rot} are new temperature estimates for the next iteration (iteration k + 1) in the loop described in Fig. 2.5(a). The iterations continue until changes in new estimates are within 1 K of the temperatures at the start of the iteration. The linestrength model described in Sec. 2.2.2, implies T_{vib} will affect the linestrengh ratio of two lines from the same vibrational band. This is shown in Fig. 2.4 and the affect is clearly seen at high T_{vib} and low T_{rot}. This stems from the inclusion of stimulated emission in the linestrength formulation.

Figure 2.5(b) shows the measured absorbance spectra from a representative laser scan (no averaging) along with the resulting spectral fits of the target CO transitions from the iteration procedure. The residual between measurement and overall spectral fit with the Voigt lineshape model is typically under 5% for each line, demonstrating the appropriateness of the iterative fitting procedure and the relatively high signal-to-noise ratio (SNR).

2.5 Results/Sensor Demonstration

Experiments were conducted to demonstrate the range, accuracy, and time resolution of the multi-temperature sensing method. Both equilibrium conditions and non-equilibrium conditions were generated in CO-Ar mixtures behind incident and reflected shocks. The first series of tests were aimed at anchoring the measurements to expected equilibrium calculations from normal shock relations. This test series also included low-temperature comparisons to the Bethe-Teller vibrational relaxation model [5] with relaxation time constants given by Millikan [58]. The second series of tests aimed to demonstrate the sensor at non-equilibrium conditions more relevant to the entry environment which involved higher incident shock velocities, higher temperatures, lower pressures, and higher CO concentrations. These tests were focused on demonstrating time resolution and transient temperatures that converge from frozen towards equilibrium conditions.

We first consider time-resolved data from a single representative experiment, shown in Fig.

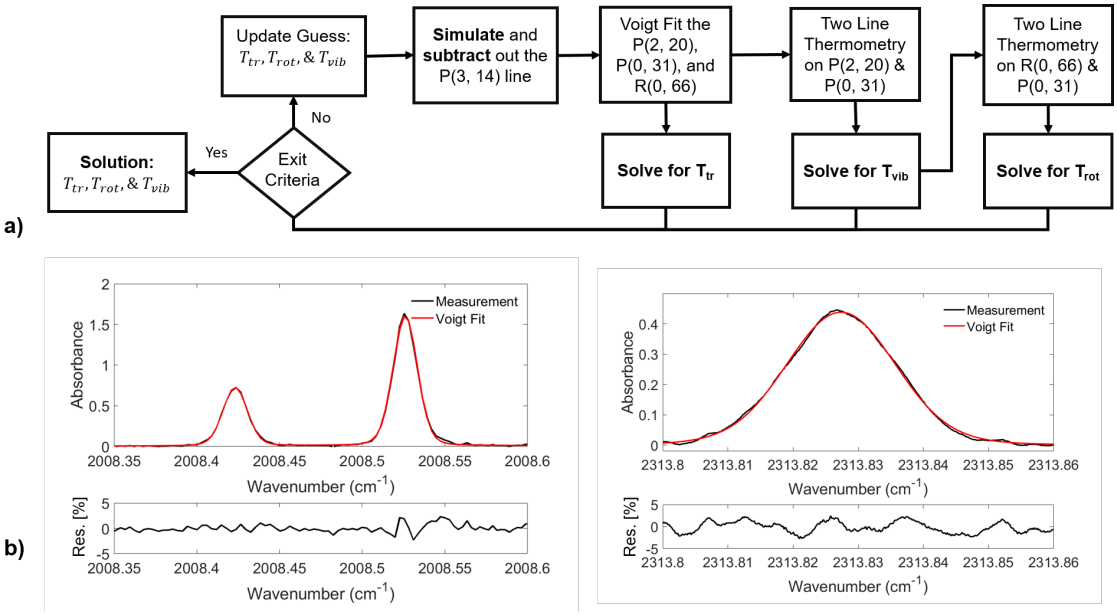

Figure 2.5: a) Block diagram describing iterative spectral fitting procedure for determination of T_{tr}, T_{rot}, and T_{vib} with b) representative three-line fits for single laser scans.

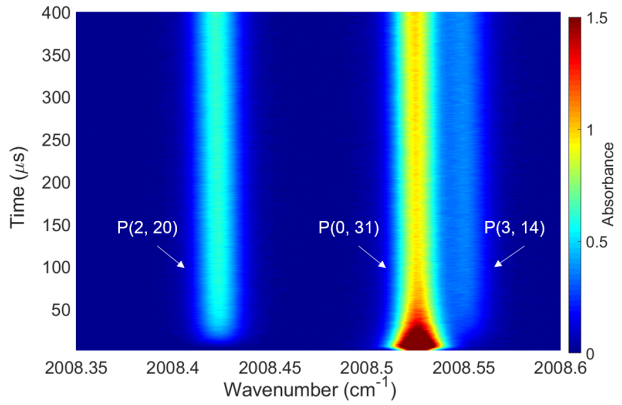

Figure 2.6: Absorbance signal versus time and wavenumber. Rapid depopulation of the P(0, 31) line is seen in the first 50 microseconds.

2.6, which presents absorbance versus wavenumber (near 4.98 µm) and time behind a reflected shock. From the spectroscopic model previously discussed in Sec. 2.2.2, Fig. 2.6 confirms the proper trends are captured in the data. A rapid population of the ground state P(0,31) transition occurs behind the shock wave and is seen to peak near the beginning of the test time. The second and third vibrational levels then begin to populate as the ground state is de-populating. This is characteristic of a vibrational temperature increase during this relaxation to thermal equilibrium. A clear equilibrium is reached in the spectra by observing the widths and absorbance intensities at later test times, characteristic of steady temperature, pressure, and mole fraction conditions.

An incident shock test is highlighted in Fig. 2.7, giving analogous trends but here showing the retrieved absorbance areas and Doppler widths from the fitting procedure described in Section 2.4. From the transient integrated line areas, we see the P(0,31) and R(0,66) populate rapidly and then immediately begin depopulating as the P(2,20) population increases. The retrieved Doppler width, which scales as $\sqrt{T_{\mathrm{tr}}}$, is plotted versus time in Fig 2.7(b), and is shown to decrease during the transient portion of the test. Equilibrium predictions of absorbance area and Doppler width are plotted as well at the conditions estimated from the shock relation solver [10]. The equilibrium linestrength is taken from the HITEMP database [75] and used with Eq. 1.16 to generate the absorbance area prediction. For all

parameters, the convergence towards equilibrium values is clear, with a representative decay. This is consistent with the Bethe-Teller prediction that the rate of vibrational energy change is proportional to the energy difference between the equilibrium vibrational energy and its current vibrational energy.

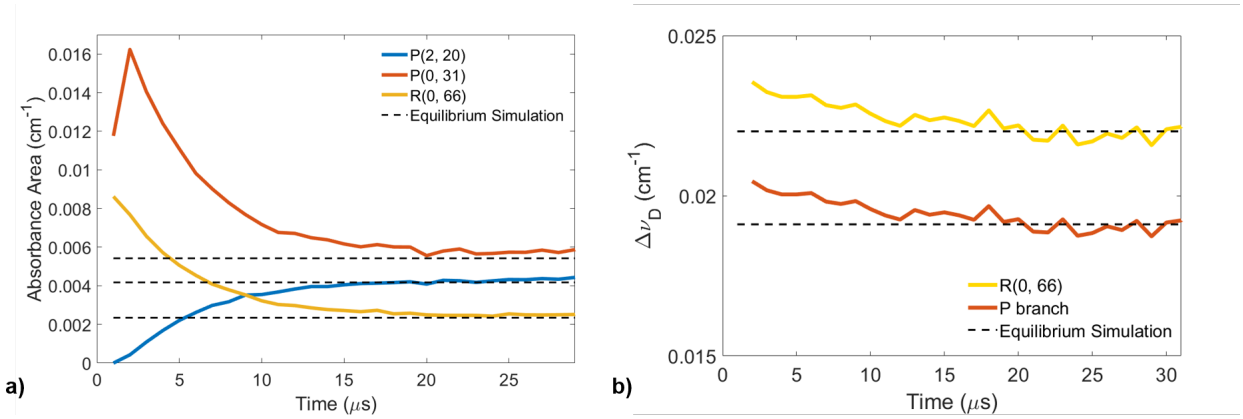

Figure 2.7: a) Absorbance area versus time for three lines shown with equilibrium predictions. b) Measured Doppler width versus time for the R(0,66) and P branch transitions.

At the lower temperatures and relatively high fill pressures (>10 torr), the time-resolved temperatures behind reflected shocks could be well-compared to vibrational relaxation models. One such low-temperature test is presented in Fig. 2.8, showing good agreement between measured vibrational and rotational temperature time-histories with predicted vibrational relaxation time from Millikan [58]. The lower temperature, 5% CO concentration, and higher pressure tests precluded a reliable independent measurement of T_{tr} because the width of the spectral features have a small Doppler component convoluted with a larger component from Lorentizian broadening due to the elevated pressures. However, at such conditions, T_{rot} and T_{tr} are expected to be equivalent. The time-resolved T_{rot} on this test had a standard deviation (2σ) of 30 K. T_{vib} showed a similar standard deviation (2σ) of 21 K. This demonstrates the high precision and signal-to-noise ratio of the sensor when measuring the relaxation transients at low temperatures and high fill pressures (near 10 torr). At very low initial fill pressures (which yielded higher post-shock temperatures), there was somewhat lower confidence in the simulated vibrational relaxation time-scales due to modest leak rates in

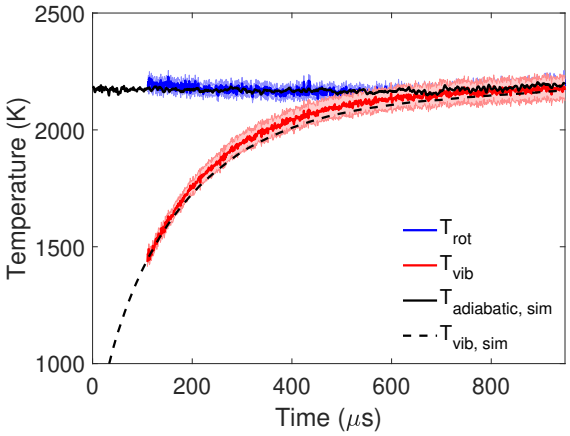

Figure 2.8: T_{rot} and T_{vib} plotted versus time. Note the strong agreement with the Millikan prediction for relaxation time. 5% CO - Ar reflected shock test case ($U_{\text{is}} = 993 \pm 5$ m/s).

the shock tube (∼100 µTorr/minute), which became more consequential when fill pressures approached ∼1 Torr.

At the higher end of the temperature range examined (>3500 K), all three temperatures could be successfully resolved as seen in Fig. 2.9. Higher CO concentrations were used in the tests above 3000 K (25% and 75%) while fill pressures were decreased to around 1 torr. While the relaxation time-scales were perhaps more difficult to control at these low initial pressures, vibrationally frozen and equilibrium conditions post-shock could still be readily calculated and compared to measurements. The higher incident shock velocities increase the Doppler broadening of each spectral line and the lower fill pressures decrease the collisional broadening of each line. These two facts aid in driving noise down on the T_{tr} measurement. While relaxation times began to deviate from the Millikan model [58], likely due in part to experimental uncertainties the equilibrium values showed good agreement. Fig. 2.10 summarizes the range of conditions measured with the sensor. To generate Fig. 2.10 a thermal equilibrium region was identified for various tests (after temperatures plateau) and mean values of T_{tr}, T_{rot}, T_{vib}, were extracted from the data. The simulated temperature (x-axis) was determined from the calculated equilibrium post-shock temperature coupled with an isentropic compression / expansion assumption that accounts for pressure change

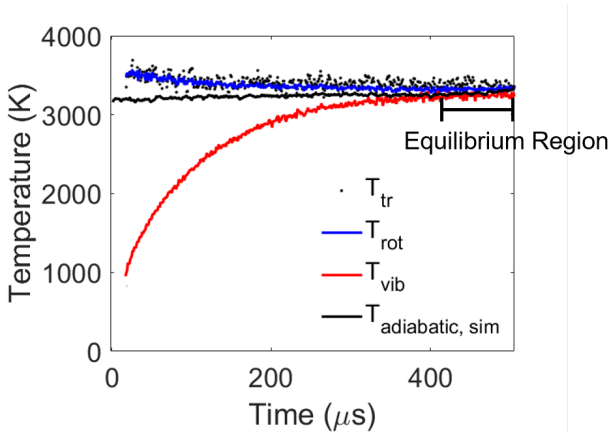

Figure 2.9: Non-equilibrium temperatures versus time. T_{rot} and T_{vib} resolved at 1 MHz. T_{tr} resolved at 500 kHz. Note the convergence of temperatures to equilibrium at the end of the test time. 25% CO-Ar reflected shock test case ($U_{\text{is}} = 1336 \pm 9$ m/s).

during the test time. The time-resolved post-shock pressure is measured with a high-speed pressure transducer (Kistler 601B1). The data presented in Fig. 2.10 show average standard deviations (2σ) of 56 K and 72 K for T_{rot} and T_{vib} respectively. T_{rot} and T_{vib} have an average residual of 1–2% with the simulated temperature, which highlights the average precision of the sensor over this temperature range. The T_{tr} measurements exhibited higher noise and up-down scan oscillations than the T_{rot} and T_{vib} measurement; however, this noise was somewhat mitigated in the equilibrium region. To reduce the oscillatory behavior in the T_{tr} measurement in the equilibrium region (where longer timescales were observed), a moving average filter with a window of 2 was applied to the Doppler width. This yielded an effective measurement rate of 500 kHz on T_{tr}, with an effective precision on the order of 3% (100 K). Overall, the equilibrium measurements have been compared with predictions from the shock relations solver over the temperature range of 2100–5500 K. T_{rot} and T_{vib} show average agreement on the order of 2% and T_{tr} shows typical agreement within 5%.

To highlight the time resolution capability of the multi-temperature sensor, Fig. 2.11 presents two incident shock cases where the three transient temperatures were resolved at 1 MHz. These high temperature, low pressure tests yield lower noise in translational temperature likely due to the much higher Doppler-to-collision width ratio and higher CO concentration

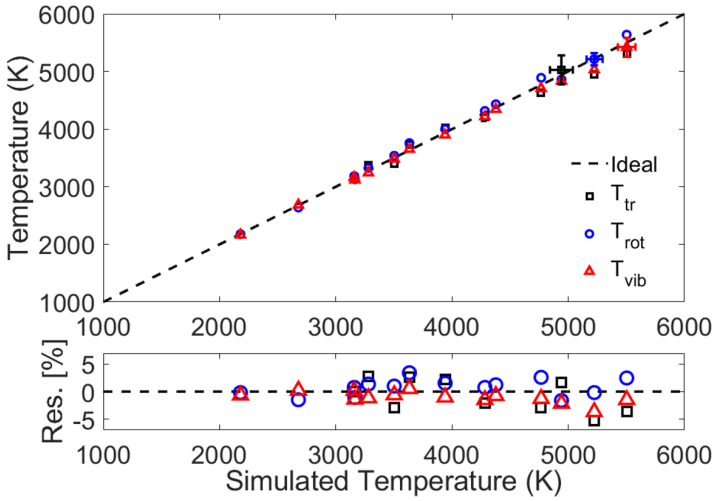

Figure 2.10: Test conditions measured by the sensor and compared to simulated conditions based off the normal shock relation solver [10]. Representative error bars are shown on 3 points.

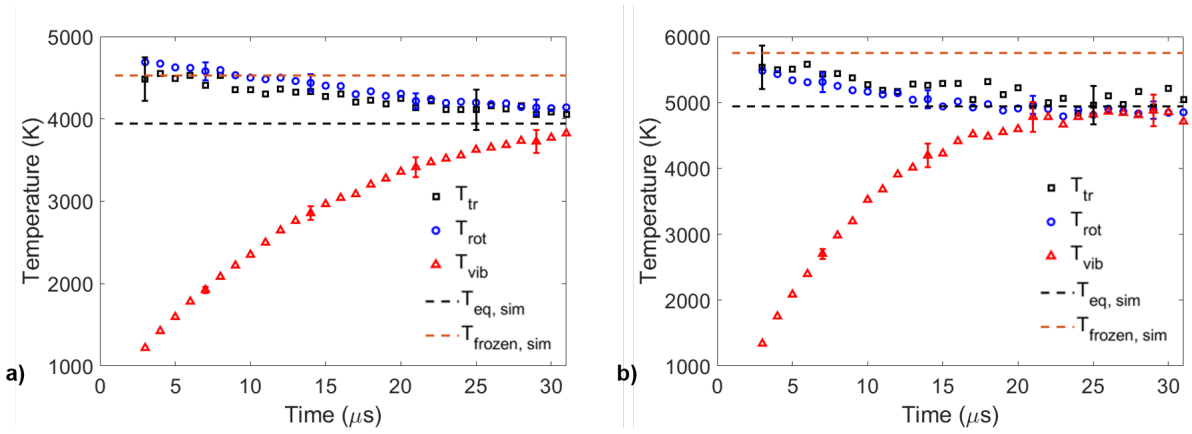

Figure 2.11: Non-equilibrium temperatures plotted with time. a) 75% CO - Ar incident shock test case ($U_{is} = 2769 \pm 28$ m/s) resolved at 1 MHz approaching $T_{eq} = 3920$ K. b) 75% CO - Ar incident shock test case ($U_{is} = 3142 \pm 35$ m/s) resolved at 1 MHz approaching $T_{eq} = 4940$ K.

(75% versus 25%). Initially the rotational and translational temperatures are measured to be nearly the same value as the vibrationally frozen gas temperature estimated from the shock relations solver. As the second vibrational level becomes populated, the vibrational temperature is measured and begins to be captured around 3 µs on each test with a value above 1000 K. It is observed on both tests that T_{tr}, T_{rot}, and T_{vib} trend towards the equilibrium temperature predicted from the shock relations. We also note that the translational and rotational temperatures are shown to agree within measurement uncertainty throughout the transient.

2.6 Conclusions

A multi-temperature gas sensor based on mid-IR laser absorption spectroscopy of carbon monoxide has been developed and shown to yield simultaneous measurements of T_{tr}, T_{rot}, and T_{vib} at temperatures ranging from 2100–5500 K. A 1-MHz measurement rate was achieved and presented in Fig. 2.11. The sensor is shown to resolve non-equilibrium transient temperatures of CO for conditions relevant to Mars entry at speeds up to 3.2 km/s, with good potential for studies at higher temperatures (T > 5500 K) and higher shock velocities. Several validation tests were performed to build confidence in the sensor performance. The low temperature tests (<3000 K) yielded very good agreement with the Millikan model [58] for relaxation times of CO-Ar mixtures. At these low temperatures and high pressure conditions, T_{tr} could not reliably be extracted due to low Doppler width relative to collision width. At higher temperatures, the observed relaxation time was faster than the Millikan prediction. Though the attribution to this observation has not yet been definitely proven, the measurements showed good agreement with the simulated beginning and end states (frozen and equilibrium), thus the deviation is highly unlikely to be sensor-related. Rigorous uncertainty analysis of the experimental results is detailed in Sec.2.7 and predict errors are on the order

of 2–3% for T_{rot}, 3–4% for T_{vib}, and 5–6% for T_{tr}.

In conclusion, this work demonstrated that three temperatures of CO (vibration, rotation, translation) could be measured simultaneously at temperatures above 3500 K and sub-atmospheric pressures via infrared laser absorption. As expected, the translational temperature measurement produced better results at higher Doppler to collision width ratios, achieved during the incident shock tests. This study has shown that rapidly tunable mid-IR lasers are capable of resolving transitions from multiple vibrational bands at MHz rates allowing multiple temperatures to be inferred using two room-temperature quantum cascade lasers. As such, the sensing strategy is well suited for transient studies of shock-induced non-equilibrium. Furthermore, refinement of the technique is expected to yield improved accuracy and increased time-resolution.

2.7 Uncertainty Analysis

This study has presented and demonstrated a method to determine non-equilibrium temperatures using laser absorption spectroscopy. In this section we detail the primary sources of uncertainty in this measurement technique using the Taylor series method for error propagation. The non-dimensional uncertainty in variable r (represented as $\frac{\delta r}{r}$ in Eq. 4.18) can be calculated from the uncertainties in the quantities used to calculate r (represented as x_i with its associated uncertainty δx_i) [6]. Equation 4.18 implicitly assumes the sources of error (x_i) are uncorrelated. By inspection of Eq. 1.17, T_{rot} and T_{vib} are shown to be functions of each other as well as the linestrength (S) and area ratio (R_{vib} or R_{rot}) of the transitions. The application of Eq. 4.18 to T_{rot} and T_{vib} yields Eqs. 4.19 and 4.24) which are solved simultaneously. The derivatives in Eq. 4.19 and Eq. 4.24 are evaluated numerically because Eq. 1.19 has no closed form solution for T_{rot} and T_{vib}. The equations are readily solved once appropriate values for the uncertainty in area ratios and linestrengths are determined.

$$\left(\frac{\delta r}{r}\right)^2 = \sum_i \left(\frac{dr}{dx_i}\frac{\delta x_i}{x_i}\frac{x_i}{r}\right)^2 \tag{2.11}$$

$$T_{\text{vib}} = f(R_{vib}, T_{\text{rot}}, S_{P(0,31)}, S_{P(2,20)}) \tag{2.12}$$

$$T_{\text{rot}} = f(R_{rot}, T_{\text{vib}}, S_{P(0,31)}, S_{R(0,66)}) \tag{2.13}$$

$$\left(\frac{\delta T_{\text{rot}}}{T_{\text{rot}}}\right)^2 = \left(\frac{dT_{\text{rot}}}{dR_{rot}}\left(\frac{\delta R_{rot}}{R_{rot}}\right)\frac{R_{rot}}{T_{\text{rot}}}\right)^2 + \left(\frac{dT_{\text{rot}}}{dT_{\text{vib}}}\left(\frac{\delta T_{\text{vib}}}{T_{\text{vib}}}\right)\frac{T_{\text{vib}}}{T_{\text{rot}}}\right)^2 + \left(\frac{dT_{\text{rot}}}{dS_{P(0,31)}}\left(\frac{\delta S_{P(0,31)}}{S_{P(0,31)}}\right)\frac{S_{P(0,31)}}{T_{\text{rot}}}\right)^2 + \left(\frac{dT_{\text{rot}}}{dS_{R(0,66)}}\left(\frac{\delta S_{R(0,66)}}{S_{R(0,66)}}\right)\frac{S_{R(0,66)}}{T_{\text{rot}}}\right)^2 \tag{2.14}$$

$$\left(\frac{\delta T_{\text{vib}}}{T_{\text{vib}}}\right)^2 = \left(\frac{dT_{\text{vib}}}{dR_{vib}}\left(\frac{\delta R_{vib}}{R_{vib}}\right)\frac{R_{vib}}{T_{\text{vib}}}\right)^2 + \left(\frac{dT_{\text{vib}}}{dT_{\text{rot}}}\left(\frac{\delta T_{\text{rot}}}{T_{\text{rot}}}\right)\frac{T_{\text{rot}}}{T_{\text{vib}}}\right)^2 + \left(\frac{dT_{\text{vib}}}{dS_{P(0,31)}}\left(\frac{\delta S_{P(0,31)}}{S_{P(0,31)}}\right)\frac{S_{P(0,31)}}{T_{\text{vib}}}\right)^2 + \left(\frac{dT_{\text{vib}}}{dS_{P(0,20)}}\left(\frac{\delta S_{P(2,20)}}{S_{P(0,20)}}\right)\frac{S_{P(2,20)}}{T_{\text{vib}}}\right)^2 \tag{2.15}$$

There are five terms in Eq. 4.19 and Eq. 4.24 needed to determine the uncertainty in rotational temperature ($\delta T_{\text{rot}}/T_{\text{rot}}$) and the uncertainty in vibrational temperature ($\delta T_{\text{vib}}/T_{\text{vib}}$). The representative value for the uncertainty in vibrational area ratio 3%. Similarly, the representative value for uncertainty in rotational area ratio is 4%. The uncertainty in linestrength is taken directly from the HITEMP database [75] (5%, 2%, and 2% for the P(2, 20), P(0, 31), and R(0, 66) lines respectively). To calculate the uncertainty in the area ratio, the error in each measured absorbance area was calculated considering three sources: 1) the value of the free spectral range (FSR) of the etalon, 2) the confidence in the peak locations of the etalon signal, and 3) the confidence in the Voigt fit of the absorbance signal. The

uncertainty due to the FSR and peak location was determined by re-fitting the spectra after manual adjustment of the values in the algorithm. It was determined that the FSR error is $< 1\%$ on both the germanium etalon and the InF3 fiber etalon. A second order sine wave was fit through the peaks of the etalon signal to model the wavelength modulation of each laser. It was found that the area uncertainty due to peak location in the etalon signal was approximately 1% on each feature. The error due to the Voigt fit was determined by the root mean square value of the residual over each feature. The non-absorbing region of the absorbance was not considered as this would artificially lower the rms value of the residual over each feature and does affect the confidence in the area or linewidth of the Voigt fit to the data. In the first microseconds of the test the P(2, 20) feature has low SNR, thus increasing the uncertainty in the P(2, 20) fit. This has been accounted for in the analysis. The final values for the uncertainty in absorbance area are then estimated via Eq. 4.20. The representative uncertainty values for each line were determined by taking an average of the results of this analysis from all the tests. These values are used to generate the error bars shown Fig. 2.8 and 2.11.

$$\left(\frac{\delta A}{A}\right)^2 = \left(\frac{\delta A_{FSR}}{A}\right)^2 + \left(\frac{\delta A_{FSRfit}}{A}\right)^2 + \left(\frac{\delta A_{Voigtfit}}{A}\right)^2 \tag{2.16}$$

The uncertainty in T_{tr} is estimated using a similar Taylor series method shown in Eq. 3.7. The derivative is evaluated from rearrangement of Eq. 1.13. The uncertainty in Doppler width is again due to uncertainty in the FSR value, the fitting of the etalon peaks, and the Voigt fit. These three parameters are determined in the same way as previously described with one small difference. The effect of adjusting the FSR and peak locations is observed on Doppler width and not the area of each transition.

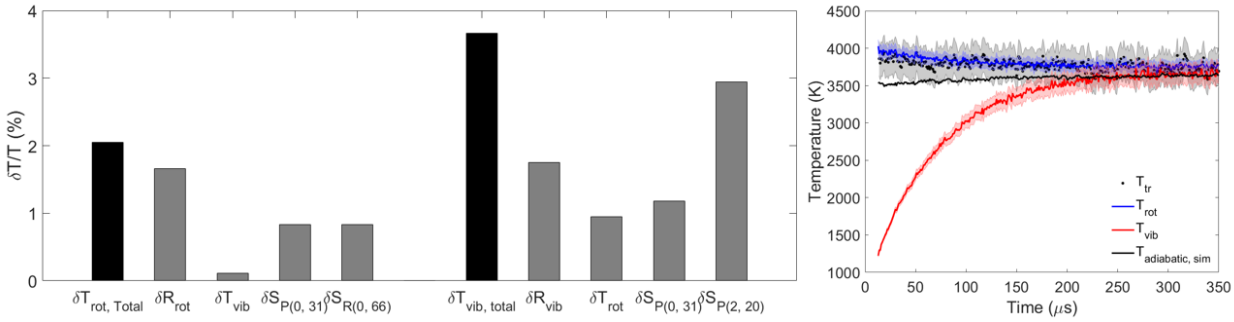

Figure 2.12: (left) Representative uncertainties for rotational temperature and (middle) vibrational temperature from each source of error considered. Total error for T_{vib} and T_{rot} shown in black taken as the rms value of all the sources. (right) Reflected shock test (25% CO - Ar, $U_{\text{is}} = 1423 \pm 10$ m/s) plotted with shaded error bars representing the uncertainty in the measurement.

$$\left(\frac{\delta T_{\text{tr}}}{T_{\text{tr}}}\right)^2 = \left(\frac{dT_{\text{tr}}}{d\Delta\nu_D}\left(\frac{\delta\Delta\nu_D}{\Delta\nu_D}\right)\frac{\Delta\nu_D}{T_{\text{tr}}}\right)^2 \tag{2.17}$$

The above uncertainty analysis has yielded results consistent with the data presented in Fig. 2.10. Calculated uncertainties in T_{tr} are between 5-6%, T_{rot} between 2-3%, and T_{vib} between 4-5%. Figure 2.12 shows the relative contributions of each term in the determination of δT_{rot} and δT_{vib}. It is evident that the area ratio uncertainty is the dominant factor in the determination of T_{rot}. This is attributed mainly to the Voigt fit of the R(0, 66) transition due to low signal to noise ratio. The area ratio and the linestrength uncertainty in the P(2, 20) feature are the most significant contributors to the uncertainty in T_{vib}. The T_{tr} uncertainty was again dominated by the uncertainty in Voigt fit over the three lines. Additionally, is observed that the uncertainties were least affected by each other because of proper line pair selection, where P(0, 31) and R(0, 66) are sensitive to T_{rot} and P(0, 31) and P(2, 20) are sensitive to T_{vib}.

Other contributions not included in this analysis are briefly discussed below. There is some uncertainty in the presumed known conditions in the shock tube. In the reflected shock cases,

the vibrational mode of the gas is assumed to be frozen during the incident shock. On tests that had equilibrium temperatures near 5000 K after the reflected shock, this assumption begins to come into question as the relaxation times in the incident region are shorter. A time-resolved solver may be more appropriate for shock conditions in these cases. Lastly, in the calculation of the pressure broadening ($\Delta\nu_C$), the pressure is set at the equilibrium pressure where, physically, there is a drop in pressure behind the incident shock wave due to the decrease in T_{tr}. The effects of this simplifying assumption are expected to be small as the broadening in a majority of the test cases is dominated by the Doppler component and not the pressure component. The collisional broadening parameters were adjusted by 50% on test cases $>$ 4000 K and showed minimal change in measured temperature ($<$ 1% for T_{rot} and T_{vib} and $<$ 5% for T_{tr}). This highlights the robust temperature measurement capability in significantly Doppler dominated conditions.

Chapter 3

Non-Equilibrium Carbon Dioxide Spectroscopy

3.1 Introduction

Mars and Venus planetary entries are governed by the non-equilibrium chemical kinetics (vibrational excitation, chemistry, and radiation) of shock heated CO_2. Flow temperatures just behind the bow shock can be in excess of 10,000 K, and around the shoulder of the vehicle, the shock-induced temperatures and pressures are significantly lower. The thermal protection system (TPS) in front of the vehicle typically experiences the highest heat loads, however the large volume of gas in the wake radiates with line of sight to the backshell and must be considered. Recent studies [8, 97, 17] have highlighted the need to investigate mid-infrared backshell radiation from vibrationally hot CO_2 to assess radiative heat loads that were once thought to be negligible. The most intense radiation from CO_2 occurs for temperatures between 2,000–3,000 K when the vibrational bands of CO_2 are excited and below the dissociation limit [8, 97]. In this study an optical diagnostic is developed to

probe multiple vibrational and rotational states of CO_2 in order to investigate thermal non-equilibrium associated with Mars backshell radiation.

The present study involves development and demonstration of a high-speed rovibrational multi-state sensing method for CO_2 in the mid-wave infrared using laser absorption spectroscopy, complementing the prior analogous work focused on CO [35]. Rapid tuning of a distributed-feedback interband cascade laser in a bias-tee circuit enables sub-microsecond spectral resolution of a cluster of rovibrational lines near 4.2 μm. The sensor is designed to investigate radiative heating rates expected on the backshell of Mars entry vehicles via quantitative investigations of shock-heated CO_2 between 1,500 - 3,000 K for comparison with multi-temperature and state-to-state models. The optical diagnostic is demonstrated for this purpose on a high-enthalpy shock tube for measurements of vibrationally excited CO_2 probing rotational absorption transitions in the ground and first-excited bending mode (01^10) of the fundamental asymmetric stretch bands centered near 4.3 μm. The multi-line measurement is used to infer multiple temperatures and state populations at MHz rates.

3.2 Methods and Theory

3.2.1 The infrared CO_2 spectrum

The carbon dioxide spectrum is complicated by multiple modes of vibration with different fundamental frequencies: symmetric stretch (ν_1, 1334 cm^{-1}), doubly degenerate bending (ν_2, 667 cm^{-1}), and asymmetric stretch (ν_3, 2349 cm^{-1}). Here we probe the strong absorption region near 4.3 μm which corresponds to the fundamental asymmetric stretch bands (ν_3) where $\Delta v_3 = 1$. The fundamental asymmetric stretch bands can be distinguished by lower vibrational level, denoted with vibrational quantum numbers $v_1 v_2^{l_2} v_3$ respectively, where l_2 characterizes the angular momentum of the molecule. Within the vibrational bands, rota-

tional lines are indicated X(J") where X is the branch (R, P, or Q) describing an increase, decrease, or no change in rotational quantum number, with J" being the lower state rotational assignment. The observed line intensities for absorption spectroscopy have a strong dependence on the population of the lower energy state. In this work, we probe two ν_3 fundamental bands, notated as $\nu_3(00^00)$ and $\nu_3(01^10)$, and several rotational lines within the R branch of these bands that span from J"=58 to J" = 143. The main distinction between the two bands utilized in this study is the lower vibrational energy level of the bending mode, as both bands originate from the ground vibrational state of the symmetric ($v_1 = 0$) and asymmetric ($v_3 = 0$) stretch. The target absorption transitions are shown in Fig. 3.1.

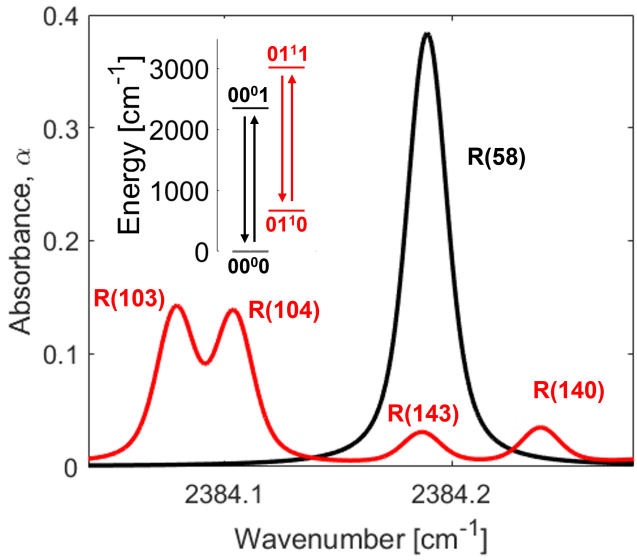

Figure 3.1: Simulated CO_2 spectrum using the HITEMP database [75]. The inset figure shows the energy level diagram of the vibrational states of CO_2 used in this study. Note the red color indicates transitions with v" = 01^10.

3.2.2 Laser absorption spectroscopy

In this work, laser absorption spectroscopy (LAS) is utilized to measure the R(58) line of the $\nu_3(00^00)$ fundamental band and the R(103), R(104), and R(140) lines of the $\nu_3(01^10)$ fundamental band of CO_2 via spectrally-resolved light attenuation in the mid-wave infrared,

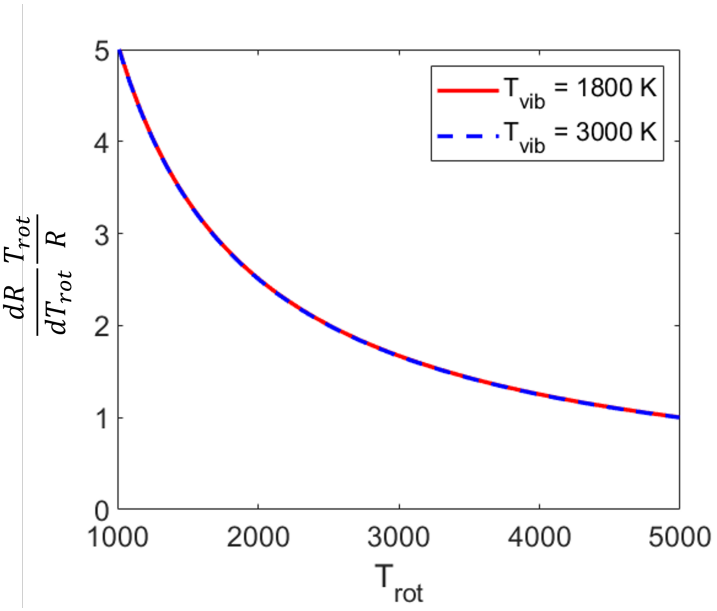

Figure 3.2: Rotational temperature sensitivity of the area ratio of the $\nu_3(01^10)$ R(103) and R(140) spectral features used in this study.

see Sec. 1.5. At the temperature and pressure conditions of the this study ($\Delta\nu_D/\Delta\nu_C \sim 2.0$), an accurate lineshape model is required to determine T_{tr}. The collisional broadening and temperature coefficients for CO_2-CO_2 and CO_2-Ar from Rosenmann et al. [74], and Lee et al. [47] were utilized as they were determined for similar rotational quantum numbers and in a similar temperature range as the present work. To evaluate 1.19, the rotational and vibrational energies are taken from Klarenaar et al. [42], and found to be in good agreement with the values listed in HITEMP [75] and calculated from Tashkun [88]. The partition functions of NEQAIR [68] were used in this study. The approach utilizing Eq. 1.16 is used in this study to determine T_{vib} for the purpose of enhanced sensitivity.

3.2.3 Line selection

The sensor was designed to probe multiple rotational and vibrational state populations of CO_2 between 2000 - 3000 K. The wavelength region of 4.19 μm (as presented in Fig 3.1) was selected for multiple reasons including: 1) the ease of resolving a clear baseline. Above

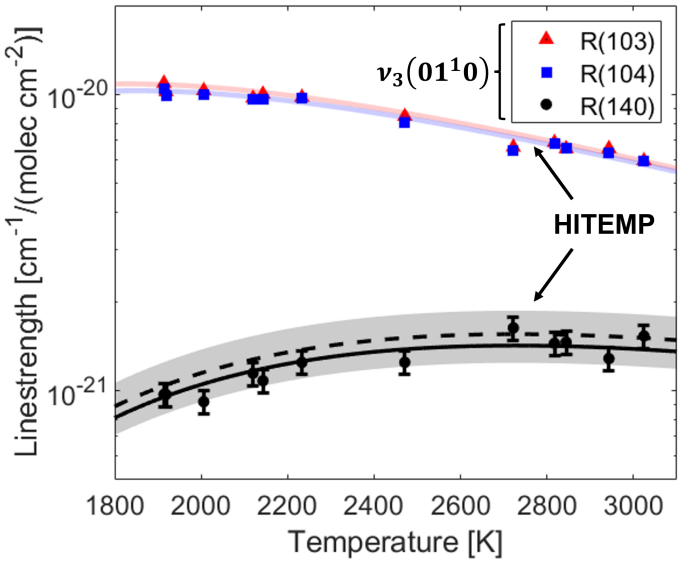

Figure 3.3: Measured equilibrium linestrength of the $\nu_3(01^10)$ R(103), R(104) and R(140) spectral features compared to the HITEMP model (dashed line and shaded regions) [75] over the temperature range of interest in this study. The solid line indicates the linestrength model used in this study to determine T_{rot}.

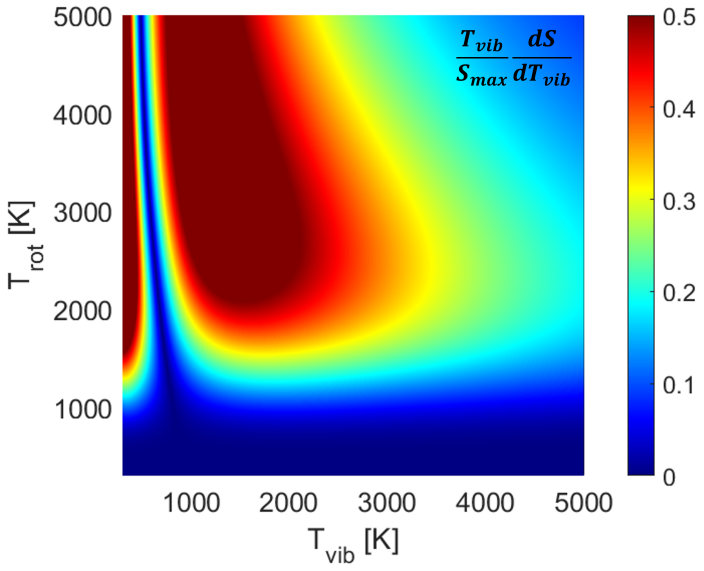

Figure 3.4: Vibrational temperature sensitivity versus rotational and vibrational temperature based on the $\nu_3(01^10)$ R(103) linestrength.

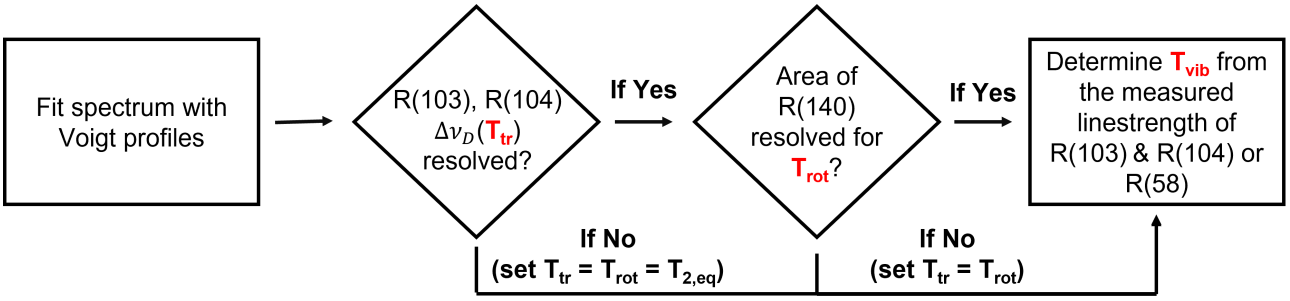

Figure 3.5: Solution method box diagram. Voigt profiles are fit to the spectrum to determine the integrated absorbance area and Doppler width.

1000 K, the CO_2 spectrum becomes increasingly blended toward the band center near 4.3 μm and this can increase the uncertainty in resolved absorbance areas; 2) Transitions from two different vibrational states are probed (as highlighted in Fig. 3.1), which is not practical at shorter wavelengths beyond the $\nu_3(01^10)$ bandhead; 3) The targeted spectral features are sufficiently isolated to resolve the absorbance areas of several individual transitions in a relatively small domain; 4) A wide range of rotational lower state energies are probed rendering the measurement sensitive to small changes in T_{rot}. This is highlighted in Fig. 3.2 with the non-dimensional rotational temperature sensitivity of the R(103) and R(140) features plotted against T_{rot} at two different vibrational temperatures. R is the absorbance area ratio of R(103) and R(140) shown in Eq. 1.17. A value greater than 1 generally indicates a sensitive measurement [85]. As noted, because the R(103) and R(140) features are from the same vibrational band (01^10), the area ratio is insensitive to changes in T_{vib}.

To determine T_{rot}, the R(140) absorbance area must be separated from the R(58) absorbance area. This is achieved via sequential fitting where the initial fit of the R(58) feature is subtracted out of the spectrum and the R(140) is fit allowing a quadratic polynomial to capture any residual curvature of the baseline. To check the efficacy of this method at known conditions, shock tube experiments were run to produce equilibrium non-reacting conditions and infer line strengths of the target CO_2 transitions, shown in Fig. 3.3. The measured values were compared to calculated linestrengths from HITEMP [75]. The measurements in this study are within the uncertainty values listed in HITEMP (1-2% for the R(103) and

R(104) features, and $\geq 20\%$ for the R(140) feature). On average, the R(140) linestrengh was measured to be 8.5% below the HITEMP value which is within the tabulated uncertainty, thus an adjustment of 8.5% was applied for data processing. This is highlighted by the solid line in Fig. 3.3.

The vibrational temperature is determined once T_{rot} is known via numerically solving Eq. 1.16 and comparing to the measured linestrength determined from the absorbance area, $\mathcal{A}_j$. Critically, this is only feasible when mole fraction is known, as is generally expected for conditions < 3000 K, thus rendering the line intensity a function of multiple temperatures. Figure 3.5 illustrates the solution method. The density profile behind the incident shock is modeled by an exponential increase from the vibrationally frozen density predicted from the normal shock relations solver [10] to the equilibrium number density after relaxation. Figure 3.4 shows the absorbance area of the R(103) feature is most sensitive to T_{vib} over the temperature range of 1500–3000 K. While any line area may be theoretically used to infer a T_{vib} value, the R(103) and R(104) lines are preferentially used here as R(58) can be optically thick, and R(140) is often optically thin. It should be noted for temperatures > 3000 K, dissociation starts to affect the absorbance area and the uncertainty of T_{vib} increases significantly unless the number density of CO_2 can be determined in an alternate way. Addressing this limitation is less critical given that at temperatures instigating dissociation, vibrational relaxation is very short, meaning that state populations approach a single temperature distribution (i.e. thermal equilibrium).

Lastly, the population fraction of the rovibrational state i, N_i/N where N is the total CO_2 population, can be derived from Eqs. 1.16 & 1.18 using the absorbance area, $\mathcal{A}_i$, as shown in Eq. 3.1, provided the stimulated emission (N_2/N) can be estimated.

$$\frac{N_i}{N} = \frac{g_i}{g_2}\left(\frac{8\pi\nu^2 c\mathcal{A}_i}{A_{21}NL} + \frac{N_2}{N}\right) \tag{3.1}$$

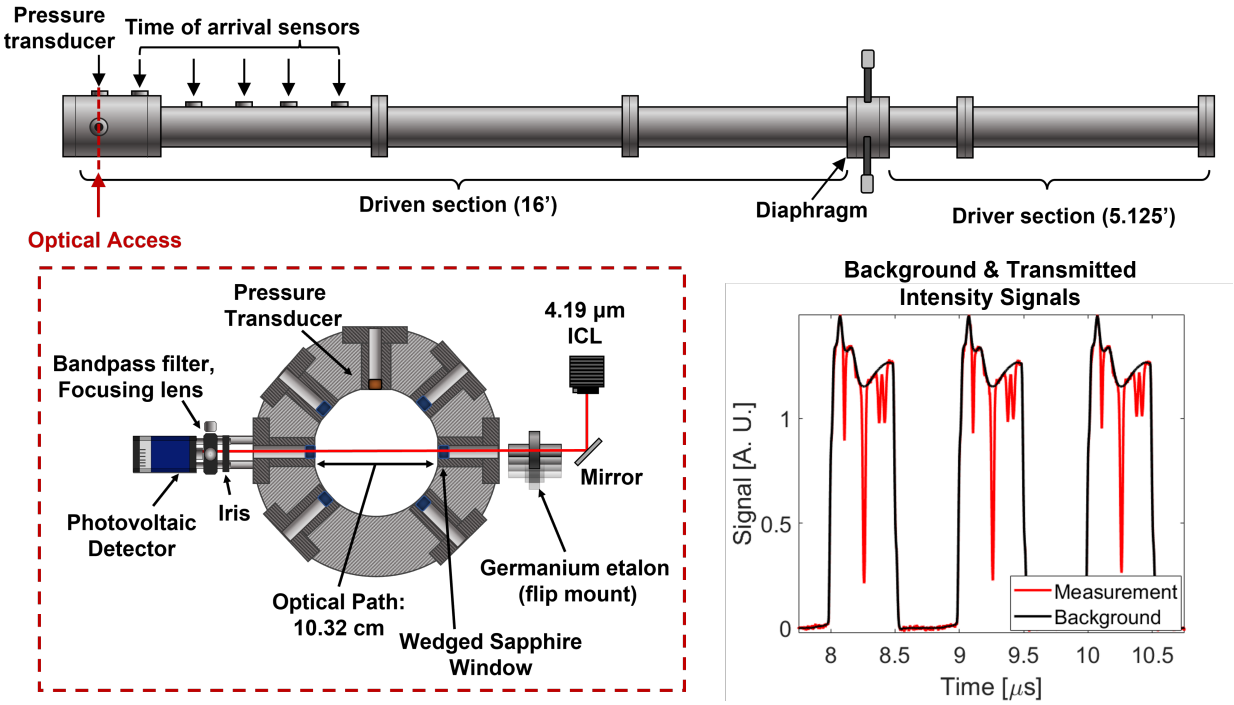

Figure 3.6: (top) Shock tube schematic. (left) Sensor layout through the optical access location 2 cm from the endwall. (right) Background and transmitted light intensity signals during an incident shock. Note the transient intensity in the measurement signal.

3.3 Optical and Experimental Setup

The optical and experimental setup is shown in Fig. 3.6. An interband cascade laser is used to resolve four rovibrational lines of the asymmetric stretch fundamental bands of CO_2 near 4.19 μm described above in Sec. 3.2.3. The laser is controlled using an RF-diplexer (bias-tee) circuit as described in [62]. A square waveform is used, as this type of modulation maximizes the signal intensity, and hence optimizes the signal to noise ratio (SNR) during the scan. An additional benefit of the square waveform includes the sharp temperature difference the laser chip experiences between the up and down scans. This temperature difference is what drives the wavelength change during the scan, and therefore the square wave maximizes the scan-depth (the range of wavelengths generated) for a given amplitude of current modulation. Additional details on improving the scan-depth using arbitrary waveforms are given in Nair et al. [64].

The sensor has a relatively simple optical setup as shown in Fig. 3.6. Key hardware and sensor operation is briefly discussed here. It can be seen in the sample laser scans of Fig. 3.6 that the laser is scanned below the lasing threshold. This allows for an accurate accounting of the emission during each scan, and the detector dark signal to be known immediately before the test. The total integration time of one scan is 500 ns, as the laser is effectively off (not emitting) when the current is below the lasing threshold limit. This scan function yields an effective measurement rate of 1 MHz. A 2-inch germanium etalon is used to convert light intensity signals from the time domain to the wavenumber domain. The background intensity and etalon signals are recorded immediately before each run. Additional hardware include a narrow bandpass filter and iris to mitigate the emission signal prior to light detection. Two wedged sapphire windows were used to seal the shock tube and prevent etalon signals between the two windows, and a focusing lens was used to collect the light onto a high bandwidth ($\sim$200 MHz) photovoltaic detector and mitigate beam steering. Additionally, beam steering tests were performed throughout the test series to ensure accurate measurements immediately behind the passage of the incident shock. Lastly, the data acquisition system has a bandwidth of 200 MHz and recorded signals at 12-bits and a sampling rate of 1.25 GS/s providing high-SNR measurements of the raw light intensities.

A high enthalpy shock tube (HEST) at UCLA was used for all experiments in this work to shock-heat CO_2 - Ar over a range of incident shock velocities up to 2.7 km/s relevant to Mars entry backshell heating. Different mixtures of CO_2 - Ar were used with CO_2 concentrations of 2%, 20%, and 100%. The facility is well documented in literature [3] and briefly described here. The stainless-steel tube consists of a 5.125 ft cold gas driver and a 16 ft driven section with 5 piezoelectric transducers integrated along the length of the driven section to measure the shock position/time of arrival and infer shock velocity. A high-speed pressure transducer (Kistler 601B1) and optical access are located 2 cm from the endwall. Before each test, a turbopump is used to achieve an ultimate vacuum pressure on the order of 100s of µtorr and leak rates are measured via rate of rise on a Baratron manometer (627D) and were in the

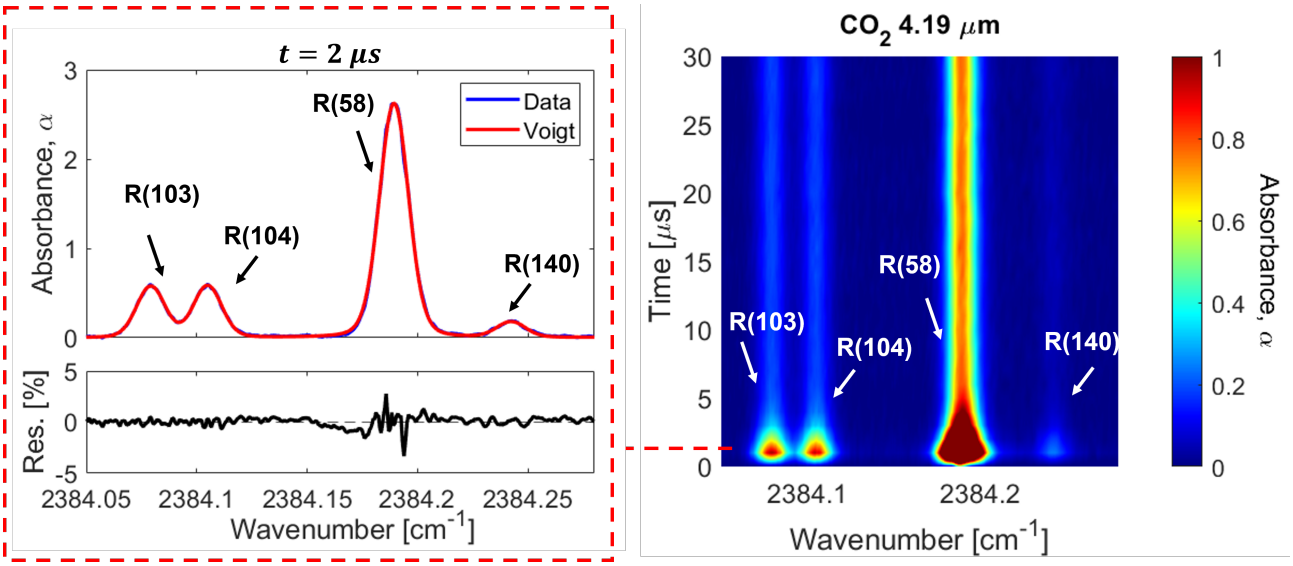

Figure 3.7: (left) Voigt Fit of the spectra at t = 2 μs into the test. (right) 2D map of absorbance versus time and wavenumber. Shock conditions: Fill pressure = 1.30 Torr, 20% CO_2 - Ar, U_{is} = 1855 $\pm$ 15 m/s.

range 0.1 - 1 mtorr/min.

3.4 Results/Sensor Demonstration

Based on the sensing strategy and experimental setup outlined in the previous sections, a series of tests were performed to validate the sensor at controlled conditions. Additionally, a number of tests were conducted to examine thermal non-equilibrium of CO_2 and associated vibrational relaxation timescales, with comparison to existing models.

3.4.1 Multi-temperature Validation

Incident shock waves with velocities between 1.1 - 2.7 km/s in CO_2 - Ar gas mixtures were studied to determine the range, accuracy and precision of the sensor with regards to translational, rotational, and vibrational temperature measurements. Equilibrium temperatures

were achieved between 1250 - 3100 K and equilibrium pressures ranged from 0.03 - 0.17 atm. These conditions prevented any CO_2 dissociation during the test time.

As described in Sec. 3.2, the temperatures of rotation and vibration are related to the population distribution of CO_2 and determined from the absorbance area measurements of the R(58), R(103), R(104), and R(140) rovibrational lines in the ν_3 bands. Figure 3.7 (right) shows a representative absorbance signal resolved versus wavenumber and time. A clear intensity reduction occurs in the first 5 microseconds of the test, related to a population decrease in the v" = 00^00 and v" = 01^10 energy levels. The population fractions are plotted versus time using Eq. 3.1 and compared with the 2-temperature vibrational relaxation model of Simpson et al. [79] in Fig. 3.8. The observed decrease in population fraction of these states is expected because the ground and first bending mode are low vibrational states ($E_{vib,01^10}$ = 667 cm^{-1}). Therefore, they will depopulate during vibrational excitation at temperatures greater than approximately 1000 K. After the initial transient, strong agreement is observed with the simulated equilibrium population fraction. The time axis is given in particle time as this facilitates easier comparisons to relaxation rates given in literature and is related to the lab frame via Eq. 3.2 [20].

$$\Delta t_{particle} = \frac{\rho_2}{\rho_1} \Delta t_{lab} \tag{3.2}$$

At this condition, good agreement is generally observed between the values predicted from Simpson et al. [79] throughout the entire test.

Time resolved temperatures determined using the process outlined in Fig. 3.5 are presented in Figs. 3.9 and 3.10 for temperatures near 2100 K and 3000 K, respectively. A clear energy transfer is observed behind the incident shock passage at t = 0 from the translational and rotational energy modes to the vibrational energy mode. This relaxation is due to to both vibration-vibration (VV) and vibration-translation (VT) exchange processes in the gas.

For the case presented in Fig. 3.10, good agreement is seen between the translational and rotational energy modes of the gas. This is expected because translational and rotational energy modes equilibrate significantly faster than the vibrational energy mode [43, 45]. The energy modes are also seen to equilibrate to the temperature predicted from the normal shock relations solver [10], indicating an accurate and quantitative temperature measurement.

Further tests were conducted to validate the sensor over a range of temperatures of interest (1250 - 3100 K) and assess its limitations. Measured equilibrium temperatures are compared to the normal shock relations solver [10] and results are presented in Fig. 3.11. Representative error bars are calculated using the method described in Sec. 3.6 largely following the analysis described in [60, 62]. In this figure, the representative error bars are estimated as 7% for T_{tr}, 4% for T_{vib}, and 8% for T_{rot}. Note rotational temperatures are reported on 100% CO_2 cases where the R(140) feature can be sufficiently resolved. Below ∼2200 K, where the R(140) can not be well-resolved, the rotational and translational temperatures can not be determined independently and are thus assumed to be equal. The primary domain of operation for multi-temperature sensing is 1900–3100 K. In more dilute gas mixtures wherein translational and rotational temperatures are equilibrated immediately behind the shock and determined by normal shock relations, the vibrational temperature may still be measured independently, demonstrated here down to 1250 K. The average discrepancy between measured temperatures in the equilibrium region with calculated temperatures from normal shock relations is ∼4%. The average standard deviation (2σ) of the measured temperatures after vibrational relaxation is found to be 105 K for T_{tr}, 164 K for T_{rot} and 106 K for T_{vib}, on the order of 5% of the measurement values, representing measurement precision.

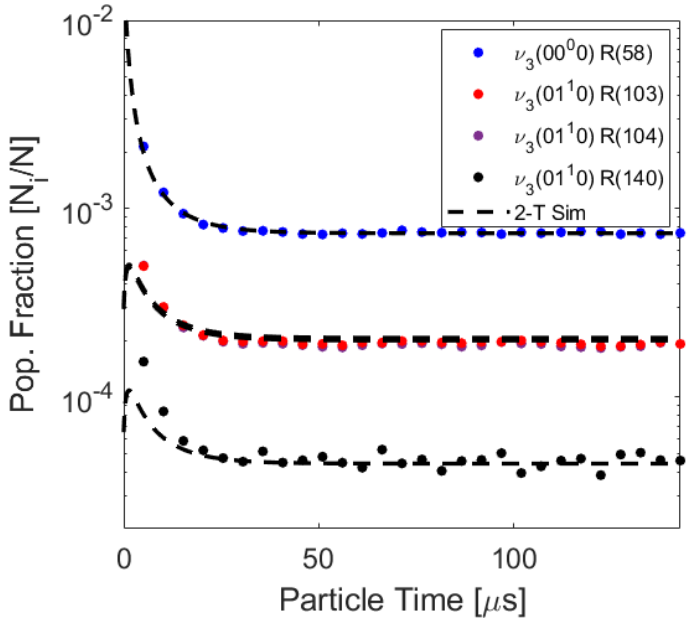

Figure 3.8: Measured populations versus time compared to the two temperature Simpson relaxation time model [79] from the normal shock relations solver [10]. Shock conditions: Fill pressure = 1.30 Torr, 20% CO_2 - Ar, U_{is} = 1855 ± 15 m/s.

3.4.2 Vibrational Relaxation Timescales

From resolved vibrational temperature trends, vibrational relaxation time is determined and compared to the models of Simpson [79] and Park [72]. The Simpson model was developed from a laser Schlieren technique which measured the density change during vibrational relaxation behind incident shock waves in CO_2 - Ar mixtures. The Park model was fit to the pure CO_2 data of Carmac [12] and relies on the correlation formula of Millikan and White [59] to estimate the vibrational relaxation rate with Ar. The functional form of each model is subtly different, with Park adding an additional term to prevent the vibrational excitation rate from exceeding the elastic collision cross section (σ'). The value Park lists for σ' has negligible effect at the conditions of this study.

The fitting procedure used to determine τ_{vib} in this work follows from the Bethe-Teller

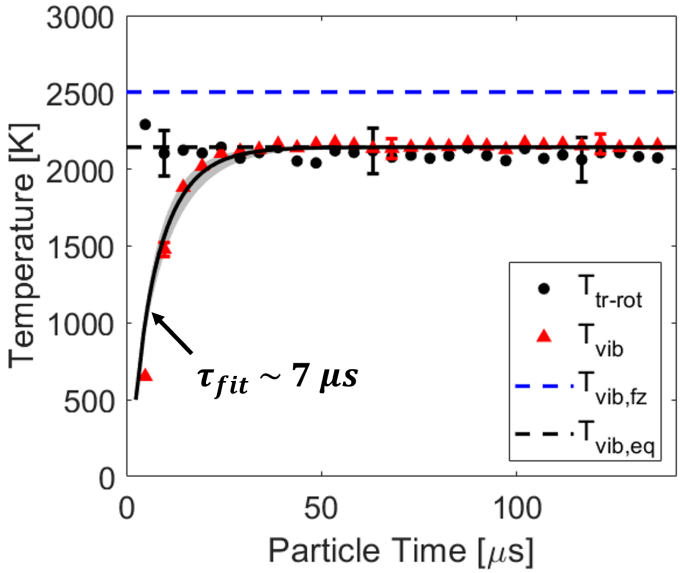

Figure 3.9: Time resolved temperatures compared to the normal shock relations solver [10]. Shock conditions: Fill pressure = 3.50 Torr, 20% CO_2/Ar, U_{is} = 1612 ± 11 m/s.

equation shown in Eq. 3.3.

$$\frac{de_{\text{vib}}}{dt} = \frac{e^*_{\text{vib}}(T_{\text{tr}}) - e_{\text{vib}}(T_{\text{vib}})}{\tau_{VT}} \tag{3.3}$$

e^*_{vib} is the vibrational energy the gas would have if it were at the translational temperature of the gas. The vibrational energy of the gas is calculated from the measured vibrational temperature via Eq. 3.4 assuming three separable modes of vibration, and a simple harmonic oscillator to approximate the energy level spacing within the modes. Θ_{vib} [K] is the characteristic vibrational temperature of the mode and k is the Boltzmann constant. The solution of the Bethe-Teller equation for a bath gas is given in Eq. 3.5, and is linearly fit on a log plot to determine τ_{VT} from the slope. $e_{vib}(T_{vib,i})$ is the initial vibrational energy of the gas before relaxation.

$$e_{vib} = \frac{n_A k \Theta_{vib}}{\exp(\frac{\Theta_{vib}}{T_{vib}}) - 1} \tag{3.4}$$

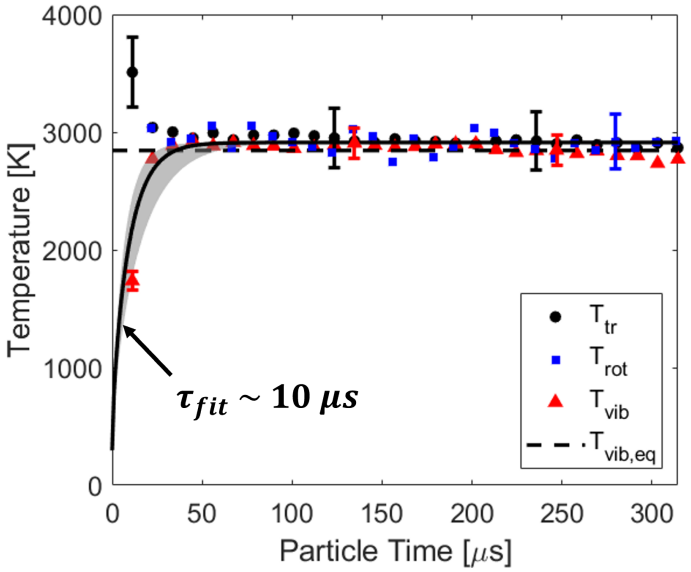

Figure 3.10: Time resolved temperatures compared to the normal shock relations solver [10]. Shock conditions: Fill pressure = 0.36 Torr, 100% CO_2, U_{is} = 2562 ± 24 m/s. Note the vibrationally frozen temperature is estimated at 5100 ± 94 K and not shown on the figure.

$$\frac{e^*_{vib}(T_{eq}) - e_{vib}}{e^*_{vib}(T_{eq}) - e_{vib}(T_{vib,i})} = \exp\left(\frac{-t}{\tau_{VT}}\right) \tag{3.5}$$

The fitted relaxation time fit is shown in Fig. 3.10 and estimated to be 7 ± 2 μs, based on the uncertainty in the fitted slope. The vibrational relaxation times were fit over the range of conditions investigated in this study and are presented in Fig. 3.12. Good agreement is seen with the data measured by Kamimoto et al. [41] who studied mixtures ≤ 4% CO_2 - Ar with an emission technique. For dilute CO_2 in argon, the Simpson model [79] was found to be largely within the uncertainty of the measurements. The Park rate for CO_2 - Ar is based off an empirical correlation formula developed by Millikan and White [59]. Therefore, it is expected that the experimentally determined rate of Simpson better captures the data. Additionally, the Simpson model predicts faster vibrational relaxation with increasing CO_2 concentration and this is consistent with the measurements of this study.

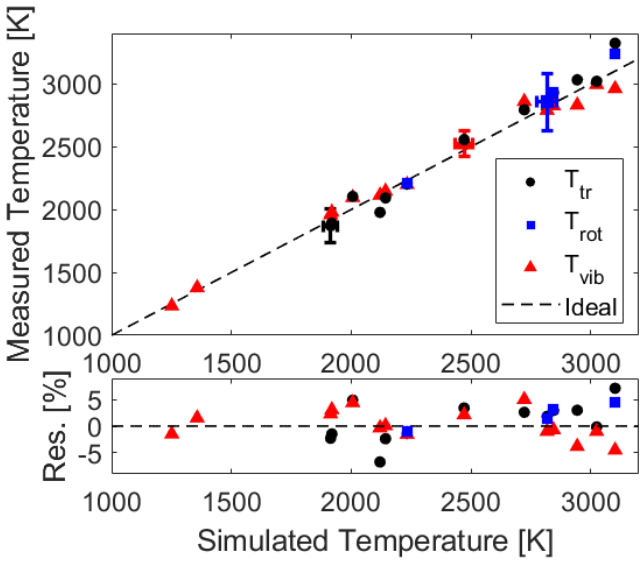

Figure 3.11: Mean equilibrium temperatures of translation, rotation, and vibration compared to the normal shock relations solver [10]. Temperature ranges from 1250 - 3100 K.

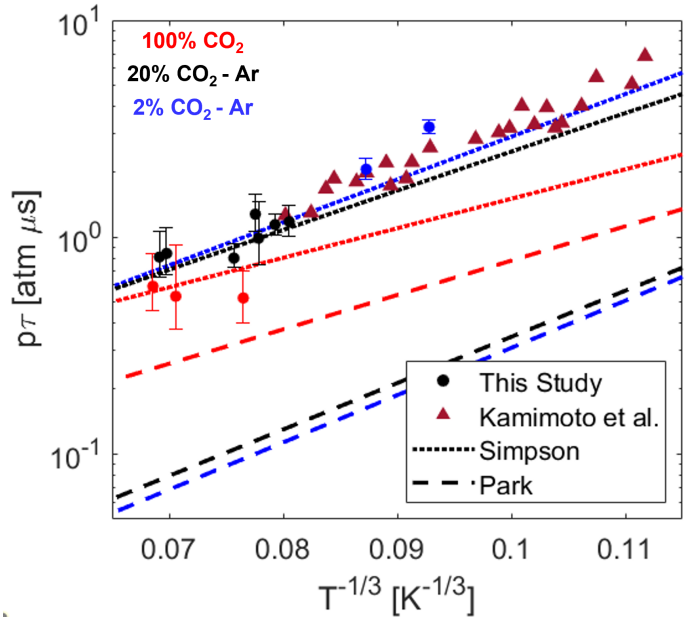

Figure 3.12: Landeau-Teller plot of relaxation times measured in this study compared to literature. Mixture concentrations are denoted with the blue (2% CO_2-Ar), black (20% CO_2-Ar), red (100% CO_2) color scheme.

3.4.3 State Population Analysis

In addition to multi-temperature analysis, the spectroscopic technique may be used to infer state-specific populations (per Eq. 3.1) in thermal non-equilibrium and inform state-to-state modeling efforts. Figure 3.13 demonstrates one case of particular interest at the low end of the investigated shock velocities. The measured population fractions of two rovibrational states (01^10, J"=103 and J"=104) are compared to the calculated ones assuming a single vibrational temperature and the Simpson relaxation time. At this test condition, and a few others at similarly weak shock velocities, the multi-temperature solution method failed to recover a T_{vib} from the first several recorded spectra after the shock front. This was particularly noticeable on the lowest CO_2 concentration test cases where VV rates are expected to have the least effect due to the limiting of CO_2 - CO_2 collisions and also where the kinetics are expected to be the slowest at low temperatures. Since T_{vib} is determined from Eq. 1.16, and the number density and pathlength are well known, it is suspected the two temperature linestrength model (Eq. 1.19) is not valid at these conditions. A clear overpopulation of the 01^10 states are measured for approximately 25 μs of particle time. To generate the model uncertainty displayed in Fig. 3.13 as the shaded region, the listed 2% uncertainty in the database linestrength value was considered along with the partition function uncertainty. The partition function was simulated at both the vibrationally frozen rotational temperature (1375 K) and vibrationally equilibrated rotational temperature (1357 K). These temperatures are very similar because the CO_2 is very dilute (2%) in Ar. It is observed the uncertainty in T_{rot} and the uncertainty in the evaluation of the partition function cannot explain the gap between the measured population fraction and the two temperature model, though the timescale is well captured by the Simpson rate [79].

The likely explanation of the result displayed in Fig. 3.13 is non-equilibrium between the bending and asymmetric stretch vibrational modes ($T_{vib,bend} \neq T_{vib,as}$). It is known the asymmetric stretch temperature, $T_{vib,as}$, relaxes slower than the symmetric stretch and bending

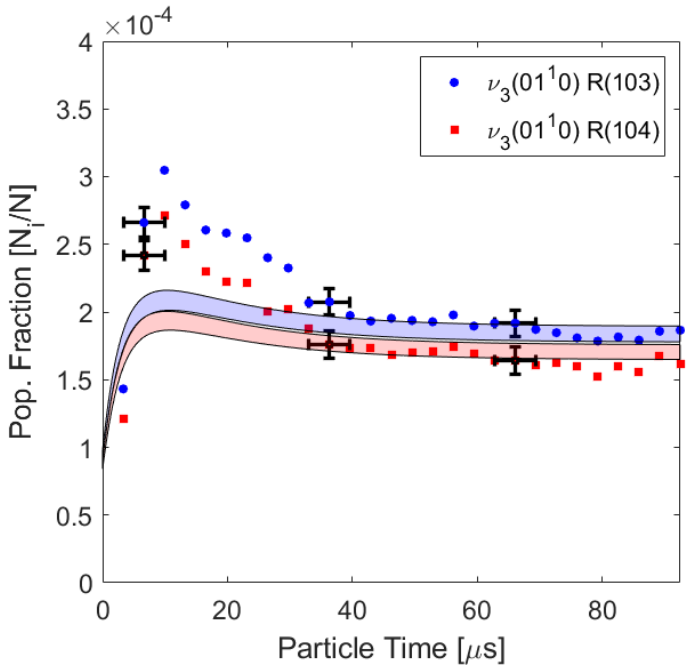

Figure 3.13: Time-resolved population fractions in an incident shock compared to a two-temperature model assuming the relaxation rate of Simpson et al. [79]. Shock conditions: Fill pressure = 5.60 Torr, 2% CO_2/Ar, U_{is} = 1116 ± 7 m/s.

modes [45]. If $T_{vib,as}$ is lower than $T_{vib,ss}$ and $T_{vib,bend}$, the stimulated emission term in Eq. 3.1 is overestimated. Thus, lowering $T_{vib,as}$ would decrease the inferred population fraction of this state from the absorbance data. Simultaneously, lowering $T_{vib,as}$ would increase the expected population fraction in the level, thus bringing the measurement and the model into better agreement. Rigorously testing this hypothesis is beyond the scope of this paper, but it is clear that the MHz-rate state population measurements enabled by the sensing method provide an opportunity for such future work.

3.5 Conclusion

A mid-IR laser absorption sensor has been developed and demonstrated to probe several ro-vibrational state populations of CO_2 at MHz rates in shock-induced thermal non-equilibrium relevant to Mars entry heating. Shock tube tests were performed to examine sensor capability

with shock velocities between 1.1 km/s - 2.7 km/s in various CO_2-Ar gas mixtures ranging from 2%, 20%, and 100% CO_2. Quantitative state populations are used to infer translational, rotational and vibrational temperatures. Pressure and equilibrium temperature conditions ranged from 0.03 - 0.17 atm and 1250 - 3100 K. This sensing method was shown to provide quantitative results for temperature across this range, with estimated uncertainties of 7% for T_{tr}, 4% for T_{vib}, and 8% for T_{rot}. Demonstrated temperature precision was approximately $\sim$100 K for each energy mode. The high effective precision, accuracy, and temporal resolution (1 µs in the lab frame) of this sensor demonstrates its potential for use to investigate the complex vibration - dissociation dynamics of CO_2.

From the tests performed in this work, thermal non-equilibrium was investigated and compared to rates of vibrational excitation predicted from the Park [72] and Simpson [79] models. Our results show good agreement with the Simpson model and the measurements of Kamimoto et al. [41]. On a few tests cases at low shock velocity, a single vibrational temperature could not be determined at early test times. This was primarily observed on low temperature tests highly dilute in Ar, likely due to the limiting of VV exchanges during CO_2-CO_2 collisions and low collision rates in this temperature range. It should be noted that the rate model of Simpson [79] still predicted the relaxation timescale well at these conditions, however the two temperature linestrength model fails in the prediction of the population distribution of the (01^10) state. Non-equilibrium between the asymmetric stretch and bending vibrational modes likely explains the discrepancies between the two-temperature model and measured population fractions. Further analysis requires a model of the asymmetric stretch temperature or additional spectra collected in higher asymmetric stretch states. In summary, a new high-speed laser absorption sensing technique has been developed to investigate CO_2 non-equilibrium processes at relevant temperatures and pressures to Mars backshell heating and demonstrated to yield quantitative results to refine non-equilibrium rate models. This diagnostic can be used to complement the state-of-the-art emission diagnostics utilized by various groups to reduce uncertainties in models of thermal non-equilibrium between

translational, rotational, and vibrational energy modes of CO_2.

3.6 Uncertainty Analysis

3.6.1 Temperature Uncertainty Analysis

This section describes the calculation of uncertainty based on the Taylor series method of error propagation and assuming uncorrelated sources of uncertainties [6]. The non-dimensional uncertainty of a dependent variable r (δr/r) can be calculated from the uncertainty in the independent variables (δx$_i$) used to calculate r as shown in Eq. 4.18.

$$\left(\frac{\delta r}{r}\right)^2 = \sum_i \left(\frac{\partial r}{\partial x_i}\frac{\delta x_i}{x_i}\frac{x_i}{r}\right)^2 \tag{3.6}$$

For the uncertainty in translational temperature, uncertainty in the free spectral range (FSR) of the etalon used to make the time to wavenumber transform is considered as well as the uncertainty in the collision width and Voigt fit as shown in Eq. 3.7 and 3.8.

$$\left(\frac{\delta T_{tr}}{T_{tr}}\right)^2 = \left(\frac{\partial T_{tr}}{\partial \nu_D}\frac{\delta \nu_D}{\nu_D}\frac{\nu_D}{T_{tr}}\right)^2 \tag{3.7}$$

$$\left(\frac{\delta \nu_D}{\nu_D}\right)^2 = \left(\frac{\delta \nu_{D,FSR}}{\nu_D}\right)^2 + \left(\frac{\delta \nu_{D,\Delta\nu_C}}{\nu_D}\right)^2 + \left(\frac{\delta \nu_{D,Fit}}{\nu_D}\right)^2 \tag{3.8}$$

The derivative of T_{tr} with Doppler width is easily calculated from Eq. 1.13. The FSR uncertainty is estimated at 1% and the spectrum is re-fit with the adjusted FSR. The uncertainty in collision width for CO_2-CO_2 collisions from Rosenmann et al. [74] is listed as 7%, and CO_2-Ar collision width uncertainty is 3% from the values listed in Lee et al. [47]. The

Voigt fit uncertainty is taken as the root mean square of the residual of the fit over the spectral features estimated as approximately 2.5%. Note that as the temperature increases and pressure decreases, the uncertainty due to the collision width will diminish, increasing the precision of the T_{tr} measurement. Figure 3.14 (left) shows the relative contributions of each source of error in the Doppler width measurement. The primary sources of uncertainty arise in the fit, and in the collision width.

The uncertainty in vibrational temperature is determined from the uncertainty in absorbance area, linestrength, and rotational temperature via Eq. 3.9.

$$\left(\frac{\delta T_{vib}}{T_{vib}}\right)^2 = \left(\frac{\partial T_{vib}}{\partial A}\frac{\delta A}{A}\frac{A}{T_{vib}}\right)^2 + \left(\frac{\partial T_{vib}}{\partial S}\frac{\delta S}{S}\frac{S}{T_{vib}}\right)^2 + \left(\frac{\partial T_{vib}}{\partial T_{rot}}\frac{\delta T_{rot}}{T_{rot}}\frac{T_{rot}}{T_{vib}}\right)^2 \tag{3.9}$$

The uncertainty in absorbance area A can be estimated via Eq. 4.20, where α_{pk} is the peak absorbance of the transition [60].

$$\frac{\delta A}{A} = \frac{1}{SNR}\left(\frac{\exp(\alpha_{pk})}{\alpha_{pk}}\right) \tag{3.10}$$

The derivative of vibrational temperature with area and linestrength is calculated numerically from Eq. 1.16 and Eq. 1.19. The derivative of T_{vib} with T_{rot} is determined numerically via a perturbation approach where T_{vib} is recalculated after T_{rot} is perturbed in the model (consistent with the estimated uncertainty of T_{rot} on a given test). δS/S is estimated from the uncertainty value in the reference linestrength listed in HITRAN [28] for R(103) and R(104) (2 %) and HITEMP [75] for R(140) (20%), as the R(140) feature is not listed in HITRAN. For the R(103) and R(104) features used to measure T_{vib}, the relative error from each term in Eq. 3.9 is shown in Fig. 3.14. The two primary sources of error are the uncertainty in rotational temperature and uncertainty in absorbance area fit. As this analysis shows, uncertainty in T_{vib} is strongly correlated to the T_{rot} uncertainty and could be further reduced if needed by improving the T_{rot} accuracy.

Rotational temperature uncertainty can be estimated via Eq. 4.19 (see Minesi et al. [60]), provided the spectral features are within the same vibrational band.

$$\frac{\delta T}{T} = \frac{k_B}{hc}\frac{T}{\Delta E}\sqrt{\sum_{i=1}^{2}\left(\frac{\delta S_i}{S_i}\right)^2 + \left(\frac{\delta A_i}{A_i}\right)^2} \tag{3.11}$$

Considering the fundamental $\nu_3(01^10)$ R(103) and R(140) features used in this work, the estimated uncertainty is 13% assuming the HITEMP value of 20% for δS/S of R(140). Based on the consistency of our measurements validated via normal shock relations, we estimate δS/S to be 10% for the R(140) feature, thus yielding a more realistic uncertainty of 8% for $\delta T_{rot}/T_{rot}$.

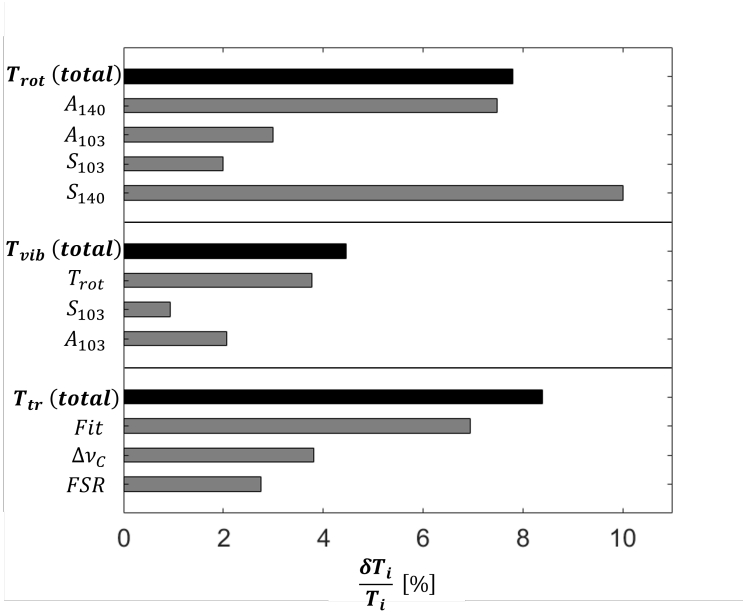

Figure 3.14: Calculated relative uncertainty contribution from each term in Eq. 4.19 (top), Eq. 3.9 (middle), & Eq. 3.8 (bottom) for the case presented in Fig. 3.10.

3.6.2 Non-equilibrium T_{vib} sensitivity

Vibrational temperature is determined from the absolute area measurement of the R(103) and R(104) spectral features in the 01^10 vibrational lower state in this work. It is hypothe-

sized that non-equilibrium between vibrational modes may exist at certain conditions in this study. Sensitivity of the area measurement was analyzed with respect to different vibrational temperatures. The analysis requires the T_{vib} and E_{vib} terms in Eq. 1.19 to be separated into three separate terms with an associated temperature for each mode: symmetric stretch - $T_{vib,ss}$, bending - $T_{vib,bend}$, and asymmetric stretch - $T_{vib,as}$. The linestrengh expression then becomes Eq. 3.12 and the non-equilibrium partition function can be calculated using the Klarenaar model [42]. To simplify the calculation, we assume $T_{vib,ss} = T_{vib,bend}$, as this is often assumed due to Fermi resonance between these modes.

$$S_j = \frac{A_{21} g_2}{8\pi\nu^2 c Q_{\mathrm{rot}}(T_{\mathrm{rot}}) Q_{\mathrm{vib}}(T_{\mathrm{vib,ss}}, T_{\mathrm{vib,bend}}, T_{\mathrm{vib,as}})} \left[\exp\left(\frac{-c_2 E_{\mathrm{rot},1}}{T_{\mathrm{rot}}}\right) \exp\left(\frac{-c_2 E_{\mathrm{vib,bend},1}}{T_{\mathrm{vib,bend}}}\right) - \exp\left(\frac{-c_2 E_{\mathrm{rot},2}}{T_{\mathrm{rot}}}\right) \exp\left(\frac{-c_2 E_{\mathrm{vib,bend},2}}{T_{\mathrm{vib,bend}}}\right) \exp\left(\frac{-c_2 E_{\mathrm{vib,as},2}}{T_{\mathrm{vib,as}}}\right) \right] \quad (3.12)$$

The sensitivity to each vibrational temperature can be calculated by taking the respective temperature derivative of each mode. This is done numerically and shown in Fig. 3.15 at T_{tr-rot} = 2250 K. The sensitivity of each vibrational mode temperature is not a strong function of rotational temperature. It is observed that the dominant signal in the area of the R(103) (and similarly R(104)) transition is the bending mode temperature over the entire range investigated in this study (T = 1250–3000 K). The R(103) area is approximately twice as sensitive to the bending mode temperature when compared with the asymmetric stretch temperature. This is expected as $T_{vib,as}$ effects the stimulated emission of the resolved areas, and its influence grows with increasing $T_{vib,as}$. In conclusion, this analysis shows the relative influence of potential non-equilibrium across the vibrational modes on the state populations inferred from the R(103) and R(104) lines. At early test times, if $T_{vib,bend} > T_{vib,as}$, the sensor can be interpreted as resolving mostly the bending mode temperature with a high degree of confidence considering the curves in Fig. 3.15.

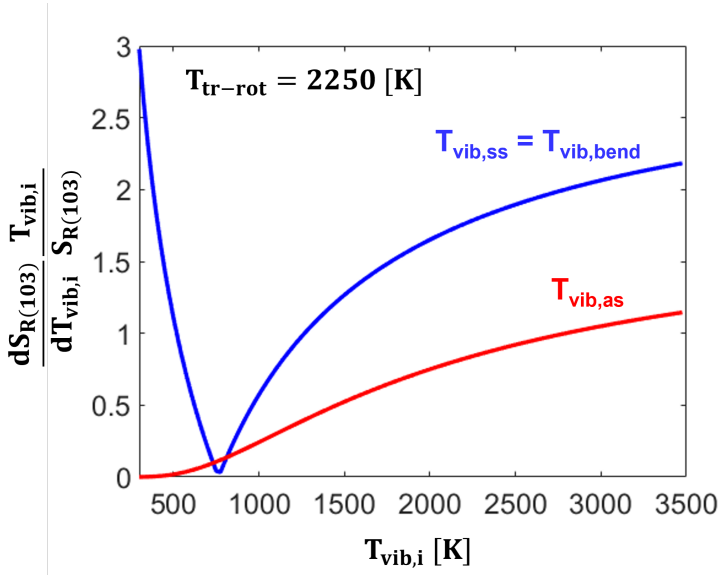

Figure 3.15: Calculated sensitivity of the $\nu_3(01^10)$ R(103) area to the bending mode temperature and asymmetric stretch mode temperature as a function of respective vibrational mode temperature.

Chapter 4

Multi-Species Sensing at NASA EAST Facility

4.1 Motivation: Mars2020 and the MEDLI2 Sensor Suite

The sensor developed in chapters 2 and 3 was modified for deployment at the Electric Arc Shock Tube (EAST) facility at NASA Ames from October 2021 - April 2022 (Test series 64A) to study a re-created shock layer experienced by the Mars2020 entry vehicle.

The Mars2020 mission successfully landed the Perseverance rover within the Jezero crater at the Octavia E. Butler landing site on February 18, 2021. The aeroshell of the Mars2020 mission was instrumented with the MEDLI2 sensor suite [16, 57, 86] to conduct measurements of the aerothermal environment upon entry, descent, and landing (EDL). Temperatures were recorded at multiple locations via thermocouples. Total heat flux was recorded on the backshell by two sensors (MEDTHERM, Model 22171-01KS) and the backshell radiative heating

component was measured via a radiometer (MEDTHERM, Model 22160-22KS-1.410). Figure 4.1 shows the backshell instrumentation and compares the flight data to the NASA simulations [16]. The simulated radiative heat flux (shown in Fig. 4.1) is generally well

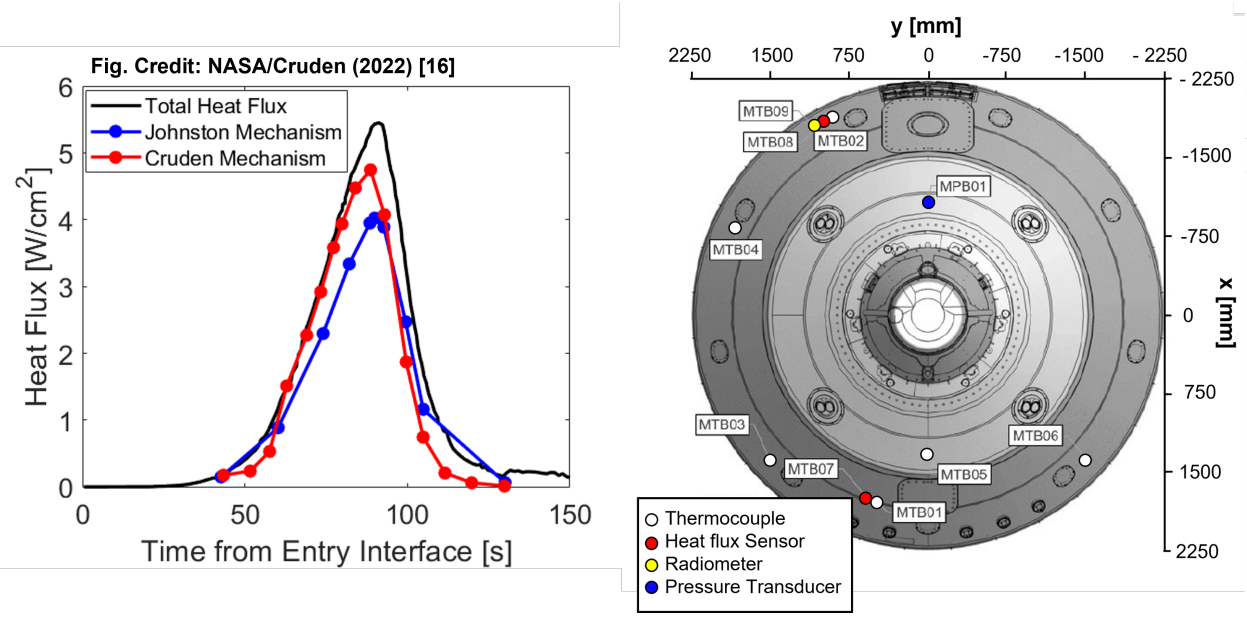

Figure 4.1: (left) MEDLI2 flight data (total heat flux) compared to the radiative heat flux predicted by the Cruden [18] and Johnston [37] mechanisms at different points during entry. (right) Backshell measurement locations of the MEDLI2 sensor suite. Figure reproduced from [16, 57, 86, 99].

captured by the NASA Cruden and Johnston models [18, 37], with under prediction at the peak. Some under prediction at the peak is expected, as the total heat flux is measured and the models have computed the radiative component. As the data shows, convective heating is small at the MTB08/MTB09 position on the backshell. Interestingly, the Cruden mechanism matches the flight data well at early test times, and the Johnston mechanism performs better at later test times.

A test series (64A) at the Electric Arc Shock Tube (EAST) facility at NASA Ames was conducted to investigate the rate models at the Mars2020 conditions experienced by the MEDLI2 sensor in order to reduce uncertainties in the models. For that purpose, the EAST facility was equipped with several mid-infrared lasers for absorption spectroscopy measure-

ments of temperature, CO, and CO_2 [35, 36]. In parallel, multiple spectrometers recorded plasma emission for additional measurements of temperature and number density. This work presents the laser absorption spectroscopy (LAS) results whereas a companion paper [90] details the optical emission spectroscopy (OES) results and compares the two techniques.

4.2 Methods and Theory

In this study, ϕ_j is resolved via scanned-wavelength laser absorption spectroscopy to infer temperatures and number density of CO_2 and CO from spectrally-resolved light attenuation in the mid-wave infrared. There are two methods used to fit the measured absorbance spectrum: 1) A simulated spectrum can be fit over the entire range allowing temperature, number density, and line-specific collision width to float. 2) Each individual lineshape (ϕ_j) can be fit assuming a Voigt profile, without enforcing a single temperature or number density over all the features. Through analysis of the resulting absorbance area ratios, a temperature and number density can be determined. Method 2 can be advantageous if features are influenced by non-ideal effects such as a cool boundary layer, however there is a trade off when features become blended. Often this requires sequential fitting of the spectrum and this increases algorithmic complexity. The fitting routine employed in this work uses a step weight function, defined in Eq. 4.1. This weighting ensures that features of different amplitude equally contribute to the spectral fitting - see for instance the $\nu_3(00^00)$ R(58) and the $\nu_3(01^10)$ R(140) features in Fig. 4.2.

$$W_j = \frac{3}{\alpha_{max,j}} \tag{4.1}$$

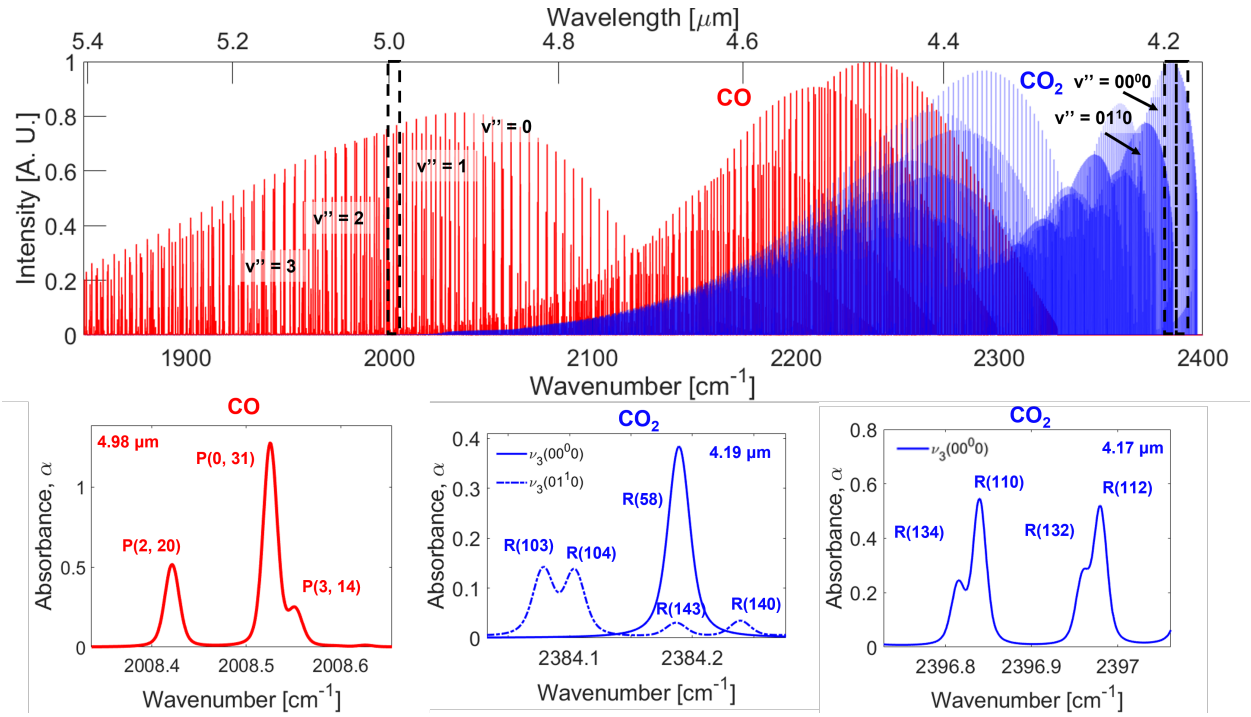

Figure 4.2: Line survey of the fundamental bands of CO and the asymmetric stretch fundamental bands of CO_2 from 4.2 - 5.4 μm (top) Simulated spectrum of resolved transitions of CO (bottom left), and CO_2 (bottom middle and bottom right) using the HITEMP database [75]. Vibrational lower state of CO_2 is denoted with the solid/dashed lines.

4.2.1 Line selection

In this work, a total of twelve spectral transitions (see Table 4.1) are targeted near 4.17, 4.19, and 4.98 µm to resolve temperatures and number densities of both CO_2 and CO. These lines were selected for strong absorbance signals over a wide range of temperatures with sufficient spectral isolation to enable resolution of individual integrated areas, and large energy level spacing making the measurement sensitive to temperature.

The carbon dioxide molecule possesses multiple modes of vibration, complicating the spectrum. The fundamental vibrational frequencies of CO_2 are: symmetric stretch (ν_1, 1334 cm^{-1}), doubly degenerate bending (ν_2, 667 cm^{-1}), and asymmetric stretch (ν_3, 2349 cm^{-1}). In this study, the CO_2 spectra are from the strong absorption region near 4.3 µm which

corresponds to the fundamental asymmetric stretch bands (ν_3) where $\Delta v_3 = 1$. The fundamental asymmetric stretch bands can be distinguished by their lower vibrational levels, denoted with vibrational quantum numbers $v_1 v_2^{l_2} v_3$. l_2 characterizes the angular momentum of the molecule. Within the vibrational bands, rotational lines are indicated as X(J") where X is the branch (R, P, or Q) describing an increase, decrease, or no change in rotational quantum number, with J" being the lower state rotational assignment. In this work, we probe two ν_3 fundamental bands, notated as $\nu_3(00^00)$ and $\nu_3(01^10)$, and several rotational lines within the R branch of these bands ranging from J" = 58 to J" = 140. The target absorption transitions of CO_2 are shown in Fig. 4.2. The two bands utilized in this study are distinguished by lower vibrational energy level of the bending mode, (differentiated by colors in Fig. 4.2: black for the ground state, 00^00, and red for the first excited bending mode, 01^10) as both bands originate from the ground vibrational state of the symmetric ($v_1 = 0$) and asymmetric ($v_3 = 0$) stretch. The $\nu_3(00^00)$ R(58) line and the $\nu_3(01^10)$ R(103), R(104), and R(140) transitions are targeted for measurement by an interband cascade laser (ICL) at 4.19 µm. A second ICL is used at 4.17 µm to probe the $\nu_3(00^00)$ R(110), R(112), R(132), and R(134) features. This multi-laser sensing strategy improves the confidence in the temperature and CO_2 number density measurement. The CO_2 temperature sensitivity is mainly driven by the line pair of $\nu_3(00^00)$ R(58) and the $\nu_3(01^10)$ R(140) features whose maximum energy difference is $\Delta E'' = 7004$ cm^{-1}. At some low temperature conditions the $\nu_3(00^00)$ R(58) is optically thick, when this occurs the temperature sensitivity is mainly driven by the $\nu_3(01^10)$ R(103) and $\nu_3(01^10)$ R(140) line pair with $\Delta E'' = 3502$ cm^{-1}.

For CO, the line identifier B(v'',J'') indicates the branch (R or P) and lower state vibrational and rotational quantum numbers. As shown in Fig. 4.2 (bottom left), the P(2, 20), P(0, 31), and P(3, 14) lines are targeted for measurement. This line selection has been used in previous work and demonstrated high sensitivity to number density and temperature [35, 36].

Table 4.1: Rotational and vibrational lower state energies of transitions probed in this work. $E''_{total} = E''_{vib} + E''_{rot}$. Linecenter and energies are given in wavenumber [cm^{-1}].

Molecule	Linecenter	Line Label	E''_{vib}	E''_{rot}	E''_{total}
CO	2008.42	P(2, 20)	4260	792	5052
CO	2008.53	P(0, 31)	0	1901	1901
CO	2008.55	P(3, 14)	6350	392	6742
CO_2	2384.08	$\nu_3(01^10)$ R(103)	667	4169	4836
CO_2	2384.10	$\nu_3(01^10)$ R(104)	667	4257	4924
CO_2	2384.19	$\nu_3(01^10)$ R(143)	667	7987	8654
CO_2	2384.19	$\nu_3(00^00)$ R(58)	0	1334	1334
CO_2	2384.24	$\nu_3(01^10)$ R(140)	667	7671	8338
CO_2	2396.81	$\nu_3(00^00)$ R(134)	0	7015	7015
CO_2	2396.84	$\nu_3(00^00)$ R(110)	0	4745	4745
CO_2	2396.96	$\nu_3(00^00)$ R(132)	0	6810	6810
CO_2	2396.98	$\nu_3(00^00)$ R(112)	0	4917	4917

4.2.2 Experimental Setup and Test Conditions

To resolve the spectral features described above in Sec. 4.2.1, two beam paths are utilized with three lasers as shown in Fig. 4.3. Two NanoPlus interband cascade lasers (ICLs) were utilized near 4.19 and 4.17 µm to measure CO_2 and one Alpes quantum cascade laser was utilized near 4.98 µm to measure CO. The light is focused into InF_3 single mode fibers and mounted directly to EAST. The light is collimated upon exiting the fiber and pitched across the shock tube's 4-inch pathlength (= 10.16 cm). High bandwidth (∼200 MHz) photovoltaic Vigo detectors are mounted approximately 4 inches from the optical port and contain an iris, bandpass filter, and focusing lens to cut emission, maximize signal, and minimize beam steering. For shock velocities above ∼ 2.7 km/s, the temperature is high enough to dissociate CO_2 and form CO in sufficient quantities to be detected. In these cases, the 4.17-µm ICL laser used for CO_2 is replaced by a quantum cascade laser (QCL) scanning at 2008 cm^{-1} (= 4.98 µm) to monitor CO formation.

The EAST facility at NASA Ames was used to generate the conditions of interest for this study. This facility is well documented in literature [15] and is briefly described in Sec. 2.2.

A 1.25 MJ capacitor bank supplies energy for the electric arc driver. The facility is capable of generating incident shock velocities up to 46 km/s through the 30-foot driven section though in this study the shock velocities ranged from 1.30 - 3.75 km/s. Approximately 50 shocks were conducted using a simulated Mars atmosphere at the time of the Mars2020 entry (95.4% CO_2, 2.6% N_2, 2.0% Ar) [91]. Different fill pressures were used ranging from 0.5 - 2.0 Torr on most test cases.

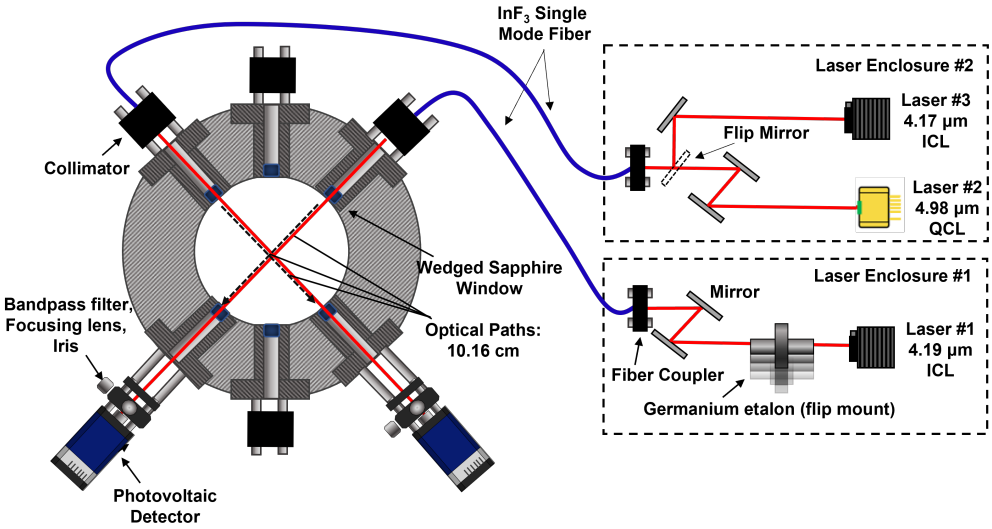

Figure 4.3: Optical setup on the EAST facility. Two laser enclosures contain the free space beam and couple the light into InF_3 single mode fibers. The 4.17-µm ICL laser or the 4.98-µm QCL laser were used depending on the expected shock speed.

4.3 Results

Experiments were conducted to reproduce the Mars2020 shock layer environment near the radiometer and nearby thermal plug location on the TPS. To achieve similarity, three primary fill pressures were used (1.09, 1.49, and 1.99 Torr) and various shock velocities ranging from 1.30 - 3.75 km/s captured multiple points along the flight trajectory. As a result, both chemically frozen and chemically reacting cases were observed. For all but the lowest velocities, vibrational relaxation times predicted by Park [72] and Simpson et al. [79] are

on the order of 1 µs. Therefore, given the temporal resolution of the measurement, a 1 temperature spectrum is valid over almost the entire test time.

4.3.1 Spectrum Fitting Method Results

Absorbance is related to the temperature and number density as described in Sec. 1.5. A single temperature spectrum is fit over the absorbance signals of each molecule independently allowing the temperature, number density and collisional broadening to float. Representative Voigt fits are shown in Figs. 4.4 and 4.5. The states that are probed in this study

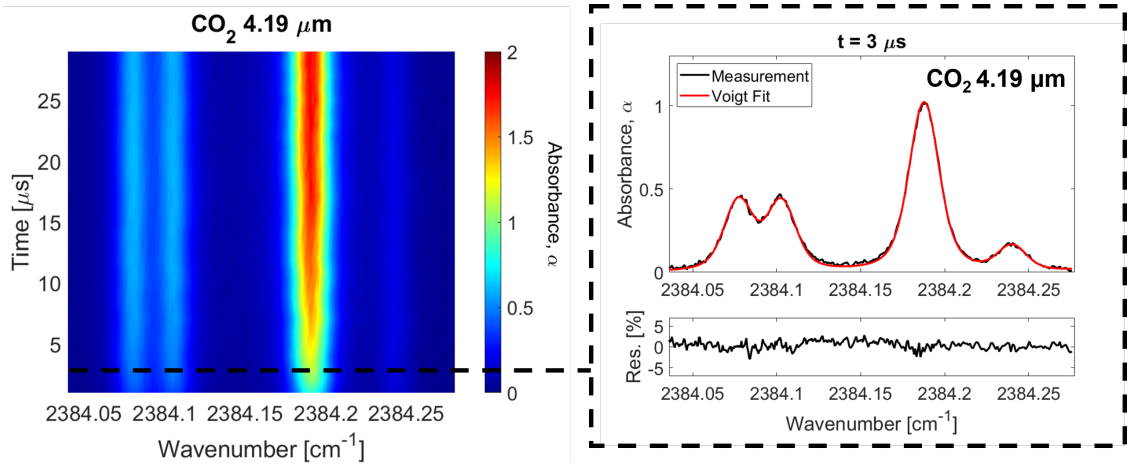

Figure 4.4: (left) Absorbance vs wavenumber and time for CO_2 spectrum at 4.98 µm. (right) Representative Voigt fit of spectrum at t = 3 µs.

become populated very rapidly behind the shock front and this results in high SNR at both wavelengths. The features are well resolved and the Voigt fit shows a low residual indicating it is a good model of the lineshape. Both signals are increasing throughout the test times due to two effects. 1) The CO signal increases primarily as more CO is formed. 2) As the gas cools due to dissociation, the CO_2 signal increases as the low lying states that are resolved in this work become more populated. The transients seen in the absorbance signal imply changing temperature and number density conditions throughout the test.

Key comparisons are made in Figs. 4.6 - 4.8 between the time resolved species and number

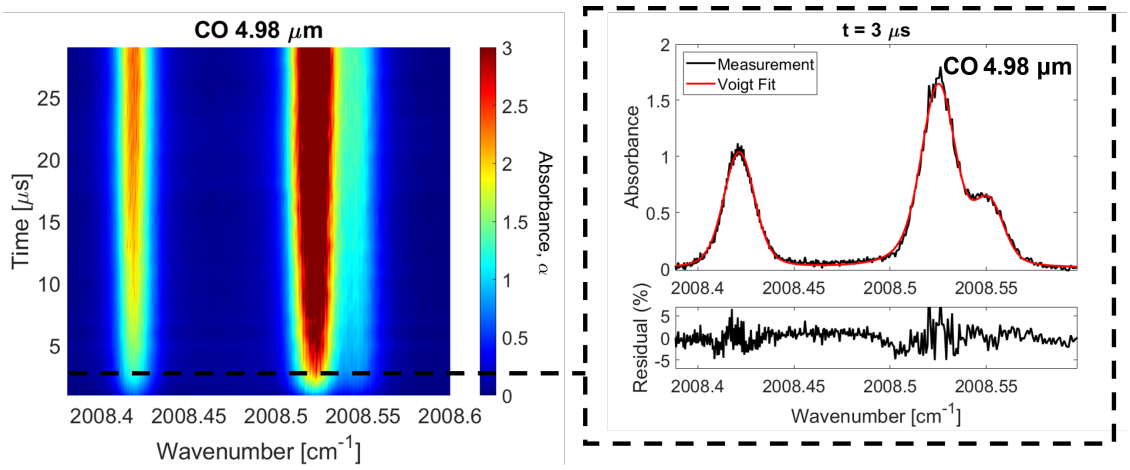

Figure 4.5: (left) Absorbance vs wavenumber and time for CO spectrum at 4.98 µm. (right) Representative Voigt fit of spectrum at t = 3 µs.

densities resolved with LAS and the NASA DPLR CFD code [104]. From shock velocities below 2.7 km/s, CO_2 dissociation is frozen, and thus the simulation is independent of chemical kinetic mechanism used. As velocities increase above 2.7 km/s, dissociation begins to occur within the test time of the incident shock and the CFD simulation becomes sensitive to the chemical rate models employed.

The time resolved measurements generated with the single temperature spectrum fitting method show strong agreement with the simulated temperature and number density across all chemically frozen test cases (see Figs. 4.6 - 4.7). On the time resolved temperature and species plots, number density and temperature in the first 1 - 2 microseconds may be elevated compared to the values measured at t > 2 μs and this is attributed to vibrational relaxation. When this was observed, the measurement resolution (1 µs) is faster than the vibrational relaxation time. In these cases, an alternative fitting routine based on the area ratio of two absorption features sensitive to rotational temperature was utilized to determine T_{rot}. The vibrational temperature is simultaneously deduced based on conservation of enthalpy (assuming $T_{rot} \neq T_{ss} = T_{bend} = T_{as}$). Lastly, the 1.99 Torr test cases produced a more optically thick spectrum than other fill pressures. Neglecting absorbance $\alpha > 3.0$ in the fit, the temperature measurement showed good agreement with the simulated temperature,

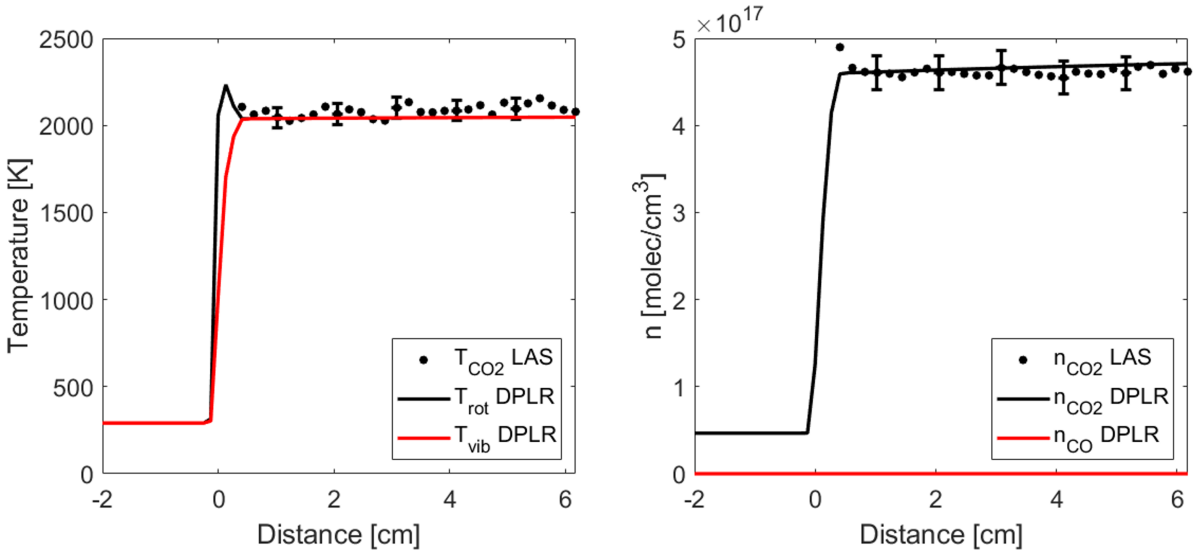

Figure 4.6: Temperature (left) and number density (right) measured and simulated vs distance for a shock velocity of 2.06 km/s 1.49 Torr fill pressure. Estimated δT $\sim$ 2.8 %, and δn $\sim$ 6.0%.

however the number density of CO_2 is about 5 - 10% below that predicted. This discrepancy is attributed to the optical thickness. In Section 4.3.3, a rotational temperature fitting method neglecting the optically thick $\nu_3(00^00)$ R(58) feature is applied to the 1.99-Torr fill cases and reduces the gap between the simulations and measurements in number density.

Figures 4.6 - 4.7 are typical of the majority of 1.09 Torr and 1.49 Torr fill pressure test cases with velocities below $\sim$2.7 km/s. Strong agreement is seen between the measured temperature and measured number density and the simulation. Figure 4.8 shows the typical inferred LAS temperature and number density trends of the higher velocity (>2.7 km/s) test cases. Independently measured temperature between CO_2 and CO is found to be in agreement and follow the DPLR Johnston [37] model. Additionally, the measured number density of CO_2 slightly decreases over the test time and is seen to be below the number densities predicted from both the Cruden [14] and Johnston models [37]. This difference can be attributed to the formation of a boundary layer and detailed analysis is presented in Sec. 4.3.2.

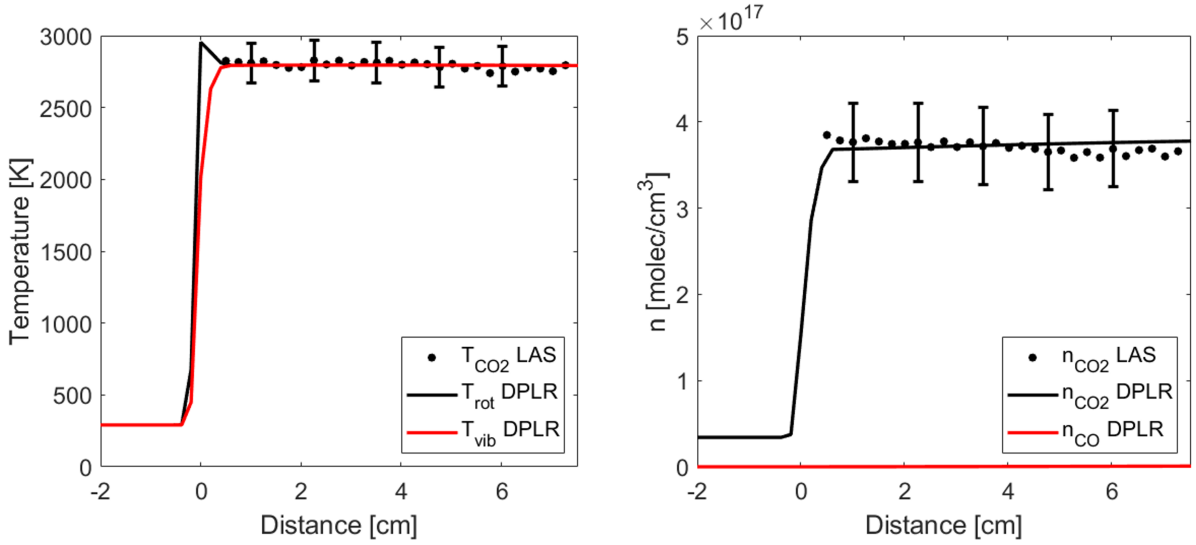

Figure 4.7: Temperature (left) and number density (right) measured and simulated vs distance for a shock velocity of 2.51 km/s, 1.09 Torr fill pressure. Estimated δT $\sim$ 5.0 %, and δn $\sim$ 12.0%.

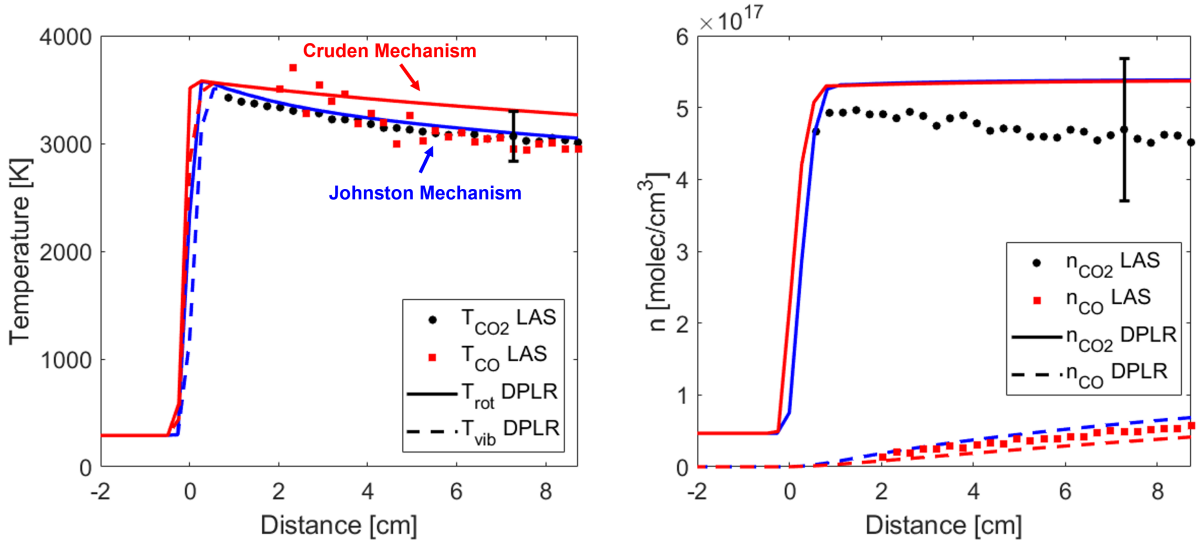

Figure 4.8: Temperature (left) and number density (right) measured and simulated vs distance for a shock velocity of 2.91 km/s, 1.49 Torr fill pressure. Estimated δT $\sim$ 7.5 %, and δn $\sim$ 21.1%. Results have not been corrected for boundary layer absorption.

The CO number density results are highlighted in Fig. 4.9, and resolve a clear trend with lower shock velocities producing less CO. The yield of CO is determined via fitting an exponential curve (Eq. 4.2) to the CO number density and is compared to the Johnston [37]

and Cruden [18] kinetic models implemented in DPLR.

$$n(t) = n_{eq}\left[1 - \exp\left(\frac{-t}{\tau}\right)\right] \tag{4.2}$$

The CO measurements are found to be in close agreement with the DPLR prediction, lying mostly along the Johnston [37] model and then in between the Cruden [18] and Johnston [37] models at higher velocities.

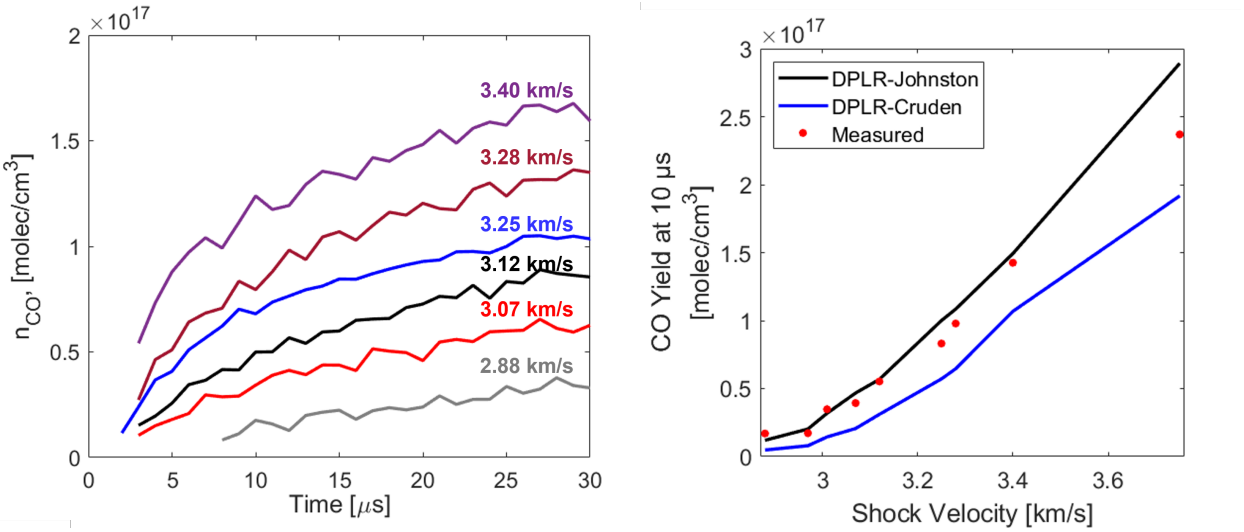

Figure 4.9: (left) Measured CO number density with time for 1 Torr test cases. (right) CO yield at 10 µs from measurement and simulations vs shock velocity.

Figure 4.10 compares the average temperature predicted from the DPLR simulations [37, 18] to the average temperature measured for the range of shock velocities covered in this test series. On a majority of the test cases, temperature is within 5% of the Johnston model. Number density measurements are typically within 10% of the model at velocities below 2.7 km/s, and then are systematically lower by 10 - 20%. This is attributed to the boundary layer (see Sec. 4.3.2). Additionally, two tests were performed at fill pressures of 9 Torr, to investigate CO formation at low velocity, but none was observed at 4.98 µm. CO_2 at 4.19 µm on these tests was optically thick precluding a measurement with this sensor at this condition.

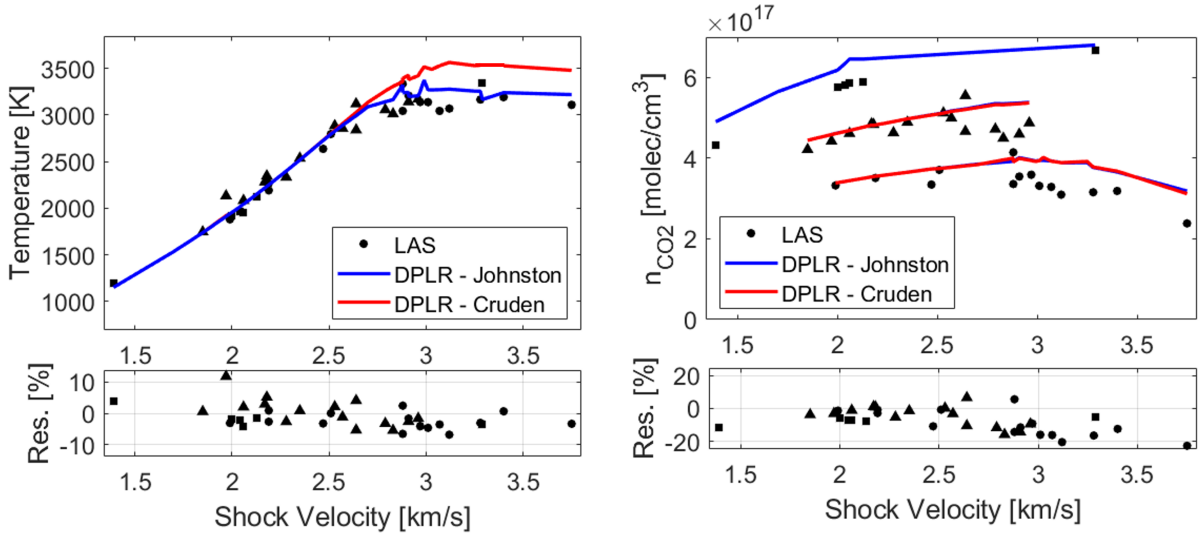

Figure 4.10: CO_2 shock summary showing the average measured temperature and number density with the simulation, vs shock velocity. Residual is calculated against the Johnston mechanism [37]. Squares, triangles, and circles denote a fill pressure of 1.99, 1.49, and 1.09 Torr respectively.

4.3.2 Boundary Layer Analysis

The discrepancy observed at high velocities between the number density of CO_2 inferred from absorption and the simulated number density was investigated and can be attributed to a thin boundary layer behind the shock wave. The following analysis is conducted to estimate the boundary layer and show its effect on inferred temperature and number density over a range of conditions. The compressible boundary layer in a shock tube is well described by Mirels theory [61] and the governing equations are shown in Eqs. 4.3 - 4.6.

$$\frac{\partial(\rho u)}{\partial x} + \frac{\partial(\rho v)}{\partial y} = 0 \qquad \text{(Mass)} \tag{4.3}$$

$$\rho\left(u\frac{\partial u}{\partial x} + v\frac{\partial u}{\partial y}\right) = -\frac{\partial p}{\partial x} + \frac{\partial}{\partial y}\left(\mu\frac{\partial u}{\partial y}\right) \qquad \text{(x - momentum)} \tag{4.4}$$

$$\frac{\partial p}{\partial y} = 0 \qquad \text{(y - momentum)} \tag{4.5}$$

$$\rho c_p \left(u\frac{\partial T}{\partial x} + v\frac{\partial T}{\partial y} \right) = -u\frac{\partial p}{\partial x} + \frac{\partial}{\partial y}\left(k\frac{\partial T}{\partial y} \right) + \mu \left(\frac{\partial u}{\partial y} \right)^2 \qquad \text{(Energy)} \tag{4.6}$$

ρ is the density, u and v are the velocity in the flow (x) and wall normal (y) directions, p is the pressure, T is the temperature, μ is the dynamic viscosity, c_p is the specific heat at constant pressure, and k is the thermal conductivity of the gas. Dynamic viscosity and thermal conductivity are calculated at elevated temperatures via Sutherland's law [98] as shown in Eqs. 4.7 and 4.8.

$$\frac{\mu}{\mu_0} = \left(\frac{T}{T_0} \right)^{\frac{3}{2}} \frac{T_0 + S_\mu}{T + S_\mu} \tag{4.7}$$

$$\frac{k}{k_0} = \left(\frac{T}{T_0} \right)^{\frac{3}{2}} \frac{T_0 + S_k}{T + S_k} \tag{4.8}$$

Sutherland's law is based on kinetic theory, and has been shown to be accurate over a wide range of temperatures for air and is commonly used in hypersonics CFD programs. For the simulation of the compressible boundary layer in this study, the gas viscosity is assumed to be that of CO_2, as it is the major constituent (95.4%) of the mixture. Table 1-2 and 1-3 of [98] list the viscosity of CO_2 as 1.370×10^{-5} [(N·s)/m^2] and thermal conductivity of CO_2 as 0.0146 [W/(m·K)] at the reference temperature of 273 K. Additionally, the Sutherland constants for CO_2 are listed as $S_\mu = 222$ K and $S_k = 1800$ K.

Mirels provides a similarity variable, η, for solving the compressible boundary layer equations

as shown in Eq. 4.9.

$$\eta = \sqrt{\frac{1}{2}\frac{u_e \rho_e}{x \mu_e}} \int_0^y \frac{T_e}{T} dy \tag{4.9}$$

In shock fixed coordinates, the boundary conditions of Mirels are shown in Eq. 4.10 - 4.14.

$$u(x,0) = -U_{is} \tag{4.10}$$

$$v(x,0) = 0 \tag{4.11}$$

$$T(x,0) = T_w \tag{4.12}$$

$$u(x,\infty) = u_2 \tag{4.13}$$

$$T(x,\infty) = T_e \tag{4.14}$$

The velocity in the x direction at the wall is determined from the no-slip condition. The y velocity at the wall is zero. The wall temperature is held fixed, and the freestream temperature and velocity determined from the normal shock relations are enforced at $\eta = \infty$.

There are multiple ways to numerically solve this system of equations using modern methods. For this study, the solution method of Oz et al. [67] for the compressible boundary layer of air over a flat plate was combined with Mirel's theory to estimate the compressible boundary layer properties behind a stationary shock wave in a CO_2 test gas. The code is presented in Appendix A. A 4th order Runge-Kutta method is utilized with a shooting method to close the system of equations and allow a numerical solution. The freestream velocity and temperature ($\eta = \infty$) are used as the convergence criteria. Once the similarity solution is

obtained, Eq. 4.15 is applied to transform the η back to x and y coordinates.

$$y\sqrt{\frac{1}{2}\frac{u_e\rho_e}{x\mu_e}} = \int_0^\eta \frac{T}{T_e}d\eta \tag{4.15}$$

A typical boundary layer temperature profile is presented in Fig. 4.11. The temperature trends from the wall temperature ($\sim$ 297 K) to the core flow temperature (2000 – 3500 K) within the boundary layer thickness (see the δ_{99} curve in Fig. 4.11). Additionally, the number density is inversely related to the temperature profile, resulting in approximately ten times more CO_2 near the wall than in the freestream (core) flow. This boundary layer code was found to be within 10% of the boundary layer estimated in the LASTA code [76] (when comparing up to 10 cm behind the shock front) which utilizes a slightly different approach in the estimation of the boundary layer though still based on Mirels Theory.

The absorbance signal of the boundary layer can be estimated at the measured locations behind the incident shock wave now that the size (pathlength), temperature, and density of the region is characterized. This simulated boundary layer absorbance is then subtracted from the line of sight (LOS) measurement as shown in 4.11 and is refit to estimate a new temperature and number density of CO_2. It is seen that the cool boundary layer affects the $\nu_3(00^00)$ R(58) feature significantly more than the $\nu_3(01^10)$ R(103), R(104), and R(140) features. This is highlighted in Fig. 4.12 which shows the simulated area difference [%] of three spectral features as a function of temperature outside the boundary layer. This is due to the temperature dependent linestrength curve, as low temperature CO_2 does not produce a strong spectral signal in the $\nu_3(01^10)$ R(103), R(104), and R(140) features.

As can be clearly seen, the temperature of CO_2 increases as well as the CO_2 number density when accounting for the boundary layer in this high temperature case. The low velocity, chemically frozen result is minimally affected by the boundary layer as the $\nu_3(00^00)$ R(58) feature is optically thick and remains above the absorbance cutoff limit in the fit upon sub-

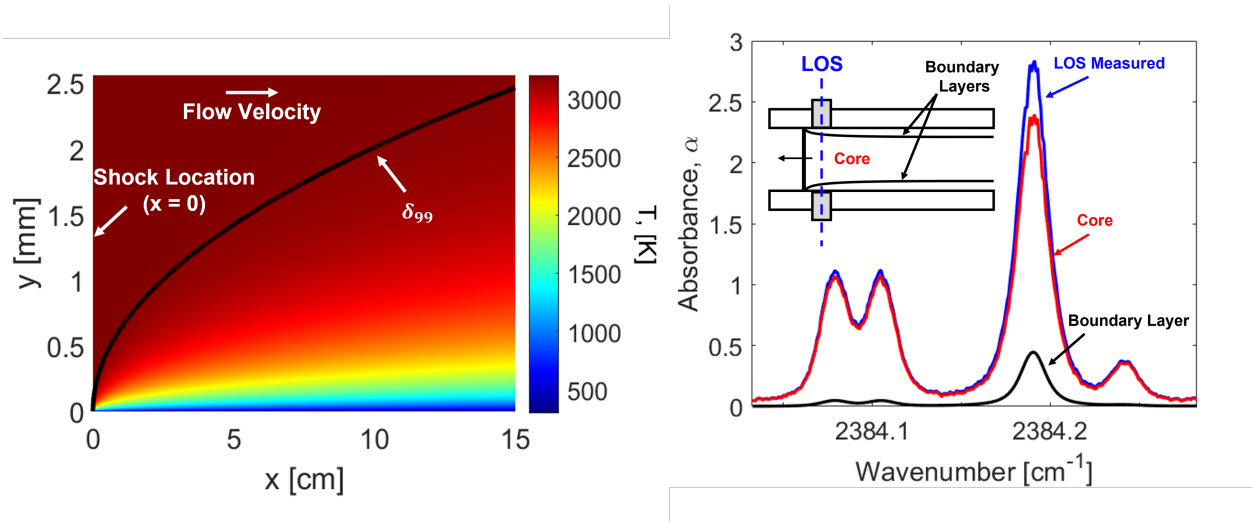

Figure 4.11: (left) Simulated compressible boundary layer temperature profile. The shock location, δ_{99} thickness and freestream flow direction are highlighted. The no slip condition is enforced at the wall (y = 0). (right) Absorbance signals from the line of sight (blue), core (red), and boundary layer (black) estimated from a similarity solution of the boundary layer profile.

traction of the simulated boundary layer. In summary, the $\nu_3(00^00)$ R(58) absorbance

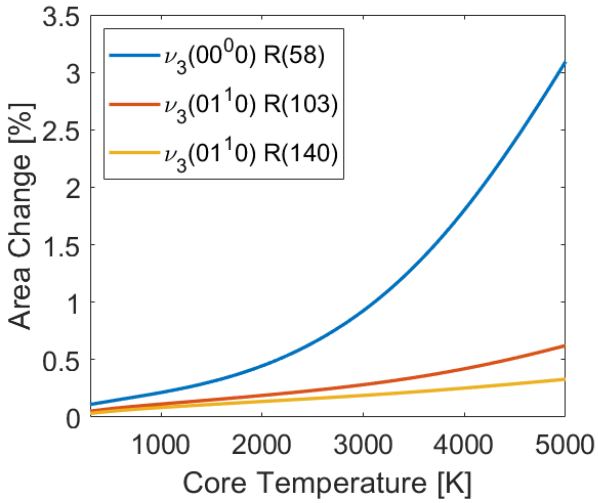

Figure 4.12: Line area change due to the boundary layer. The higher energy states are less sensitive to the boundary layer.

signal has been shown to be sensitive to a boundary layer affecting ~2% of the 10.16 cm total pathlength. Accounting for a simulated laminar boundary layer increases the LAS CO_2 temperature typically less than 5% and increases the inferred number density by approxi-

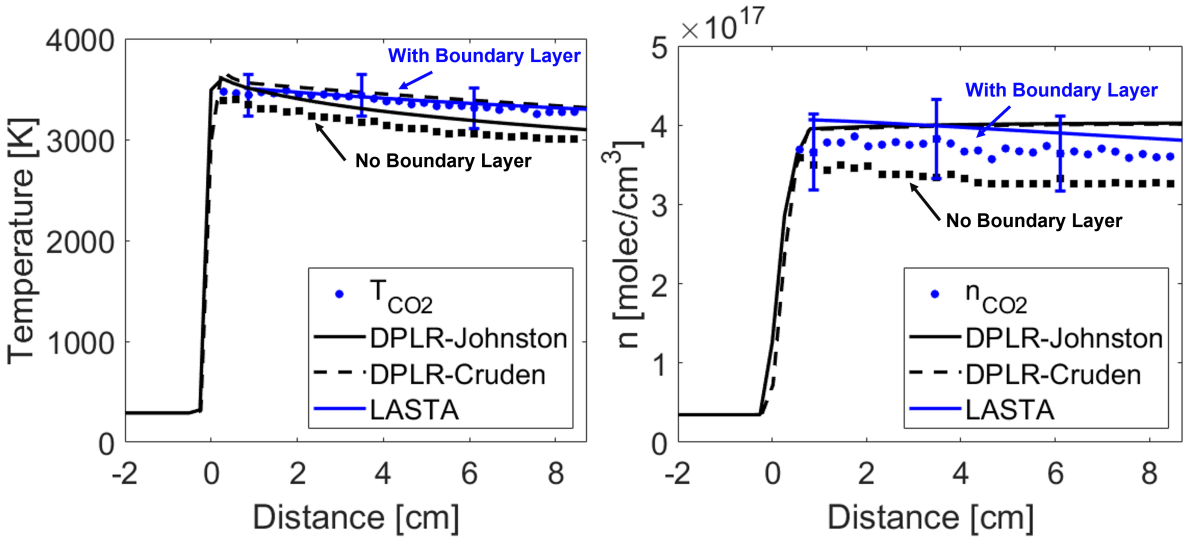

Figure 4.13: (left) Temperature and (right) number density vs distance behind shock estimated with LOS absorbance spectrum (black) and estimated with a simulated boundary layer profile (blue). Data is compared with the Cruden [18] and Johnston [37] mechanisms simulated in DPLR [104] and LASTA [76].

mately 10% (see Fig. 4.13). Importantly, this explains much of the discrepancy in number density measurement in the reacting regime, and also alters the interpretation of the rate chemistry based upon the temperature trend.

4.3.3 Multi-temperature area fitting method

An alternative method to the single temperature spectrum fitting method is explored in this section to minimize the effect of the boundary layer, and high velocity test case results are found to increase to values closer to the DPLR models. The $\nu_3(00^00)$ R(58) absorbance signal is the primary source of boundary layer induced bias in the measurement (see Fig. 4.12). A rotational temperature of CO_2 can be determined from the spectra via the area ratio between the $\nu_3(01^10)$ R(103) and the $\nu_3(01^10)$ R(140) signals, and as Fig. 4.12 shows, should be more robust to boundary layer effects. This method was previously utilized by Jelloian et al. [36] to measure CO_2 rotational temperatures in vibrationally relaxing mixtures. The reader is referred to [36] for details on fitting method, sensitivity, and uncertainty analysis

using this technique.

The measured rotational temperature can be used on chemically frozen cases to infer vibrational temperature through the conservation of stagnation enthalpy shown in Eq. 4.16. $h_{0,1}$ and $h_{0,2}$ are the stagnation enthalpy [J/kg] before and after the shock passes.

$$h_{0,1} = h_{0,2} = h_f^o + C_{p,tr-rot}(T_{rot} - T_{ref}) + h_{vib}(T_{vib}) - h_{vib}(T_{ref}) + \frac{u_2^2}{2} \tag{4.16}$$

h_f^o is the enthalpy of formation [J/kg], $C_{p,tr-rot}$ is the heat capacity at constant pressure [J/(kg·K)], h_{vib} [J/kg] is the enthalpy contribution from the vibrational energy, and u_2 [m/s] is the flow velocity behind the incident shock in the shock fixed frame of reference. Note the flow velocity (u_2) changes during vibrational relaxation by approximately 300 m/s on a majority of the test cases, however this is only attributable to about 3% of the total enthalpy of the flow. Therefore for this analysis, the vibrationally equilibrated flow velocity is used throughout the test. To calculate $C_{p,tr-rot}$ an expression is given in Eq. 4.17 which assumes the translational and rotational energy mode are equilibrated ($T_{tr} = T_{rot}$) and fully excited.

$$C_{p,tr-rot} = R + \frac{3}{2}R + \frac{D_{rot}}{2}R \tag{4.17}$$

R is the gas constant, and D_{rot} is the rotational degrees of freedom (for linear molecules such as CO_2, $D_{rot} = 2$). Utilizing Eqs. 4.16 and 4.17, the vibrational temperature can be determined on chemically frozen test cases.

Vibrational relaxation was observed on a few low velocity test cases and multi-temperature measurements are presented in Figs. 4.14 and 4.15. Figure 4.14 shows clear trends from near the vibrationally frozen temperature ($\sim$ 3000 K) to the vibrationally equilibrated temperature ($\sim$ 1880 K). The estimated uncertainty in T_{rot} at this shock velocity is 4.3 %. On many test cases, the vibrational relaxation times measured are slightly longer than the model

employed in the DPLR code [104]. As velocities increase and the gas begins to dissociate, the relaxation times decrease to < 1 μs and a single temperature is assumed over all energy modes of CO_2.

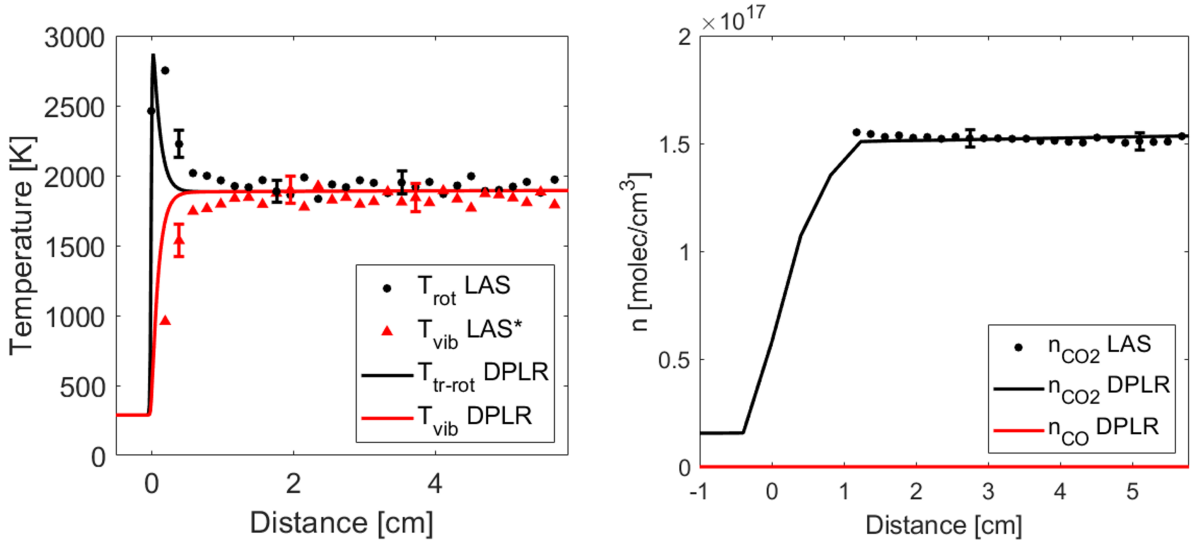

Figure 4.14: Time resolved rotational and vibrational temperature (left) and number density (right) for a 1.96 km/s shock with 0.49 Torr fill pressure. The vibrational temperature is determined from conservation of enthalpy assuming $T_{tr} = T_{rot}$.

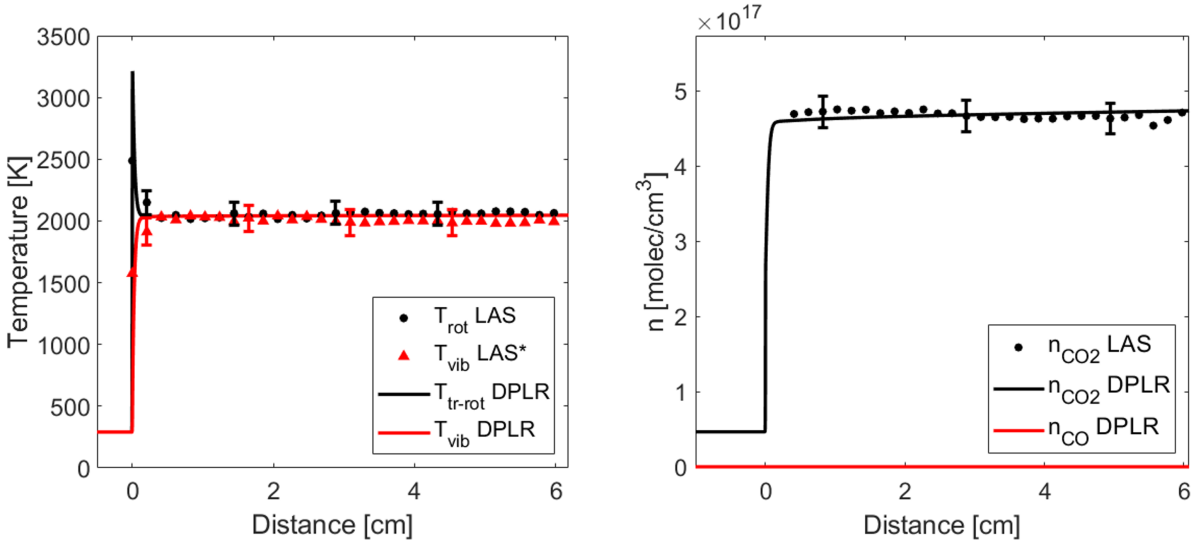

Figure 4.15: Time resolved rotational and vibrational temperature (left) and number density (right) for a 2.06 km/s shock with 1.49 Torr fill pressure. The vibrational temperature is determined from conservation of enthalpy assuming $T_{tr} = T_{rot}$.

The differences between measured LAS inferred properties (T and n_{CO_2}) and the DPLR

model predictions on chemically reacting test cases have been decreased using the area ratio method with a simulated boundary layer (Figs. 4.16 - 4.18). It is observed that the temperature results determined with the area ratio plus boundary layer method have slightly increased the temperature measurement (<5%) and more significantly increased the number density measurement of CO_2 (<10%) with the high velocity cases showing the most significant change. Additionally, in order to measure a rotational temperature, the $\nu_3(01^10)$ R(140) feature must have sufficient signal. On the two lowest velocity test cases (1.30 and 1.39 km/s) , the $\nu_3(01^10)$ R(140) feature was not sufficiently resolved and thus this area ratio method cannot be used. The new fitting method results are summarized in Fig. 4.18. Overall, good agreement is still found with the Johnston [37] mechanism, although a number of tests yield data that lies between the Johnston and Cruden mechanisms at the highest shock velocities. At velocities > 3.1 km/s, the measured number density of CO_2 is lower than any model, however the residuals between model and measurement are decreased relative to Fig. 4.10.

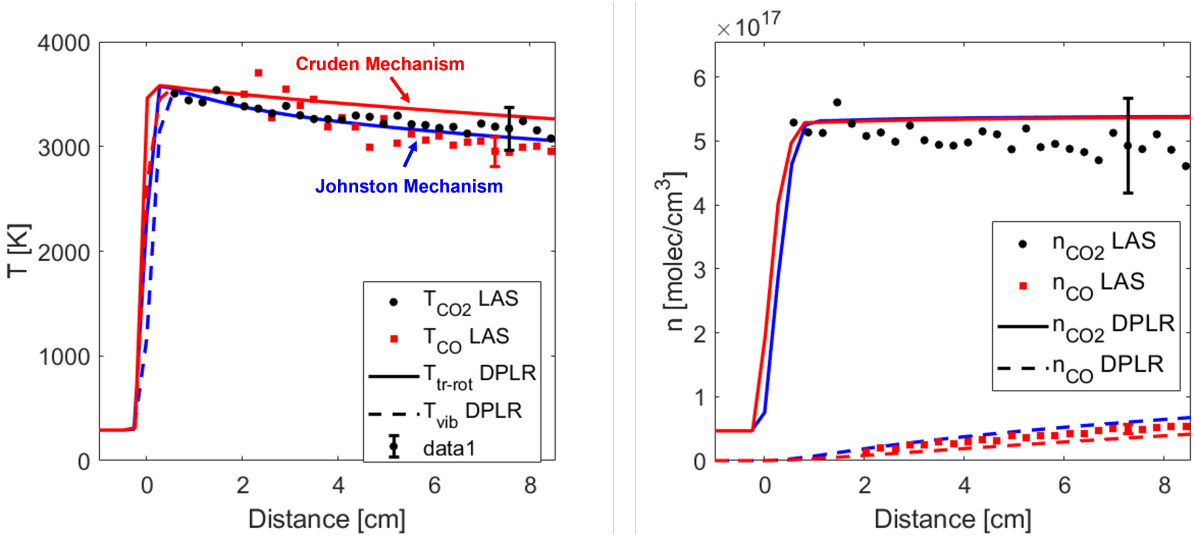

Figure 4.16: Spatially resolved rotational temperature (left) and number density (right) for a 2.91 km/s shock with 1.49 Torr fill pressure. Boundary layer correction applied to CO_2.

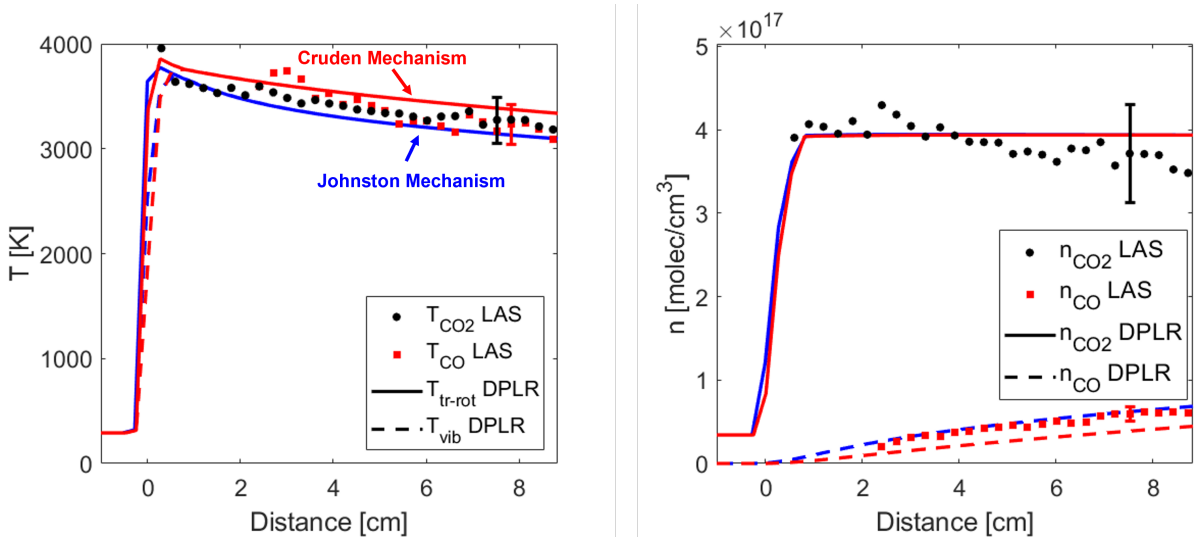

Figure 4.17: Spatially resolved rotational temperature (left) and number density (right) for a 3.01 km/s shock with 1.09 Torr fill pressure. Boundary layer correction applied to CO_2.

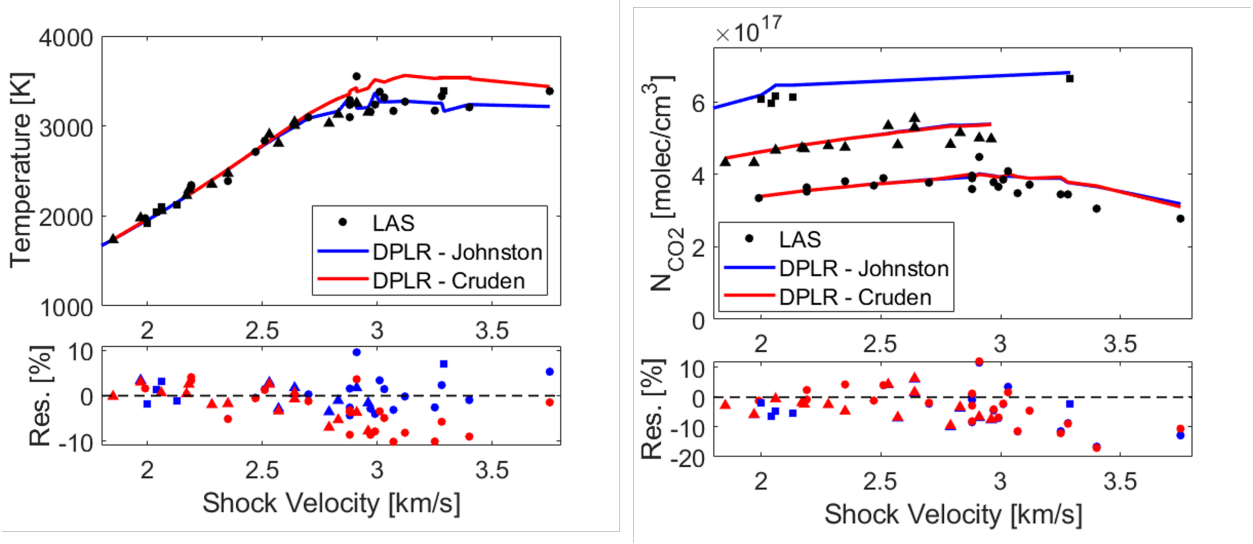

Figure 4.18: Measured temperature (left) and CO_2 number density (right) vs shock velocity. Data is compared with the Cruden [18] and Johnston [37] mechanisms simulated in DPLR [104]. Squares, triangles, and circles denote a fill pressure of 1.99, 1.49, and 1.09 Torr respectively.

4.4 Conclusions

A mid-infrared laser absorption diagnostic has yielded quantitative measurements of temperature and number density of CO_2 and CO at shock conditions relevant to the MEDLI2 heat

flux data [16, 57, 86] captured during the Mars2020 EDL. Initially, the spectrum was fit with a one temperature model and was found to be sensitive to a thin (1 – 2 mm) boundary layer at shock velocities above 2.7 km/s. The spectra were re-fit using a simulated boundary layer and methods that isolate the energy modes as developed in [36]. The resulting temperature and number density plots were found to be more robust to the boundary layer effect (up to velocities ∼3.1 km/s) and yield results closer to the DPLR models (typically within 5% for temperature and 10% for number density).

Independent spectral fitting over CO_2 and CO has yielded similar temperature results typically within 5% of the estimated temperature from simulation. A slight decrease is observed on the number density of CO_2 that is not captured in the DPLR model. This is likely due to an adverse pressure gradient in the simulation while the shock tube has a decreasing pressure gradient behind the shock wave. Multi-temperature measurements were made at low velocities and relaxation times were found to be slightly longer than those predicted by the DPLR model [104].

In summary, the LAS sensor and method described above have been used in tandem with optical emission spectroscopy (OES) to measure a recreated Mars entry shock layer to further the investigation of the MEDLI2 flight data and increase the science return of the Mars2020 mission. The emission data is the subject of a companion paper [90], however, the resulting trends in inferred temperature and number density from OES and LAS largely agree within their respective uncertainties. Further experimental studies of the boundary layer size are warranted to assess the accuracy of the simulations and assumptions utilized in this work, though these simulations have shown good agreement with an independent code (LASTA [76]) and successfully explain a gap between the LAS measurements and models on reacting test cases. CO_2 non-equilibrium kinetics are complex, and the data produced in this work and [90] can be used to refine and tune the rate models utilized in this environment.

4.5 Uncertainty Analysis

Uncertainty analysis is conducted to quantify the uncertainty in temperature and number density on CO_2. This section describes the uncertainty analysis based on the Taylor series method of error propagation which assumes uncorrelated sources of error [6]. The following expressions are well detailed and derived in the appendix of Minesi et al. [60]. The non-dimensional uncertainty of a dependent variable r (δr/r) can be calculated from the uncertainty in the independent variables ($\delta \mathrm{x}_i$) used to calculate r as shown in Eq. 4.18.

$$\left(\frac{\delta r}{r}\right)^2 = \sum_i \left(\frac{\partial r}{\partial x_i}\frac{\delta x_i}{x_i}\frac{x_i}{r}\right)^2 \tag{4.18}$$

Rotational temperature uncertainty can be estimated via Eq. 4.19 (see Minesi et al. [60]) since the $\nu_3(01^10)$ R(103) and $\nu_3(01^10)$ R(140) spectral features are within the same vibrational band.

$$\frac{\delta T}{T} = \frac{k_B}{hc}\frac{T}{\Delta E}\sqrt{\sum_{i=1}^{2}\left(\frac{\delta S_i}{S_i}\right)^2 + \left(\frac{\delta A_i}{A_i}\right)^2} \tag{4.19}$$

The uncertainty in absorbance area A can be estimated via Eq. 4.20, where α_{pk} is the peak absorbance of the transition [60].

$$\frac{\delta A}{A} = \frac{1}{SNR}\left(\frac{\exp(\alpha_{pk})}{\alpha_{pk}}\right) \tag{4.20}$$

δS/S is estimated from the uncertainty value in the reference linestrength listed in HITRAN [28] for R(103) and R(104) (2 %) and HITEMP [75] for R(140) (20%), as the R(140) feature is not listed in HITRAN. The number density uncertainty is approximated with the expression

in Eq. 4.22.

$$\left(\frac{\delta n}{n}\right)^2 = \left(\frac{\delta A_i}{A_i}\right)^2 + \left(\frac{\delta S_i}{S_i}\right)^2 \tag{4.21}$$

$$\left(\frac{\delta S_i}{S_i}\right)^2 = \left(\frac{\delta S_i^o}{S_i^o}\right)^2 + \left(\frac{1}{S(T)}\frac{dS}{dT}\delta T\right)^2 \tag{4.22}$$

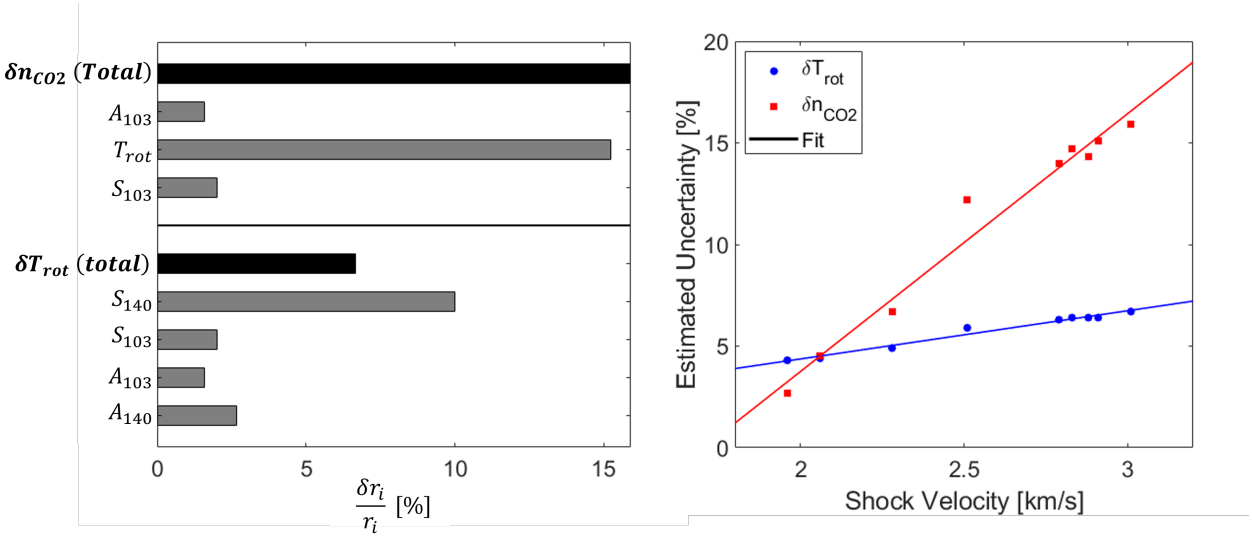

Figure 4.19: Bar chart representing the contribution of uncertainty of each term in Eq. 4.19 (bottom) and 4.22 (top) on a 3.01 km/s test case. (left) Estimated rotational temperature and number density uncertainty vs shock velocity (right). Note a majority of the error comes from the coupling of T and n.

Figure 4.19 highlights the sources of uncertainty considered in the calculation. It is observed that the uncertainty in the ν_3 (01^10) R(140) linestrength is the main contribution to the rotational temperature uncertainty and the linestrength sensitivity to temperature is the main contribution to the number density of CO_2 uncertainty. A subset of tests was analyzed and used to generate the 4.19 (right) figure highlighting the uncertianty trends with shock velocity.

To determine the uncertainty in T_{vib}, the uncertainty in vibrational enthalpy was estimated considering the uncertainty in T_{rot} and the uncertainty in flow velocity in shock fixed coordinates behind the shock front (u_2) as shown in Eqs. 4.23 and 4.24. The uncertainty in u_2 is estimated as 100% based off of the vibrationally frozen and equilibrated values calculated from the normal shock relations solver [10]. The uncertainty in the measured T_{vib} value is mostly a function of the uncertainty in T_{rot}, u_2 minimally affects the overall stagnation enthalpy (typically less than 3%) and thus does not propagate much uncertainty to T_{vib}. The resulting uncertainty in T_{vib} is estimated to be between 5 - 6%.

$$\left(\frac{\delta h_{vib}}{h_{vib}}\right)^2 = \left(\frac{dh_{vib}}{dT_{rot}}\frac{\delta T_{rot}}{T_{rot}}\frac{T_{rot}}{h_{vib}}\right)^2 + \left(\frac{dh_{vib}}{du_2}\frac{\delta u_2}{u_2}\frac{u_2}{h_{vib}}\right)^2 \tag{4.23}$$

$$\left(\frac{\delta T_{vib}}{T_{vib}}\right)^2 = \left(\frac{dT_{vib}}{dh_{vib}}\frac{\delta h_{vib}}{h_{vib}}\frac{h_{vib}}{T_{vib}}\right)^2 \tag{4.24}$$

Chapter 5

Conclusions and Future Research

This project has developed novel laser absorption sensors to experimentally investigate the non-equilibrium kinetic models used for CO_2 and CO planetary entry flows. There have been four major accomplishments during the course of this work: 1) The tunability of the ICL and QCL lasers employed in this study was increased from the hundreds of kHz to several MHz by incorporating an RF-diplexer (bias tee) into the control circuit. This enabled the fast vibrational relaxation rates and chemical rates experienced at entry velocities to be investigated in this work and additionally benefited separate studies of rotating detonation engines [63, 62] and CO dissociation near 10,000 K (nearly 1 eV!) [60]. 2) Multi-temperature measurements of CO - Ar mixtures on a high enthalpy shock tube at UCLA were shown to yield quantitative results. Large amounts of CO are formed in the shock layer during Mars entry, as CO_2 dissociates at modest temperatures compared to those often encountered on the fore TPS. It is therefore important to characterize the rates of energy transfer between translation, rotation, and vibration for CO. 3) Vibrational relaxation times of CO_2 and CO_2 - Ar mixtures at temperatures relevant to planetary entry were investigated on the same facility utilizing similar methods to those developed in Ch. 2. CO_2 is the primary species encountered in both the Mars and Venus atmosphere ($\sim$ 95%), and hence its vibrational

excitation and dissociation rates are important to characterize over a range of conditions as it is the rate limiting reaction (reaction 2.1) in this environment. In addition to driving most of the chemistry in the shock layer, there is a significant amount of vibrationally hot CO_2 (2,000 - 3,000 K) found the wake of the entry vehicle, and due to this large volume of gas in the wake with line of sight to the backshell, radiative heating must be considered in the design of the aft TPS. 4) A combined version of the sensors described in Ch. 2 and 3 was deployed on the EAST facility at NASA Ames and has been used to investigate chemical models employed by NASA. In summary, this work has advanced multi-temperature laser absorption spectroscopy techniques and has demonstrated such sensors are capable of resolving fast thermal and chemical non-equilibrium phenomena encountered in entry environments.

5.1 Future Research Directions

This project has aspects of both experimental measurement and simulation. Each of these areas have many avenues of further research.

The shock tube compressible boundary layer simulation can be improved to account for chemical reactions in the boundary layer. This can be investigated with a similarity solution method, or via CFD directly solving the Navier-Stokes equations for a shock tube flow. It may be possible to solve a representative steady (time-invariant) flow, simplifying the computation. The boundary layer can also be experimentally verified with a minimally intrusive optical probe to measure temperature, and number densities with laser absorption. From these measurements a boundary layer thickness can be inferred. Such a probe could also investigate a turbulent shock tube boundary layer using a roughened wall. A comprehensive model of the boundary layer in a shock tube (with its associated uncertainty) would benefit many studies as boundary layer effects are often neglected.

An experimental investigation of the 5 temperature model of CO_2 is warranted where temperatures of translation, rotation, and three vibrational temperatures (symmetric stretch, bending, and asymmetric stretch) are measured and compared to the state to state models of Vargas [92], Kustova [44], and Kosareva [43]. In the work presented in Ch. 3, the areas of the absorbance features are primarily sensitive to the vibrational temperature of the bending mode. One could expand this approach and choose features that are sensitive to the symmetric stretch and asymmetric stretch modes, though the wavelengths will need to increase closer to 4.3 μm where the CO_2 spectrum is increasingly blended.

Further high temperature chemistry can be investigated with similar MHz shock tube laser absorption techniques. The dissociation of CO begins to occur at temperatures above 5000 K, and MHz LAS techniques can be used to resolve the formation. A recent study of Cruden et al. [14] investigated this rate via emssion and concluded that a single rate equation cannot explain the observations across all achieved shock velocities (3.4 - 9.5 km/s). The CO dissociation rate of Johnston [37] performs well above 6.6 km/s, and below 6.6 km/s the rate of Hanson [32] matches the emission measurements best. This suggests the rate can be improved, specifically the temperature dependence of the rate. In addition to high speed Mars entries, CO dissociation plays a role for Venus entry as Venus entry typically occurs at higher velocities.

Other species of interest for planetary entry can be investigated such as CN, NO, electronically excited O, and electrons using similar absorption techniques. CN is an important radiator for the case of Titan entry and can be investigated near 1.1 micron as shown in Fig. 5.1. Smaller amounts of CN form for Venus and Mars entries as well. The $^5S^0$ excited state of atomic oxygen can be investigated at 777.2 nm using the method of Nations et al. [65]. Additionally, electron number density can be investigated utilizing the Stark shift of the line [50]. MHz tuning allows the formation of electronically excited states and the formation of electrons to be better resolved. This can be used to improve the collisional radiative model

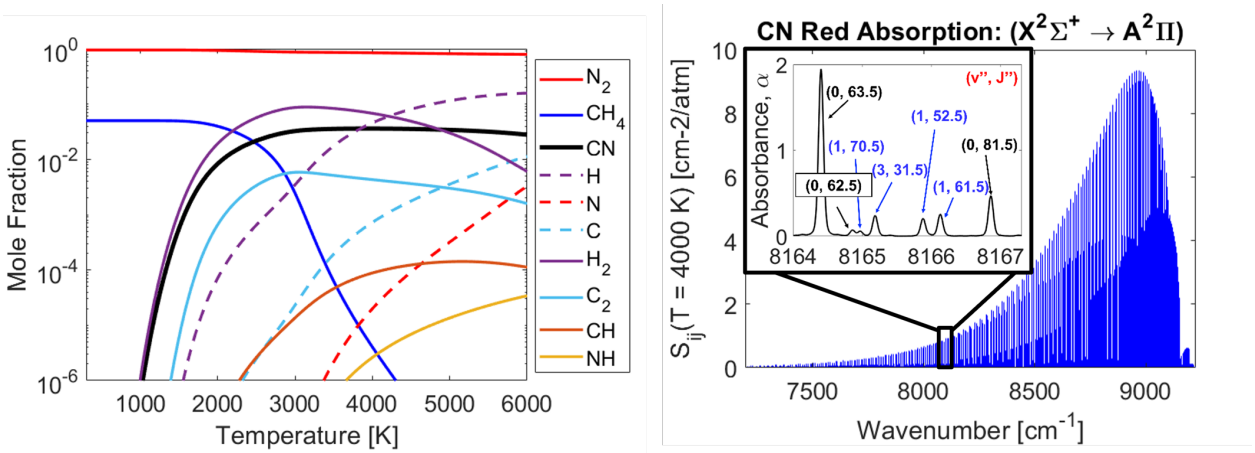

Figure 5.1: Titan atmosphere CEA analysis showing major species (left). CN line survey and simulated spectrum at representative conditions (X_{CN} = 3.5%, T = 4000 K, P = 0.5 atm, L = 10.16 cm) (right). Transitions labeled in blue indicate excited vibrational levels.

in a variety of mixtures pertaining to Earth and Mars entry cases.

High speed shock layer imaging is an additional promising area of research. This method would combine imaging techniques developed by Wei et al. [95] and high speed LAS methods in this work to image the shock layer to an improved spacial resolution (∼100 μm). A laser is used to backlight a camera that will image the shock layer as it passes. By tuning the laser over an absorption feature, the light will attenuate and a species such as CO or NO will be spatially resolved behind the shock front. There are challenges with this method including current bandwidth limitations of mid-IR cameras, nevertheless this area should be investigated. This bandwidth limitation could be overcome if deployed on a steady flow such as an arcjet.

In summary, this effort has expanded the current work in the entry community to study the Mars aerothermal environment. We have achieved high speed (MHz), quantitative, multi-temperature measurements of non-equilibrium CO and CO_2 at conditions relevant to the Mars entry shock layer and backshell. These high speed laser absorption techniques have been employed on other projects as well to investigate chemical phenomena occurring at μs timescales. These measurements can be used to refine and tune the next generation of

thermochemistry models, including those used to design efficient thermal protection systems on missions bound for Venus and Mars.

Appendix A

Numerical Simulation of the Compressible Boundary Layer

Details and the MATLAB code of the similarity solution of the laminar compressible boundary layer described in Sec. 4.3.2 are provided in this section. The code of Oz et al. [67] provides a solution for the compressible boundary layer for air flow over a flat plate. The code was verified against the air cases presented in [67] (see Fig. A.1) who previously verified the code against the NASA BL2D code [34]. It was then adapted for pure CO_2 by updating the viscosity, thermal conductivity, and the Sutherland coefficients. Additionally, the boundary condition at y = 0 (Eq. 4.10) was changed to solve the boundary layer in shock fixed coordinates. The flow velocity at the wall in shock fixed coordinates is the negative of the incident shock velocity as described by Mirels theory [61].

The code is presented in three parts: Part 1 solves provides the numerical solution to the compressible boundary layer and outputs the thickness (δ_{99}) number density, and temperature along a grid of x and y points. Part 2 is the Runge-Kutta function employed in part 1. Part 3 takes the output file from part 1 and simulates the absorbance from the boundary

layer. Note for the shock tube case, the pathlength has been doubled because the line of sight across the shock tube crosses two boundary layers.

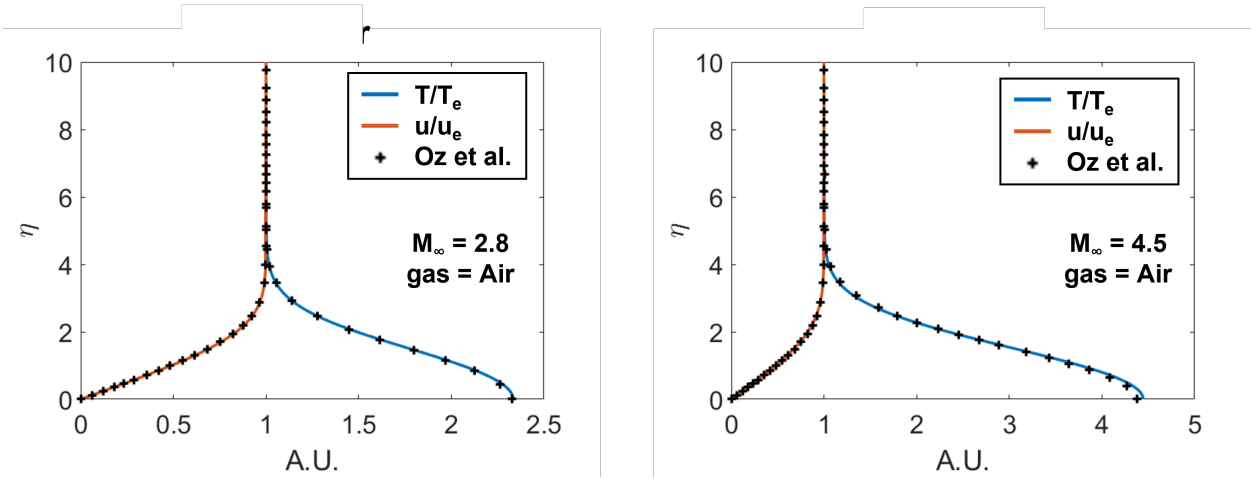

Figure A.1: Comparison of the similarity solution from this code and the solution given in Oz et al. [67] for Mach 2.8 (left) and 4.5 (right) air flows over a flat plate.

Matlab Code Part 1/3: Similarity Solution

```
clear all
close all

%This code is based off the Fluids 2021, 6, 400 article "A CFD
    Tutorial in Julia: Introduction to Compressible Laminar
    Boundary Layer Flows" by Furkan Oz and Kurssat Kara. https://
    doi.org/10.3390/fluids6110400

lim = 10;                % The value which simulates lim-> inf
N = 50000;               % Number of Points
eps = 1e-9;              % Convergence criteria
delta = 1e-10;   % Small Number for shooting method
```

```
10 %----------CHANGE THESE VARIABLES FROM RUN TO RUN
11 RunNo = 36;
12 u_inf = 203.0; %[m/s] from FROSH
13 Uis = 2000; %[m/s] from test log
14 T_inf = 1938; % [K] Freestream temperature from FROSH
15 cp_atT_inf = 1349.84; % [J/(kg K)] specific heat capacity (from
       FROSH solver)
16 gamma = 1.1649; % from FROSH
17 a_inf = 656.9; % [m/s] From FROSH
18 P_inf = 0.17285; % [atm] From FROSH
19 %----------END OF VARIABLES TO CHANGE FROM RUN TO RUN
20 maxIter = 100000;          % Max iterations
21 delta_eta = lim/N;         % Delta y
22 adibatic = 0; % Boolean either 0 or 1. If 0 specify Twall in Tw
       (dimensionless)
23 M_inf = u_inf/a_inf; %Mach number of freestream
24 Tw = 296/T_inf; % Dimensionless wall temperature (T/Te)
25 mu_ref = 1.370e-5; % [kg/(m s)] (CO2) viscosity
26 k_ref = 0.0146; % [W/(m K)] (CO2) thermal conductivity
27 c_mu = 222.0; % [K] (CO2) second coefficient of the Sutherland
       Viscosity Law NOTE THE UNITS ARE KELVIN
28 s_k = 1800; % [K] (CO2) see:https://doc.comsol.com/5.5/doc/com.
       comsol.help.cfd/cfd_ug_fluidflow_high_mach.08.27.html
29 T_ref = 273; % For Sutherland Viscocity Equation
30
31
32 %Pr calculation
```

```
33 mu_e = mu_ref*(T_inf/T_ref)^(3/2)*((T_ref+c_mu)/(T_inf+c_mu)); %
       [kg/(m s)] Sutherland Equation
34 k_atT_inf = k_ref*(T_inf/T_ref)^(3/2)*((T_ref+s_k)/(T_inf+s_k));
       % [W/(m K)] thermal conductivity of air at room temp
35 Pr = (cp_atT_inf*mu_e)/k_atT_inf; % Prandtl Number
36
37 %Initializing the solution vectors (See Listing #3 in paper)
38 y1 = zeros(N+1,1); % f
39 y2 = zeros(N+1,1); % f'
40 y3 = zeros(N+1,1); % f''
41 y4 = zeros(N+1,1); %   (   )
42 y5 = zeros(N+1,1); %   (   )'
43 eta = [0:delta_eta:delta_eta*N];
44
45 if adibatic == 1
46     y1(1) = 0;
47     y2(1) = 0;
48     y5(1) = 0;
49
50     alpha0 = 0.1; %initial guess
51     beta0  = 3.0; %initial guess
52 else
53     y1(1) = 0;
54     y2(1) = Uis/u_inf;
55     y4(1) = Tw;
56
57 %     alpha0 = 0.1; %initial guess
```

```
58 %      beta0  = 3.0; %initial guess
59       alpha0 = -10.1; %initial guess
60       beta0  = 1.1; %initial guess
61 end
62
63 AlphaList = [];
64 BetaList = [];
65
66 %% Implementation of Newton's Iteration Method (From Listing #4
       in paper)
67 for ite = 1:maxIter
68
69     if adibatic==1
70         % Boundary Conditions for adibaticabatic Case
71         y1(1) = 0;
72         y2(1) = 0;
73         y5(1) = 0;
74
75         y3(1) = alpha0;
76         y4(1) = beta0;
77     elseif adibatic==0
78         % Boundary Conditions for Isothermal Case
79         y1(1) = 0;
80 %         y2(1) = 0;
81         y2(1) = Uis/u_inf;
82         y4(1) = Tw;
83
```

```
84          y3(1) = alpha0;
85          y5(1) = beta0;
86      end
87
88      %First solution for Newton's iteration
89      [y1, y2, y3, y4, y5] = RK(N, delta_eta, y1, y2, y3, y4, y5,
            c_mu, T_inf, Pr, gamma, M_inf);
90
91      %Storing the freestream values for Newton's iteration method
92      y2o = y2(N+1);
93      y4o = y4(N+1);
94
95      if adibatic==1
96          % Boundary Conditions for adibaticabatic Case
97          y1(1) = 0;
98          y2(1) = 0;
99          y5(1) = 0;
100
101         y3(1) = alpha0+delta;
102         y4(1) = beta0;
103     elseif adibatic==0
104         % Boundary Conditions for Isothermal Case
105         y1(1) = 0;
106         y2(1) = Uis/u_inf;
107         y4(1) = Tw;
108
109         y3(1) = alpha0+delta;
```

```
110         y5(1) = beta0;
111     end
112
113     %Small number addition for Newton's iteration method
114 %       delta = 1e-10;   % Small Number for shooting method
115 %       y3(1) = alpha0 + delta; %Initial guess + small number
116 %       y4(1) = beta0; %Initial guess
117
118     %Second solution for Newton's iteration
119     [y1, y2, y3, y4, y5] = RK(N, delta_eta, y1, y2, y3, y4, y5,
            c_mu, T_inf, Pr, gamma, M_inf);
120
121     %Storing the freestream values for Newton's iteration method
122     y2n1 = y2(N+1);
123     y4n1 = y4(N+1);
124
125     %Small number addition for Newton's iteration method
126     if adibatic==1
127         % Boundary Conditions for adibaticabatic Case
128         y1(1) = 0;
129         y2(1) = 0;
130         y5(1) = 0;
131
132         y3(1) = alpha0;
133         y4(1) = beta0+delta;
134     elseif adibatic==0
135         % Boundary Conditions for Isothermal Case
```

```
136             y1(1) = 0;
137             y2(1) = Uis/u_inf;
138             y4(1) = Tw;
139
140             y3(1) = alpha0;
141             y5(1) = beta0+delta;
142         end
143 %       y3(1) = alpha0; %Initial guess
144 %       y4(1) = beta0 + delta; %Initial guess + small number
145
146         %Third solution for Newton's iteration
147         [y1, y2, y3, y4, y5] = RK(N, delta_eta, y1, y2, y3, y4, y5,
                c_mu, T_inf, Pr, gamma, M_inf);
148
149         %Storing the freestream values for Newton's iteration method
150         y2n2 = y2(N+1);
151         y4n2 = y4(N+1);
152
153         %Calculation of the next initial guess with Newton's
                iteration method
154         p11 = (y2n1 - y2o)/delta;
155         p21 = (y4n1 - y4o)/delta;
156         p12 = (y2n2 - y2o)/delta;
157         p22 = (y4n2 - y4o)/delta;
158         r1 = 1 - y2o;
159         r2 = 1 - y4o;
160         delta_alpha = (p22*r1 - p12*r2)/(p11*p22 - p12*p21);
```

```
161     delta_beta  = (p11*r2 - p21*r1)/(p11*p22 - p12*p21);
162
163     if (abs(y2(end)-1)<eps) && (abs(y4(end)-1)<eps)
164         Truey2 = y2(1);
165         Truey4 = y4(1);
166         break
167     end
168
169     alpha0 = alpha0 + delta_alpha;
170     beta0 = beta0 + delta_beta;
171
172     AlphaList = [AlphaList, alpha0];
173     BetaList = [BetaList, beta0];
174     fprintf(['iteration No. = ', num2str(ite), '\n'])
175
176 end
177
178 T_over_T_e = y4;
179 u_over_u_e = y2;
180
181 figure
182 hold on
183 plot(y4, eta, 'LineWidth', 2, 'DisplayName', 'T/T_e')
184 plot(y2, eta, 'LineWidth', 2, 'DisplayName', 'u/u_e')
185 legend
186 xlabel('A.U.')
187 ylabel('\eta')
```

```
188 box on
189 set(gca, 'FontSize', 18)
190 title(['Run No. ', num2str(RunNo)])
191 saveas(gcf, ['ShockFixedCoords_eta_', num2str(RunNo), '.fig'])
192
193 %Find eta when both u/ue and T/Te are at least 99% of freestream
      value
194
195 z = find(abs(y4-1) < 0.01);
196 zz = find(abs(y2-1) < 0.01);
197 if z(1) >= zz(1)
198     eta_bl99_index = z(1);
199 else
200     eta_bl99_index = zz(1);
201 end
202
203 eta99Cutoff = eta(eta_bl99_index);
204
205 %From Mirel's paper "Laminar boundary layer behind shock
    advancing into stationary fluid" we get an expression for y(x
    ) see eq. (17) note he uses Twall and not Te, but our
    similarity variable is of the same form except with Te so
    this solution should still be valid
206
207 int_exp = trapz(eta(1:eta_bl99_index), T_over_T_e(1:
    eta_bl99_index));
208
```

```
209 R_u = 8.31446; % [J/(mol K)]
210 MW = 0.04401; % kg/mol
211 R = R_u/MW;
212 u_e = M_inf.*a_inf;
213 P_pascals = P_inf.*101325; % [Pa]
214 rho_e = P_pascals/(R*T_inf); % [kg/m^3]
215
216 gridRes = 1e-5;
217 x_vec = [0:gridRes:0.15]; % [m]
218 delta99_vec = ((2*mu_e.*x_vec)./(u_e*rho_e)).^0.5.*int_exp;
219
220 figure
221 hold on
222 plot(x_vec.*1e2, delta99_vec.*1e3, 'LineWidth', 2, 'DisplayName'
      , '\delta{99}')
223 xlabel('x Distance [cm]')
224 ylabel('\delta_{99} [mm]')
225 set(gca, 'FontSize', 18)
226 title(['Run No. ', num2str(RunNo)])
227 box on
228 saveas(gcf, ['ShockFixedCoords_Delta99_', num2str(RunNo), '.fig'
      ])
229
230
231 %Calculate RHS of eq 17 at different values of eta
232 for j = 2:length(eta)
233     RHS_vec(j) = trapz(eta(1:j), T_over_T_e(1:j));
```

```
234 end
235
236 y_vec = [0:gridRes:max(delta99_vec)+10*gridRes]; % [m]
237 for j = 1:length(y_vec)
238     thisy = y_vec(j);
239     for jj = 1:length(x_vec)
240         thisx = x_vec(jj);
241         LHS = thisy.*(u_e*rho_e/(2*mu_e*thisx))^0.5;
242         %compare LHS to RHS (find where they match)
243         [minValue,closestIndex] = min(abs(LHS-RHS_vec));
244         thisEta = eta(closestIndex);
245         %store T_over_Te as a matrix
246         T_over_T_e_grid(j,jj) = T_over_T_e(closestIndex);
247         breakpoint = 1;
248     end
249     breakpoint = 1;
250     fprintf([num2str(j), '/', num2str(length(y_vec)), '
        completed\n'])
251 end
252
253 T_over_T_e_grid(isnan(T_over_T_e_grid))=0;
254 rho_over_rho_e_grid = 1./T_over_T_e_grid;
255 rho_grid = rho_over_rho_e_grid.*rho_e;
256 n_grid = rho_grid.*6.022e23./(MW.*100^3); %[molec/cm^3]
257 n_eq = rho_e.*6.022e23./(MW.*100^3); %[molec/cm^3]
258 T_grid = T_over_T_e_grid.*T_inf;
259
```

```
figure
surf(x_vec.*100, y_vec.*1000, T_grid)
colormap jet
shading interp
xlabel('x [cm^{-1}]')
ylabel('y [mm]')
% caxis([0 1])
set(gca, 'FontSize', 18)
h = colorbar;
xlim([min(x_vec)*100, max(x_vec)*100])
ylim([min(y_vec)*1000, max(y_vec)*1000])
set(get(h,'title'),'string','T, [K]', 'Rotation', 270.0)

figure
hold on
pcolor(x_vec.*100, y_vec.*1000, n_grid)
plot(x_vec.*1e2, delta99_vec.*1e3, 'k', 'LineWidth', 3, '
    DisplayName', '\delta{99}')
colormap jet
shading interp
xlabel('x [cm]')
ylabel('y [mm]')
xlim([min(x_vec)*100, max(x_vec)*100])
ylim([min(y_vec)*1000,max(y_vec)*1000])
caxis([n_eq, 2.0.*n_eq])
set(gca, 'FontSize', 18)
h = colorbar;
```

```
286 set(get(h,'title'),'string','n_{CO2}, [molec/cm^3]', 'Rotation',
        270.0)
287
288 figure
289 hold on
290 pcolor(x_vec.*100, y_vec.*1000, T_grid)
291 plot(x_vec.*1e2, delta99_vec.*1e3, 'k', 'LineWidth', 3, '
      DisplayName', '\delta{99}')
292 colormap jet
293 shading interp
294 xlabel('x [cm]')
295 ylabel('y [mm]')
296 xlim([min(x_vec)*100, max(x_vec)*100])
297 ylim([min(y_vec)*1000,max(y_vec)*1000])
298 caxis([min(min(T_grid)) max(max(T_grid))])
299 set(gca, 'FontSize', 18)
300 h = colorbar;
301 set(get(h,'title'),'string','T, [K]', 'Rotation', 270.0)
302
303 save(['BL_solution_', num2str(RunNo), '.mat'], 'RunNo', '
      delta99_vec', 'n_grid', 'T_grid', 'x_vec', 'y_vec')
```

Matlab Code Part 2/3: Runge-Kutta Function

```
1 function [y1, y2, y3, y4, y5] = RK(N, delta_eta, y1, y2, y3, y4,
      y5, c_mu, T_inf, Pr, gamma, M_inf)
2
```

```
% Runge–Kutta Solver based off the Fluids 2021, 6, 400 article "A CFD Tutorial in Julia: Introduction to Compressible Laminar Boundary Layer Flows" by Furkan Oz and Kurssat Kara. https://doi.org/10.3390/fluids6110400

Y1 = @(y2) y2;
Y2 = @(y3) y3;
Y3 = @(y1,y3,y4,y5,c_mu,T_inf) -y3*((y5/(2*(y4))) - (y5/(y4 + c_mu/T_inf))) - y1 * y3 * ((y4 + c_mu/T_inf)/((y4)^(0.5)*(1+ c_mu/T_inf)));
Y4 = @(y5) y5;
Y5 = @(y1,y3,y4,y5,c_mu,T_inf,M_inf,Pr,gamma) -y5^2*((0.5/y4) -(1/(y4+c_mu/T_inf))) - Pr * y1 * y5/(y4)^(0.5) * (y4 + c_mu/ T_inf)/(1 + c_mu/T_inf) - (gamma - 1) * Pr * M_inf^2 * y3^2;

    for i = 1:N
        %First Step
        k11 = Y1(y2(i));
        k21 = Y2(y3(i));
        k31 = Y3(y1(i),y3(i),y4(i),y5(i),c_mu,T_inf);
        k41 = Y4(y5(i));
        k51 = Y5(y1(i),y3(i),y4(i),y5(i),c_mu,T_inf,M_inf,Pr, gamma);

        %Second Step
        k12 = Y1(y2(i) + 0.5*delta_eta*k21);
        k22 = Y2(y3(i) + 0.5*delta_eta*k31);
```

```
22          k32 = Y3(y1(i) + 0.5*delta_eta*k11, y3(i) + 0.5*
                delta_eta*k31, y4(i) + 0.5*delta_eta*k41, y5(i) +
                0.5*delta_eta*k51, c_mu, T_inf);
23          k42 = Y4(y5(i) + 0.5*delta_eta*k51);
24          k52 = Y5(y1(i) + 0.5*delta_eta*k11, y3(i) + 0.5*
                delta_eta*k31, y4(i) + 0.5*delta_eta*k41, y5(i) +
                0.5*delta_eta*k51, c_mu, T_inf, M_inf, Pr, gamma);
25
26          %Third Step
27          k13 = Y1(y2(i) + 0.5*delta_eta*k22);
28          k23 = Y2(y3(i) + 0.5*delta_eta*k32);
29          k33 = Y3(y1(i) + 0.5*delta_eta*k12, y3(i) + 0.5*
                delta_eta*k32, y4(i) + 0.5*delta_eta*k42, y5(i) +
                0.5*delta_eta*k52, c_mu, T_inf);
30          k43 = Y4(y5(i) + 0.5*delta_eta*k52);
31          k53 = Y5(y1(i) + 0.5*delta_eta*k12, y3(i) + 0.5*
                delta_eta*k32, y4(i) + 0.5*delta_eta*k42, y5(i) +
                0.5*delta_eta*k52, c_mu, T_inf, M_inf, Pr, gamma);
32
33          %Fourth Step
34          k14 = Y1(y2(i) + 0.5*delta_eta*k23);
35          k24 = Y2(y3(i) + 0.5*delta_eta*k33);
36          k34 = Y3(y1(i) + 0.5*delta_eta*k13, y3(i) + 0.5*
                delta_eta*k33, y4(i) + 0.5*delta_eta*k43, y5(i) +
                0.5*delta_eta*k53, c_mu, T_inf);
37          k44 = Y4(y5(i) + 0.5*delta_eta*k53);
38          k54 = Y5(y1(i) + 0.5*delta_eta*k13, y3(i) + 0.5*
```

```
        delta_eta*k33, y4(i) + 0.5*delta_eta*k43, y5(i) +
        0.5*delta_eta*k53, c_mu, T_inf, M_inf, Pr, gamma);

    %Next Point Calculation
    y5(i+1) = y5(i) + (1/6)*(k51 + 2*k52 + 2*k53 + k54)*
        delta_eta;
    y4(i+1) = y4(i) + (1/6)*(k41 + 2*k42 + 2*k43 + k44)*
        delta_eta;
    y3(i+1) = y3(i) + (1/6)*(k31 + 2*k32 + 2*k33 + k34)*
        delta_eta;
    y2(i+1) = y2(i) + (1/6)*(k21 + 2*k22 + 2*k23 + k24)*
        delta_eta;
    y1(i+1) = y1(i) + (1/6)*(k11 + 2*k12 + 2*k13 + k14)*
        delta_eta;

    %check if complex---------
    tf5 = isreal(y5);
    tf4 = isreal(y4);
    tf3 = isreal(y3);
    tf2 = isreal(y2);
    tf1 = isreal(y1);
    Tarray = [tf1, tf2, tf3, tf4, tf5];

    if any(Tarray(:) < 1)
        fprintf(['Imag Detected on iteration ', num2str(i),
            '\n'])
        breakpoint = 1;
```

```
58          end
59
60          %check if complex----------
61          tf5 = isnan(y5);
62          tf4 = isnan(y4);
63          tf3 = isnan(y3);
64          tf2 = isnan(y2);
65          tf1 = isnan(y1);
66          Tarray_isnan = [tf1, tf2, tf3, tf4, tf5];
67
68          if any(Tarray_isnan(:) > 0)
69              fprintf(['NAN Detected on iteration ', num2str(i), '
                    \n'])
70              breakpoint = 1;
71          end
72      end
73  end
```

Matlab Code Part 3/3: Boundary Layer Absorbance Simulator

```
1  clear all
2  close all
3
4  RunNo = 36;
5  BLFile = load(['BL_solution_', num2str(RunNo(1)), '.mat']);
```

```
6  f1 = load('ProcessedRunFile.mat'); % load a file that contains
       the points you want to simulate the boundary layer at and the
       wavenumber range
7
8  xVecOfInterest = f1.XVec; % [cm] Points you want to simulate the
       boundary layer at
9  WN_range = f1.WavenumberVec; % [cm^{-1}] Wavenumber for spectral
       region to simulate
10
11 figure
12 hold on
13 surf(BLFile.x_vec.*100, BLFile.y_vec.*1000, BLFile.n_grid)
14 colormap jet
15 shading interp
16 xlabel('x [cm]')
17 ylabel('y [mm]')
18 xlim([min(BLFile.x_vec)*100, max(BLFile.x_vec)*100])
19 ylim([min(BLFile.y_vec)*1000,max(BLFile.y_vec)*1000])
20 set(gca, 'FontSize', 18)
21 h = colorbar;
22 set(get(h,'title'),'string','n_{CO2}, [molec/cm^3]')
23
24 figure
25 hold on
26 pcolor(BLFile.x_vec.*100, BLFile.y_vec.*1000, BLFile.T_grid)
27 plot(BLFile.x_vec.*1e2, BLFile.delta99_vec.*1e3, 'k', 'LineWidth
       ', 3, 'DisplayName', '\delta{99}')
```

```
28 colormap jet
29 shading interp
30 xlabel('x [cm]')
31 ylabel('y [mm]')
32 xlim([min(BLFile.x_vec)*100, max(BLFile.x_vec)*100])
33 ylim([min(BLFile.y_vec)*1000,max(BLFile.y_vec)*1000])
34 caxis([min(min(BLFile.T_grid)) max(max(BLFile.T_grid))])
35 set(gca, 'FontSize', 18)
36 h = colorbar;
37 set(get(h,'title'),'string','T, [K]')
38
39 BLT_grid = BLFile.T_grid; %[K]
40 BLn_grid = BLFile.n_grid; %[molec/cm^3]
41 delta99 = BLFile.delta99_vec.*1000; %[mm]
42 BLX_vec = BLFile.x_vec.*100; % [cm]
43 BLY_vec = BLFile.y_vec.*1000;% [mm]
44
45 for j = 2:length(xVecOfInterest)
46     thisX = xVecOfInterest(j);
47     %extract the T and n profile for each x point
48     [minValue,closestIndex] = min(abs(BLX_vec-thisX));
49     TValues(j,:) = BLT_grid(:,closestIndex);
50     nValues(j,:) = BLn_grid(:,closestIndex);
51     delta99Val(j) = delta99(closestIndex);
52 end
53
54 %cutoff the T and n vector at the delta99 to only be simulating
```

```
    the boundary layer
for j = 2:length(xVecOfInterest)
    thisAbs = 0;
    ycutoff = delta99Val(j);
    %     shorten the T and n vectors at each x to only contain
        the boundary layer
    for jj = 2:length(TValues(j,:))
        if BLY_vec(jj) <= ycutoff
            thisT = TValues(j,jj); %[K]
            thisn = nValues(j,jj); %[molec/cm^3]
            thisL = 2*(BLY_vec(jj+1)-BLY_vec(jj))/10; %[cm]
            % Simulate the absorbance based on the temperature,
                number density, and pathlength
            SimBLConditions(j,:) = [thisT, thisn, thisL,
                WN_range];
            thisAbsSlice = CO2_Absorb_Sim(SimBLConditions(j,:));
            thisAbs = thisAbs + thisAbsSlice;
        else
            break
        end
        breakpoint = 1;
    end

    SimulatedBLAbs(j,:) = thisAbs;

    figure
    plot(WN_range, SimulatedBLAbs(j,:))
```

```
78        xlabel('Wavenumber [cm]')
79        ylabel('Absorbance, \alpha')
80
81    end
```

Appendix B

Laser Safety and Enclosure Design for EAST Facility

The operation of a laser system at NASA Ames requires a laser safety permit and details of the laser safety permit obtained in this work are provided for the general benefit of others operating or planning to operate similar portable laser systems at various facilities.

This laser system is typically used for direct absorption measurements of CO_2 and CO in the UCLA shock tube facility. This sensor has been adapted for tests at the Electric Arc Shock Tube (EAST) facility. The lasers are scanned over fundamental band absorption features giving a measurement of line shape and strength of each state probed. This provides information on species concentration and gas temperatures. Although the laser sources are classified as Class 3B, it is contained in two enclosed boxes that are aligned initially at UCLA. When it is integrated onto the EAST facility, some fine tuning of the alignment is needed. A germanium etalon is integrated on a flip mount. The etalon is used to make the time to wavenumber transformation and is needed to analyze the absorbance data. During operation, the top of the laser enclosure will be accessed by an authorized laser user wearing

Table B.1: Laser Specifications

Specification	Laser 1	Laser 2
Manufacturer	NanoPlus	Alpes
Model	4193nm-DFB-T066	sbcw9065
Serial	2280/1-8	HHL-790
Type/Lasing Medium	Interband Cascade Laser	Quantum Cascade Laser
Laser Hazard Class	3B	3B
Wavelength	4184 - 4198 nm	4970 - 5000 nm
Continuous Wave or Pulsed	Continuous Wave	Continuous Wave
Max Power	6 mW	90 mW
Beam Diameter	< 2.5 mm	< 2.5 mm
Divergence	< 5 mrad	< 6 mrad
Minimum Safe OD	2	2

laser eye protection (OD 2 at 4000-5000 nm) to initially align the system on EAST, and record background and etalon signals before each test. The nominal hazard zone (NHZ) will be cordoned off and warning signs posted on the barriers. After the box is sealed it is treated as a Class 1 laser. Laser specifications are shown in Table B.1. The laser enclosure is shown in Fig. B.1 and 3/16" gray acrylic (McMaster part number: 8505K727) is used to enclose the beam. Transmittance of the gray acrylic housing was measured in an FTIR and is shown to be less than 0.2% over the wavelengths of the enclosed beams (Fig. B.2). This results in an optical density of > 2.6 at these wavelengths (calculated via Eq. B.1).

$$OD = log_{10}(100/\tau) \tag{B.1}$$

OD is the optical density and τ is the transmittance [%]. For reference, an optical density of 1 allows 10% of the light to be transmitted, 2 allows 1%, 3 allows, 0.1%, etc.

Both lasers emit a medium power, non-visible (infrared) beams. The beams may be hazardous under direct and specular reflection viewing conditions, but are normally not a fire hazard, diffuse reflection hazard, nor a laser generated air contaminant production hazard. For mid-infrared lasers of this wavelength, the maximum permissible exposure (MPE) is 0.1 W/cm^2 for the anticipated worst case exposure duration of 10 seconds, per ANSI Z136.1-

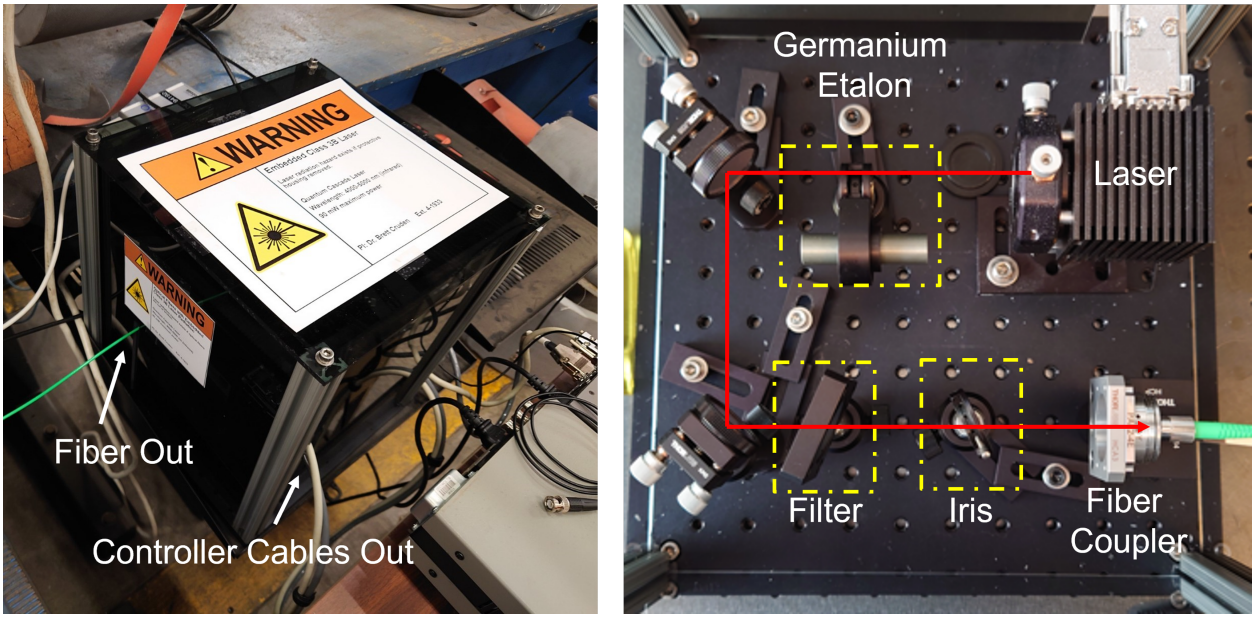

Figure B.1: Photograph of the laser enclosure used at the EAST facility (left). Photograph of the inside of the laser enclosure (right).

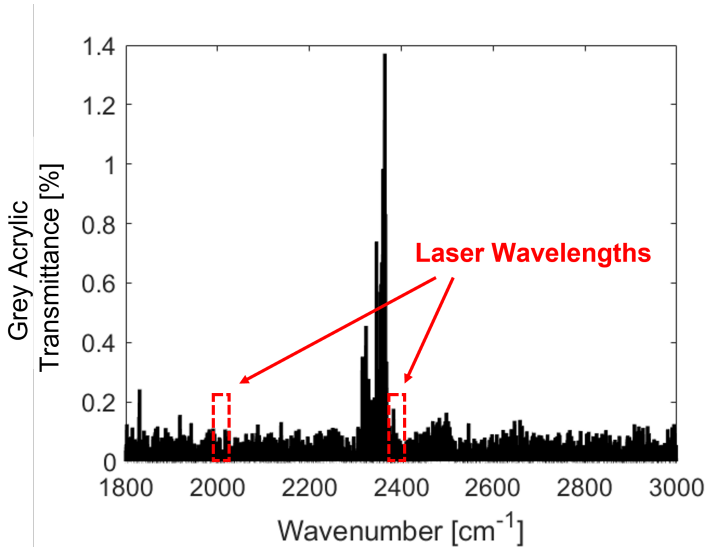

Figure B.2: FTIR scan of the grey acrylic used to enclose the laser and fiber coupling optics. Wavelength regions of the lasers enclosed are highlighted in the red boxes.

2014. The nominal ocular hazard distance (NOHD) of the laser is computed from Eq. B.2.

$$NOHD = \frac{1}{\phi}\left(\frac{4\Phi}{\pi MPE} - a^2\right)^{1/2} \tag{B.2}$$

Φ is power [W], ϕ is divergence [rad], a is beam diameter [cm] and MPE is the maximum permissible exposure [W/cm^2]. The NOHD is computed as 1.73 m for the Alpes laser, and 0.24 m for the NanoPlus laser. The nominal hazard zone (NHZ) is contained within a sphere of this radius. The NHZ of this NanoPlus laser will always be inside of that of the Alpes laser.

In total, the six laser hazard controls listed below were clearly enumerated in the safety permit.

1. Each laser is housed in its own enclosure (with dimensions: 12" x 12" x 12") and is placed side by side to facilitate an easily defined laser controlled area.
2. When the lasers are not fully enclosed (during setup/alignment), a laser controlled area is blocked off with a movable barrier displaying warning signs. The laser controlled area is set at a 2 m radius measured from the 90 mW Alpes laser. This area captures the NHZ for both lasers.
3. When the laser enclosures are fully shut, the risk is mitigated to a class 1 laser system as the radiation is contained in the enclosure, EAST, and optical fibers. The laser enclosures require a tool to unscrew 4 bolts to obtain access.
4. Laser warning labels are posted on the enclosure and optical fibers.
5. The lasers are key activated. The keys control power to the laser. The control key is not left in the machine when unattended and is kept in the custody of authorized personnel only.
6. Laser eye protection (OD 2 at 4000-5000 nm) is required during the alignment process and when laser radiation is not fully enclosed.

In the event someone enters the NHZ without appropriate eye protection, or another emergency arises, the laser is immediately shut off by turning the key interlock on the controller.

Lastly, additional analysis was carried out in the event the fiber becomes accidentally separated/severed from the laser enclosure. The fiber coupling optics within the laser enclosure focus the beam into the fiber optic cable. The coupler has a focal distance of 4 mm and the resulting beam sizes at the focus are 8.5 and 10.1 μm for the 4.19 and 4.98 micron laser respectively. In the event that the cable is accidentally separated/severed from the laser enclosure during normal operation, the beam properties as it exits the laser enclosure after passing through the focusing lens are as follows: Laser 1: $<$ 6 mW, 31.6 mm beam diameter, and 157 mrad divergence 1/2 angle. Laser 2: $<$ 90 mW, 32.0 mm beam waist radius, and 159 mrad divergence 1/2 angle. In this situation, the resulting beam cannot exceed the MPE of 0.1 W/cm^2 outside of the laser enclosure.

Bibliography

[1] I. V. Adamovich, S. O. Macheret, J. W. Rich, and C. E. Treanor. Vibrational energy transfer rates using a forced harmonic oscillator model. *Journal of Thermophysics and Heat Transfer*, 12(1):57–65, 1998.

[2] B. J. McBride, M. J. Zehe, and S. Gordon. NASA Glenn coefficients for calculating thermodynamic properties of individual species. *John H. Glenn Research Center at Lewis Field*, (September), 2002.

[3] F. Bendana. *Shock tube kinetics and laser absorption diagnostics for liquid- and hybrid-propellant rocket combustion analysis*. PhD thesis, University of California, Los Angeles, 2020.

[4] F. A. Bendana, D. D. Lee, C. Wei, D. I. Pineda, and R. M. Spearrin. Line mixing and broadening in the v(1→3) first overtone bandhead of carbon monoxide at high temperatures and high pressures. *Journal of Quantitative Spectroscopy and Radiative Transfer*, 239:106636, 12 2019.

[5] H. A. Bethe and E. Teller. Deviations from thermal equilibrium in shock waves. Technical report, Engineering Research Inst., Univ. of Mich.; Cornell Univ.; George Washington Univ., 1953.

[6] G. Bohm and G. Zech. *Introduction to Statistics and Data Analysis for Physicists*. 2010.

[7] A. Brandis, C. Johnston, B. Cruden, D. Prabhu, A. Wray, Y. Liu, D. Schwenke, and D. Bose. Validation of CO 4th positive radiation for Mars entry. *Journal of Quantitative Spectroscopy and Radiative Transfer*, 121:91–104, 5 2013.

[8] A. M. Brandis, D. A. Saunders, C. O. Johnston, B. A. Cruden, and T. R. White. Radiative heating on the after-body of Martian entry vehicles. In *Journal of Thermophysics and Heat Transfer*, volume 34, pages 66–77. American Institute of Aeronautics and Astronautics Inc., 2020.

[9] O. Brandt and P. Roth. Temperature measurements behind shock waves using a rapid scanning IR-diode laser. *Physics of Fluids*, 30(5):1294, 1987.

[10] M. F. Campbell, K. G. Owen, D. F. Davidson, and R. K. Hanson. Dependence of Calculated Postshock Thermodynamic Variables on Vibrational Equilibrium and Input Uncertainty. *Journal of Thermophysics and Heat Transfer*, 31(3):586–608, 7 2017.

[11] G. V. Candler, H. B. Johnson, I. Nompelis, P. K. Subbareddy, T. W. Drayna, V. Gidzak, and M. D. Barnhardt. Development of the US3D Code for Advanced Compressible and Reacting Flow Simulations. Technical report.

[12] Carmac M. CO2 Relaxation Processes in Shock Waves. In J. G. Hall, editor, *Fundamental Phenomena in Hypersonic Flow*, pages 195–215. Cornell University Press, Ithaca, 1966.

[13] B. A. Cruden. Absolute Radiation Measurements in Earth and Mars Entry Conditions. *Radiation and Gas-Surface Interaction Phenomena in High Speed Re-Entry - STO AVT-218*, pages 1–40, 2014.

[14] B. A. Cruden, A. M. Brandis, and M. E. Macdonald. Characterization of CO thermochemistry in incident shockwaves. *2018 Joint Thermophysics and Heat Transfer Conference*, pages 1–22, 2018.

[15] B. A. Cruden, R. Martinez, J. H. Grinstead, and J. Olejniczak. Simultaneous vacuum ultraviolet through near IR absolute radiation measurement with spatiotemporal resolution in an Electric Arc Shock Tube. In *41st AIAA Thermophysics Conference*. American Institute of Aeronautics and Astronautics Inc., 2009.

[16] B. A. Cruden, R. A. Miller, A. M. Brandis, A. C. Tibere-Inglesse, C. C. Jelloian, R. M. Spearrin, T. K. West, C. O. Johnston, D. K. Prabhu, J. Monk, J. Clarke, L. D. Mare, and M. McGilvray. MARS 2020 BACKSHELL RADIATIVE HEATING MEASUREMENT AND SHOCK TUBE VERIFICATION. In *9th International Workshop on Radiation of High Temperature Gases for Space Missions*, Santa Maria, Azores, Portugal, 9 2022.

[17] B. A. Cruden, D. K. Prabhu, and A. M. Brandis. Measurement and characterization of mid-wave infrared radiation in CO2 shocks. In *AIAA AVIATION 2014 -11th AIAA/ASME Joint Thermophysics and Heat Transfer Conference*. American Institute of Aeronautics and Astronautics Inc., 2014.

[18] B. A. Cruden, D. K. Prabhu, and A. M. Brandis. Measurement and characterization of mid-wave infrared radiation in CO2 shocks. In *AIAA AVIATION 2014 -11th AIAA/ASME Joint Thermophysics and Heat Transfer Conference*. American Institute of Aeronautics and Astronautics Inc., 2014.

[19] H. Drawin and F. Emard. Atom-atom excitation and ionization in shock waves of the noble gases. *Physics Letters A*, 43(4):333–335, 3 1973.

[20] J. N. Fox, T. I. McLaren, and R. M. Hobson. Test time and particle paths in low-pressure shock tubes. *Physics of Fluids*, 9(12):2345–2350, 1966.

[21] H. B. Franz, M. G. Trainer, C. A. Malespin, P. R. Mahaffy, S. K. Atreya, R. H. Becker, M. Benna, P. G. Conrad, J. L. Eigenbrode, C. Freissinet, H. L. Manning, B. D. Prats, E. Raaen, and M. H. Wong. Initial SAM calibration gas experiments on Mars: Quadrupole mass spectrometer results and implications. *Planetary and Space Science*, 138:44–54, 4 2017.

[22] A. Gaydon and I. Hurle. *The shock tube in high-temperature chemical physics*. Reinhold Pub. Corp, New York, 1963.

[23] J. J. Girard, P. M. Finch, C. L. Strand, R. K. Hanson, W. M. Yu, J. M. Austin, and H. G. Hornung. Measurements of time-resolved air freestream nitric oxide rotational, vibrational temperature and concentration in the t5 reflected shock tunnel. In *AIAA Propulsion and Energy 2020 Forum*, 2020.

[24] J. J. Girard, P. M. Finch, C. L. Strand, R. K. Hanson, W. M. Yu, J. M. Austin, H. G. Hornung, and P. J. Drummond. Measurements of reflected shock tunnel freestream nitric oxide temperatures and partial pressure. *AIAA Journal*, 59(12):5266–5275, 12 2021.

[25] P. A. Gnoffo. An Upwind-Biased, Point-Implicit Relaxation Algorithm for Viscous, Compressible Perfect-Gas Flows. Technical report, NASA Langley Research Center, Hampton, VA, 2 1990.

[26] C. Goldenstein, R. Spearrin, J. Jeffries, and R. Hanson. Infrared laser-absorption sensing for combustion gases. *Progress in Energy and Combustion Science*, 60:132–176, 5 2017.

[27] C. S. Goldenstein, V. A. Miller, R. Mitchell Spearrin, and C. L. Strand. SpectraPlot.com: Integrated spectroscopic modeling of atomic and molecular gases. *Journal of Quantitative Spectroscopy and Radiative Transfer*, 200:249–257, 10 2017.

[28] I. Gordon, L. Rothman, R. Hargreaves, R. Hashemi, E. Karlovets, F. Skinner, E. Conway, C. Hill, R. Kochanov, Y. Tan, P. Wcisło, A. Finenko, K. Nelson, P. Bernath, M. Birk, V. Boudon, A. Campargue, K. Chance, A. Coustenis, B. Drouin, J. Flaud, R. Gamache, J. Hodges, D. Jacquemart, E. Mlawer, A. Nikitin, V. Perevalov, M. Rotger, J. Tennyson, G. Toon, H. Tran, V. Tyuterev, E. Adkins, A. Baker, A. Barbe, E. Canè, A. Császár, A. Dudaryonok, O. Egorov, A. Fleisher, H. Fleurbaey, A. Foltynowicz, T. Furtenbacher, J. Harrison, J. Hartmann, V. Horneman, X. Huang, T. Karman, J. Karns, S. Kassi, I. Kleiner, V. Kofman, F. Kwabia–Tchana, N. Lavrentieva, T. Lee, D. Long, A. Lukashevskaya, O. Lyulin, V. Makhnev, W. Matt, S. Massie, M. Melosso, S. Mikhailenko, D. Mondelain, H. Müller, O. Naumenko, A. Perrin, O. Polyansky, E. Raddaoui, P. Raston, Z. Reed, M. Rey, C. Richard, R. Tóbiás, I. Sadiek, D. Schwenke, E. Starikova, K. Sung, F. Tamassia, S. Tashkun, J. Vander Auwera, I. Vasilenko, A. Vigasin, G. Villanueva, B. Vispoel, G. Wagner, A. Yachmenev, and S. Yurchenko. The HITRAN2020 molecular spectroscopic database. *Journal of Quantitative Spectroscopy and Radiative Transfer*, 277:107949, 2022.

[29] I. Gordon, L. Rothman, C. Hill, R. Kochanov, Y. Tan, P. Bernath, M. Birk, V. Boudon, A. Campargue, K. Chance, B. Drouin, J.-M. Flaud, R. Gamache, J. Hodges, D. Jacquemart, V. Perevalov, A. Perrin, K. Shine, M.-A. Smith, J. Tennyson, G. Toon, H. Tran, V. Tyuterev, A. Barbe, A. Császár, V. Devi, T. Furtenbacher, J. Harrison, J.-M. Hartmann, A. Jolly, T. Johnson, T. Karman, I. Kleiner, A. Kyuberis, J. Loos, O. Lyulin, S. Massie, S. Mikhailenko, N. Moazzen-Ahmadi, H. Müller, O. Naumenko, A. Nikitin, O. Polyansky, M. Rey, M. Rotger, S. Sharpe, K. Sung, E. Starikova, S. Tashkun, J. V. Auwera, G. Wagner, J. Wilzewski, P. Wcisło, S. Yu, and E. Zak. The HITRAN2016 molecular spectroscopic database. *Journal of Quantitative Spectroscopy and Radiative Transfer*, 203:3–69, 12 2017.

[30] C. H. Grimaldi, S. D. McGuire, and C. O. Laux. Infrared emission measurements of a recombining CO2 plasma. *AIAA Science and Technology Forum and Exposition, AIAA SciTech Forum 2022*, pages 1–10, 2022.

[31] R. Hanson, R. Spearrin, and C. Goldenstein. *Spectroscopy and Optical Diagnostics for Gases*. Springer International Publishing, 2016.

[32] R. K. Hanson. Shock-tube study of carbon monoxide dissociation kinetics. *The Journal of Chemical Physics*, 4970(August 2003):4970–4976, 1974.

[33] D. Hash, J. Olejniczak, M. Wright, D. Prabhu, M. Pulsonetti, B. Hollis, P. Gnoffo, M. Barnhardt, I. Nompelis, and G. Candler. FIRE II calculations for hypersonic nonequilibrium aerothermodynamics code verification: DPLR, LAURA, and US3D. In *Collection of Technical Papers - 45th AIAA Aerospace Sciences Meeting*, volume 11, pages 7322–7339, 2007.

[34] V. Iyer. Computer Program BL2D for Solving Two-Dimensional and Axisymmetric Boundary Layers. Technical report, NASA-CR-4668, Washington DC, 1995.

[35] C. C. Jelloian, F. A. Bendana, C. Wei, R. M. Spearrin, and M. E. Macdonald. Nonequilibrium Vibrational, Rotational, and Translational Thermometry via Megahertz Laser Absorption of CO. *Journal of Thermophysics and Heat Transfer*, 36(2):266–275, 2022.

[36] C. C. Jelloian, N. Q. Minesi, and R. M. Spearrin. High-speed mid-infrared laser absorption spectroscopy of CO2 for shock-induced thermal non-equilibrium studies of planetary entry. *Applied Physics B*, 128(12):216, 12 2022.

[37] C. Johnston and A. Brandis. Modeling of nonequilibrium CO Fourth-Positive and CN Violet emission in CO 2 –N 2 gases. *Journal of Quantitative Spectroscopy and Radiative Transfer*, 149:303–317, 12 2014.

[38] C. Johnston, A. Brandis, and K. Sutton. Shock Layer Radiation Modeling and Uncertainty for Mars Entry. In *43rd AIAA Thermophysics Conference*, pages 1–43, Reston, Virigina, 6 2012. American Institute of Aeronautics and Astronautics.

[39] C. O. Johnston, R. W. Barnwell, B. R. Hollis, J. A. Schetz, and R. W. Walters. Nonequilibrium Shock-Layer Radiative Heating for Earth and Titan Entry. Technical report, 2006.

[40] C. O. Johnston, B. R. Hollis, and K. Sutton. Spectrum Modeling for Air Shock-Layer Radiation at Lunar-Return Conditions. *Journal of Spacecraft and Rockets*, 45(5), 9 2008.

[41] G. Kamimoto and H. Matsui. Vibrational Relaxation of Carbon Dioxide in Argon. *The Journal of Chemical Physics*, 53(10):3990–3993, 11 1970.

[42] B. L. M. Klarenaar, R. Engeln, D. C. M. van den Bekerom, M. C. M. van de Sanden, A. S. Morillo-Candas, and O. Guaitella. Time evolution of vibrational temperatures in a CO 2 glow discharge measured with infrared absorption spectroscopy. *Plasma Sources Science and Technology*, 26(11):115008, 10 2017.

[43] A. Kosareva, O. Kunova, E. Kustova, and E. Nagnibeda. Four-temperature kinetic model for CO2vibrational relaxation. *Physics of Fluids*, 33(1), 1 2021.

[44] E. Kustova and M. Mekhonoshina. Calculation of vibrational relaxation times in carbon dioxide using forced harmonic oscillator model. In *AIP Conference Proceedings*, volume 2351. American Institute of Physics Inc., 5 2021.

[45] E. Kustova, M. Mekhonoshina, and A. Kosareva. Relaxation processes in carbon dioxide. *Physics of Fluids*, 31(4), 4 2019.

[46] E. V. Kustova and E. A. Nagnibeda. State-to-state theory of vibrational kinetics and dissociation in three-atomic gases. In *AIP Conference Proceedings 585, 620*, 2 2001.

[47] D. D. Lee, F. A. Bendana, A. P. Nair, D. I. Pineda, and R. M. Spearrin. Line mixing and broadening of carbon dioxide by argon in the v3 bandhead near 4.2 µm at high temperatures and high pressures. *Journal of Quantitative Spectroscopy and Radiative Transfer*, 253:107135, 9 2020.

[48] D. D. Lee, F. A. Bendana, and R. M. Spearrin. Laser Absorption Spectroscopy of Carbon Monoxide near 4.97 μm for Temperature and Species Measurements in Hydrocarbon-Fueled Rockets. In *2018 AIAA Aerospace Sciences Meeting*, number 210059. American Institute of Aeronautics and Astronautics, 1 2018.

[49] D. D. Lee, F. A. Bendana, and R. M. Spearrin. Exploiting line mixing effects for laser absorption spectroscopy at extreme combustion conditions. *11th U.S. National Combustion Meeting*, 2019.

[50] Y. Li, S. Wang, C. L. Strand, and R. K. Hanson. Development of a Stark shift measurement technique using excited-state oxygen atoms to determine electron number density in shock heated O 2 /Ar above 10 000 K. *Plasma Sources Science and Technology*, 30(2):025007, 2 2021.

[51] X. Lin, L. Z. Chen, J. P. Li, F. Li, and X. L. Yu. Experimental and Numerical Study of Carbon-Dioxide Dissociation for Mars Atmospheric Entry. *Journal of Thermophysics and Heat Transfer*, 32(2):503–513, 4 2018.

[52] X. Lin, X. L. Yu, F. Li, S. H. Zhang, J. G. Xin, and X. Y. Chang. CO concentration and temperature measurements in a shock tube for Martian mixtures by coupling OES and TDLAS. *Applied Physics B: Lasers and Optics*, 110(3):401–409, 3 2013.

[53] P. Linstrom, W. Mallard, and Eds. *NIST Chemistry WebBook, NIST Standard Reference Database Number 69*. National Institute of Standards and Technology, Gaithersburg, MD, 2020.

[54] A. Little, D. Bose, C. Karlgaard, M. Munk, C. Kuhl, M. Schoenenberger, C. Antill, R. Verhappen, P. Kutty, and T. White. THE MARS SCIENCE LABORATORY (MSL) ENTRY, DESCENT AND LANDING INSTRUMENTATION (MEDLI): HARDWARE PERFORMANCE AND DATA RECONSTRUCTION. Technical report, NTRS, 2 2013.

[55] M. E. MacDonald, A. M. Brandis, and B. A. Cruden. Temperature and CO Number Density Measurements in Shocked CO and CO2 via Tunable Diode Laser Absorption Spectroscopy. In *2018 Joint Thermophysics and Heat Transfer Conference*, pages 1–23, Reston, Virginia, 6 2018. American Institute of Aeronautics and Astronautics.

[56] S. D. McGuire, A. C. Tibère-Inglesse, P. B. Mariotto, B. A. Cruden, and C. O. Laux. Measurements and modeling of CO 4th positive (A–X) radiation. *Journal of Quantitative Spectroscopy and Radiative Transfer*, 245:106855, 4 2020.

[57] R. A. Miller, C. Y. Tang, T. R. White, and B. A. Cruden. MEDLI2: MISP Measured Aftbody Aerothermal Environments. In *AIAA Science and Technology Forum and Exposition, AIAA SciTech Forum 2022*. American Institute of Aeronautics and Astronautics Inc, AIAA, 2022.

[58] R. C. Millikan. Carbon Monoxide Vibrational Relaxation in Mixtures with Helium, Neon, and Krypton. *The Journal of Chemical Physics*, 40(9):2594–2596, 5 1964.

[59] R. C. Millikan and D. R. White. Systematics of Vibrational Relaxation. *The Journal of Chemical Physics*, 39(12):3209–3213, 12 1963.

[60] N. Q. Minesi, M. O. Richmond, C. C. Jelloian, N. M. Kuenning, A. P. Nair, and R. M. Spearrin. Multi-line Boltzmann regression for near-electronvolt temperature and CO sensing via MHz-rate infrared laser absorption spectroscopy. *Applied Physics B: Lasers and Optics*, 128(12):214, 12 2022.

[61] H. MIRELS. Boundary Layer Behind Shock or Thin Expansion Wave Moving Into Stationary Fluid. *NACA Tech. Note 3712*, 1956.

[62] A. Nair, D. Lee, D. Pineda, J. Kriesel, W. Hargus, J. Bennewitz, S. Danczyk, and R. Spearrin. MHz laser absorption spectroscopy via diplexed RF modulation for pressure, temperature, and species in rotating detonation rocket flows. *Applied Physics B*, 126(8):138, 8 2020.

[63] A. P. Nair, C. Jelloian, D. S. Morrow, F. A. Bendana, D. I. Pineda, and R. M. Spearrin. MHz mid-infrared laser absorption sensor for carbon monoxide and temperature behind detonation waves. In *AIAA Scitech 2020 Forum*, Reston, Virginia, 1 2020. American Institute of Aeronautics and Astronautics.

[64] A. P. Nair, N. Q. Minesi, C. Jelloian, N. M. Kuenning, and R. M. Spearrin. Extended tuning of distributed-feedback lasers in a bias-tee circuit via waveform optimization for MHz-rate absorption spectroscopy. *Measurement Science and Technology*, 33(10):105104, 10 2022.

[65] M. Nations, S. Wang, C. S. Goldenstein, D. F. Davidson, and R. K. Hanson. Kinetics of Excited Oxygen Formation in Shock-Heated O 2 –Ar Mixtures. *The Journal of Physical Chemistry A*, 120(42):8234–8243, 10 2016.

[66] M. A. Oehlschlaeger, D. F. Davidson, and J. B. Jeffries. Temperature measurement using ultraviolet laser absorption of carbon dioxide behind shock waves. *Applied Optics*, 44(31):6599, 11 2005.

[67] F. Oz and K. Kara. A CFD Tutorial in Julia: Introduction to Compressible Laminar Boundary-Layer Flows. *Fluids*, 6(400), 11 2021.

[68] G. Palmer and B. A. Cruden. Experimental validation of CO2 radiation simulations. In *43rd AIAA Thermophysics Conference 2012*, 2012.

[69] E. Pannier and C. O. Laux. RADIS: A nonequilibrium line-by-line radiative code for CO2 and HITRAN-like database species. *Journal of Quantitative Spectroscopy and Radiative Transfer*, 222-223:12–25, 2019.

[70] C. Park. *Nonequilibrium hypersonic aerothermodynamics*. NTRS: 19910029860, 1989.

[71] C. Park. Review of chemical-kinetic problems of future NASA missions. I - Earth entries. *Journal of Thermophysics and Heat Transfer*, 7(3):385–398, 7 1993.

[72] C. Park, J. T. Howe, R. L. Jaffe, and G. V. Candler. Review of chemical-kinetic problems of future NASA missions, II: Mars entries. *Journal of Thermophysics and Heat Transfer*, 8(1):9–23, 1994.

[73] G. J. Rosasco, L. A. Rahn, W. S. Hurst, R. E. Palmer, and S. M. Dohne. Measurement and prediction of Raman Q -branch line self-broadening coefficients for CO from 400 to 1500 K. *The Journal of Chemical Physics*, 90(8):4059–4068, 4 1989.

[74] L. Rosenmann, J. M. Hartmann, M. Y. Perrin, and J. Taine. Accurate calculated tabulations of IR and Raman CO_2 line broadening by CO_2, H_2O, N_2, O_2 in the 300–2400-K temperature range. *Applied Optics*, 27(18):3902, 9 1988.

[75] L. Rothman, I. Gordon, R. Barber, H. Dothe, R. Gamache, A. Goldman, V. Perevalov, S. Tashkun, and J. Tennyson. HITEMP, the High-Temperature Molecular Spectroscopic Database. *Journal of Quantitative Spectroscopy and Radiative Transfer*, 111(15):2139–2150, 10 2010.

[76] M. Satchell, M. McGilvray, and L. Di Mare. Analytical Method of Evaluating Nonuniformities in Shock Tube Flows: Theory and Development. *AIAA Journal*, 60(2):654–668, 2 2022.

[77] K. K. Schwarm, C. Wei, D. I. Pineda, R. Mitchell Spearrin, and R. M. Spearrin. Time-resolved laser absorption imaging of ethane at 2 kHz in unsteady partially premixed flames. *Applied Optics*, 58(21):5656, 7 2019.

[78] R. N. Schwartz, Z. I. Slawsky, and K. F. Herzfeld. Calculation of vibrational relaxation times in gases. *The Journal of Chemical Physics*, 20(10):1591–1599, 1952.

[79] C. J. S. M. Simpson and T. R. D. Chandler. A shock tube study of vibrational relaxation in pure CO2 and mixtures of CO2 with the inert gases, nitrogen, deuterium and hydrogen. Technical report, 1970.

[80] P. Sinclair, P. Duggan, R. Berman, A. May, and J. Drummond. Line Broadening, Shifting, and Mixing in the Fundamental Band of CO Perturbed by N2at 301 K. *Journal of Molecular Spectroscopy*, 181(1):41–47, 1 1997.

[81] R. Spearrin, C. Goldenstein, I. Schultz, J. Jeffries, and R. Hanson. Simultaneous sensing of temperature, CO, and CO2 in a scramjet combustor using quantum cascade laser absorption spectroscopy. *Applied Physics B: Lasers and Optics*, 117(2):689–698, 11 2014.

[82] R. Spearrin, S. Li, D. Davidson, J. Jeffries, and R. Hanson. High-temperature isobutene absorption diagnostic for shock tube kinetics using a pulsed quantum cascade laser near 11.3 μm. *Proceedings of the Combustion Institute*, 35(3):3645–3651, 2015.

[83] R. M. Spearrin, C. S. Goldenstein, J. B. Jeffries, and R. K. Hanson. Fiber-coupled 2.7 μm laser absorption sensor for CO2in harsh combustion environments. *Measurement Science and Technology*, 24(5):055107, 5 2013.

[84] R. M. Spearrin, C. S. Goldenstein, J. B. Jeffries, and R. K. Hanson. Quantum cascade laser absorption sensor for carbon monoxide in high-pressure gases using wavelength modulation spectroscopy. *Applied Optics*, 53(9):1938, 3 2014.

[85] R. M. Spearrin, W. Ren, J. B. Jeffries, and R. K. Hanson. Multi-band infrared CO2 absorption sensor for sensitive temperature and species measurements in high-temperature gases. *Applied Physics B*, 116(4):855–865, 9 2014.

[86] C. Y. Tang, M. Mahzari, D. K. Prabhu, H. S. Alpert, and B. A. Cruden. MEDLI2: MISP Inferred Aerothermal Environment and Flow Transition Assessment. In *AIAA Science and Technology Forum and Exposition, AIAA SciTech Forum 2022*. American Institute of Aeronautics and Astronautics Inc, AIAA, 2022.

[87] S. A. Tashkun and V. I. Perevalov. CDSD-4000: High-resolution, high-temperature carbon dioxide spectroscopic databank. *Journal of Quantitative Spectroscopy and Radiative Transfer*, 112(9):1403–1410, 2011.

[88] S. A. Tashkun, V. I. Perevalov, J.-L. Teffo, L. S. Rothman, and V. G. Tyuterevn. GLOBAL FITTING OF CO VIBRATIONAL-ROTATIONAL LINE POSITIONS USING THE EFFECTIVE HAMILTONIAN APPROACH. Technical Report 5, 1998.

[89] J. Tennyson, S. N. Yurchenko, A. F. Al-Refaie, E. J. Barton, K. L. Chubb, P. A. Coles, S. Diamantopoulou, M. N. Gorman, C. Hill, A. Z. Lam, L. Lodi, L. K. McKemmish, Y. Na, A. Owens, O. L. Polyansky, C. Sousa-Silva, D. S. Underwood, A. Yachmenev, and E. Zak. The ExoMol database: molecular line lists for exoplanet and other hot atmospheres. *Journal of Molecular Spectroscopy*, 327:73–94, 3 2016.

[90] A. C. Tibère-Inglesse, B. A. Cruden, C. C. Jelloian, and R. M. Spearrin. Examination of Mars2020 shock-layer conditions via infrared emission spectroscopy of CO2. *AIAA SciTech Conference*, 1 2023.

[91] M. G. Trainer, M. H. Wong, T. H. McConnochie, H. B. Franz, S. K. Atreya, P. G. Conrad, F. Lefèvre, P. R. Mahaffy, C. A. Malespin, H. L. Manning, J. Martín-Torres, G. M. Martínez, C. P. McKay, R. Navarro-González, Vicente-Retortillo, C. R. Webster, and M. P. Zorzano. Seasonal Variations in Atmospheric Composition as Measured in Gale Crater, Mars. *Journal of Geophysical Research: Planets*, 124(11):3000–3024, 11 2019.

[92] J. Vargas, B. Lopez, and M. Lino Da Silva. Heavy Particle Impact Vibrational Excitation and Dissociation Processes in CO2. *Journal of Physical Chemistry A*, 125(2):493–512, 1 2021.

[93] P. L. Varghese and R. K. Hanson. Collisional narrowing effects on spectral line shapes measured at high resolution. *Applied Optics*, 23(14):2376, 7 1984.

[94] W. G. Vincenti and C. H. Kruger. *Introduction to Physical Gas Dynamics*. John Wiley & Sons, Inc., New York, 2 edition, 1967.

[95] C. Wei, D. I. Pineda, L. Paxton, F. N. Egolfopoulos, and R. M. Spearrin. Mid-infrared laser absorption tomography for quantitative 2D thermochemistry measurements in premixed jet flames. *Applied Physics B*, 124(6):123, 6 2018.

[96] C. Wei, K. Schwarm, D. Pineda, and M. Spearrin. Physics-trained neural network for sparse-view volumetric laser absorption imaging of species and temperature in reacting flows. *Optics Express*, 29(14):22553–22566, 2021.

[97] T. K. West, J. E. Theisinger, A. J. Brune, and C. O. Johnston. Backshell radiative heating on human-scale mars entry vehicles. In *47th AIAA Thermophysics Conference, 2017*. American Institute of Aeronautics and Astronautics Inc, AIAA, 2017.

[98] F. M. White. *Viscous Fluid Flow*. McGraw-Hill, New York, NY, 3 edition, 2006.

[99] T. R. White, M. Mahzari, R. A. Miller, C. Y. Tang, J. Monk, J. A. Santos, C. D. Karlgaard, H. S. Alpert, H. S. Wright, and C. Kuhl. Mars entry instrumentation flight data and mars 2020 entry environments. In *AIAA Science and Technology Forum*

and Exposition, AIAA SciTech Forum 2022. American Institute of Aeronautics and Astronautics Inc, AIAA, 2022.

[100] E. E. Whiting. NEQAIR96, Nonequilibrium and Equilibrium Radiative Transport and Spectra Program: User ' s Manual. (December), 1996.

[101] E. E. Whiting, C. Park, Y. Liu, J. O. Arnold, and J. A. Paterson. NEQAIR96, Nonequilibrium and Equilibrium Radiative Transport and Sl_etra Program: User's Manual. Technical report, 1996.

[102] M. J. Wright, C. Y. Tang, K. T. Edquist, B. R. Hollis, P. Krasa, and C. A. Campbell. A review of aerothermal modeling for mars entry missions. In *48th AIAA Aerospace Sciences Meeting Including the New Horizons Forum and Aerospace Exposition*. American Institute of Aeronautics and Astronautics Inc., 2010.

[103] M. J. Wright, T. White, and N. Mangini. Data Parallel Line Relaxation (DPLR) Code User Manual Acadia -Version 4.01.1. *Nasa/Tm-2009-215388*, (October 2009):275, 2009.

[104] M. J. Wright, T. White, and N. Mangini. Data Parallel Line Relaxation (DPLR) Code User Manual Acadia-Version 4.01.1. Technical report, 2009.